

The influence of electric fields and neutral particles on the plasma sheath at ITER divertor conditions

Citation for published version (APA):

Shumack, A. E. (2011). *The influence of electric fields and neutral particles on the plasma sheath at ITER divertor conditions*. [Phd Thesis 1 (Research TU/e / Graduation TU/e), Applied Physics and Science Education]. Technische Universiteit Eindhoven. <https://doi.org/10.6100/IR712706>

DOI:

[10.6100/IR712706](https://doi.org/10.6100/IR712706)

Document status and date:

Published: 01/01/2011

Document Version:

Publisher's PDF, also known as Version of Record (includes final page, issue and volume numbers)

Please check the document version of this publication:

- A submitted manuscript is the version of the article upon submission and before peer-review. There can be important differences between the submitted version and the official published version of record. People interested in the research are advised to contact the author for the final version of the publication, or visit the DOI to the publisher's website.
- The final author version and the galley proof are versions of the publication after peer review.
- The final published version features the final layout of the paper including the volume, issue and page numbers.

[Link to publication](#)

General rights

Copyright and moral rights for the publications made accessible in the public portal are retained by the authors and/or other copyright owners and it is a condition of accessing publications that users recognise and abide by the legal requirements associated with these rights.

- Users may download and print one copy of any publication from the public portal for the purpose of private study or research.
- You may not further distribute the material or use it for any profit-making activity or commercial gain
- You may freely distribute the URL identifying the publication in the public portal.

If the publication is distributed under the terms of Article 25fa of the Dutch Copyright Act, indicated by the "Taverne" license above, please follow below link for the End User Agreement:

www.tue.nl/taverne

Take down policy

If you believe that this document breaches copyright please contact us at:

openaccess@tue.nl

providing details and we will investigate your claim.

The influence of electric fields and neutral particles on the plasma sheath at ITER divertor conditions

PROEFSCHRIFT

ter verkrijging van de graad van doctor aan de
Technische Universiteit Eindhoven, op gezag van de
rector magnificus, prof.dr.ir. C.J. van Duijn, voor een
commissie aangewezen door het College voor
Promoties in het openbaar te verdedigen
op woensdag 22 juni 2011 om 14.00 uur

door

Amy Elizabeth Shumack
geboren te Calgary, Canada

Dit proefschrift is goedgekeurd door de promotoren:

prof.dr. N.J. Lopes Cardozo

en

prof.dr.ir. D.C. Schram

Copromotor:

dr.ir. G.J. van Rooij



This work, supported by the European Communities under the Contract of Association between EURATOM/FOM, was carried out within the framework of the European Fusion Programme with financial support from NWO. The views and opinions expressed herein do not necessarily reflect those of the European Commission.

**The influence of electric fields and
neutral particles on the plasma sheath
at ITER divertor conditions**

A catalogue record is available from the Eindhoven University of Technology Library

ISBN: 978-90-386-2512-6

Reasonable people adapt themselves to the world. Unreasonable people attempt to adapt the world to themselves. All progress, therefore, depends on unreasonable people.

George Bernard Shaw

The influence of electric fields and neutral particles on the plasma sheath at ITER divertor conditions

Summary

The purpose of this thesis is to support the optimization of the ‘exhaust-pipe’, or so-called ‘divertor’, of the tokamak experiment ITER, a large international nuclear fusion reactor now under construction in the south of France. We focus particularly on two ‘tools’ for optimization of the plasma conditions in the divertor: electric fields and neutral particles. We look at how these ‘tools’ affect the plasma conditions at divertor surfaces. These conditions determine the type and rates of plasma-surface interaction processes and ultimately the lifetime of these surface materials.

A plasma boundary phenomenon that can be changed by the presence of electric fields is the so-called ‘Debye sheath’. This is a voltage drop in the transition between plasma and surface. Extremely localized, it will extend only a few micrometers from the ITER divertor plates into the plasma. However, its voltage is a crucial parameter for the interaction of plasma with these plates, since it determines the impinging ion energy. The change in sheath voltage may be particularly large in ITER where conditions are conducive to the development of large electric fields. This is partly due to the low electron temperature, such that electrical resistivity is high. It is also partly due to the high ion fluxes, which allow large currents to flow since electric currents through the divertor plates are limited by the ion flux.

We will see that neutral particles will also influence the boundary conditions in the ITER divertor. Their influence is important, because in contrast to existing tokamak divertors, the ion flux will be so high that the plasma will not be transparent for neutral atoms. Atoms will exchange energy and momentum with plasma particles. Clearly, experiments are required to study the consequences of neutral particles and also electric fields on divertor boundary conditions in the plasma conditions foreseen for ITER.

To perform these experiments systematically, we created the projected ITER divertor plasma conditions as closely as possible in a linear laboratory experiment, Pilot-PSI. Not only is this linear experiment unique in its production of the particle and heat fluxes expected in the ITER divertor, it is also able to produce parameters corresponding to the whole range of present day tokamak divertors. As a linear machine, it has large advantages over tokamak divertor experiments. The diagnostic accessibility is significantly improved and plasma parameters can be controlled much more directly.

We began the project with the development of two non-intrusive diagnostic techniques for the study of electric fields and atomic neutral density in the Pilot-PSI beam. The first diagnostic developed uses optical emission spectroscopy to probe radial electric fields via the $\vec{E} \times \vec{B}$ ion rotation drift. Although these rotating ions do not emit radiation,

we could estimate their drift velocity by observing radiation from excited neutral atoms. These atoms are coupled to both the hot, rotating ions as well as to cold non-rotating neutrals. A procedure was developed to obtain the ion rotation velocity as well as the ion temperature from measured spectra. Radial electric field strengths could then be deduced. We measured electric field strengths in Pilot-PSI of up to 16 kV/m.

Secondly, we needed measurements of the atomic neutral density. Laser induced fluorescence (LIF) is generally well-suited for this purpose, since it probes ground state atomic densities directly and with high spatial resolution. However we found, at the high electron density conditions in Pilot-PSI, the fluorescence signal to be severely limited in strength and the background emission signal to be large. Sensitive LIF measurements were not possible. Absorption spectroscopy provided a good alternative. With this diagnostic we determined an upper limit on the atomic density in the centre of the beam, from which we could calculate the ionization degree ($> 85\%$ near the plasma source). We also found that as the electron density in Pilot-PSI was increased to ITER relevant values, there was a strong rise in the neutral atomic density in the beam and also in the proportion of molecules in the vessel that were strongly rovibrationally excited. Electric fields and ion temperatures could also be determined, and were in line with values from optical emission spectroscopy. Finally, we also obtained estimations for the dissociation degree in the vessel ($\sim 7\%$) and the proportion of rovibrationally excited molecules entering the plasma beam ($\sim 30\%$).

The next step was to learn to understand and manipulate the radial electric fields in the beam of Pilot-PSI. We found that the radial electric field at the plasma source exit increased with nozzle diameter of the source and with magnetic field strength. The electric fields (and associated electric current) were found to penetrate into the beam outside of the plasma source with a characteristic length increasing with magnetization of the beam.

We could then imitate the situation in a tokamak where electric fields in the plasma interface with electrically conducting divertor surfaces. We experimentally verified that electric current will flow through these conducting surfaces. Furthermore, we confirmed that the local sheath voltage can increase substantially from its typical value without biasing, $2.5kT_e/e$ up to the total voltage difference applied. The sheath voltage increases at positions for which the current into the target is positive. Since the sheath voltage determines ion energies at the target, this may have negative consequences for the lifetime of divertor materials. Especially when there are heavy impurities present in the divertor, the threshold energy for physical sputtering may be surpassed. Experiments confirmed that sheath voltage increase at a floating target (for which the electrical potential is free to change) is avoided if an insulator inhibits surface current. We conclude that material damage reduction can be obtained by placing insulating inserts between electrically floating divertor plates.

Finally, we addressed the issue of heating by neutral particles that are reflected from the divertor plates back into the plasma, carrying energy from the sheath. This heating effect will be important in ITER because of the strong ion-neutral coupling projected. We studied its effect in Pilot-PSI, where we amplified its impact by increasing the sheath voltage with target biasing. The result was an increase in the electron temperature measured

close to the target. Also, the electron density was observed to decrease while ion flux to the target remained constant. Since electron and ion densities are equal in a quasineutral plasma, this implies rarefaction caused by plasma acceleration. We attribute this acceleration to the Bohm criterion, which states that the plasma must accelerate to at least the sound velocity at the sheath edge. Since an increased temperature corresponds to an increase in the sound velocity, extra acceleration close to the target must result.

These results are significant because they show that neutral atoms reflected from divertor plates in ITER will have a significant influence on the plasma boundary conditions. This will affect the rates of a range of processes at the plasma-wall interface. One important example is the redeposition rate of eroded divertor plate material. The observed effects are particularly striking when sheath voltages are enhanced either by electric fields in the plasma or by negative plate biasing, but will also play a role when divertor plates are floating or grounded.

In conclusion, this thesis presents an experimental study of the influence of electric fields and neutral particles on the plasma conditions close to tokamak divertor plates. Since diagnostic access to tokamak divertors is limited and measurements of densities, temperatures, velocities and ion energies are minimal, good care should be taken in predicting values for these parameters. The predicted effects will be particularly strong at ITER divertor relevant conditions, where electric fields can be large and ion-neutral coupling strong.

De invloed van elektrische velden en neutrale deeltjes op de plasmashath bij ITER divertor condities

Samenvatting

Het doel van dit proefschrift is om de optimalisatie te ondersteunen van de 'uitlaat' of zogenoemde 'divertor' van het tokamakexperiment ITER, een grote, internationale kernfusiereactor die momenteel gebouwd wordt in Zuid-Frankrijk. Het onderzoek is toegespitst op twee 'gereedschappen' voor optimalisatie van de plasmacondities in de divertor: elektrische velden en neutrale deeltjes. We onderzoeken de invloed van deze 'gereedschappen' op de eigenschappen van de rand van het plasma. Deze randplasmacondities bepalen de soort en frequentie van plasma-wand wisselwerkingprocessen en daardoor ook de levensduur van deze oppervlaktematerialen.

Een fenomeen bij de plasmarand dat door elektrische velden beïnvloed kan worden is de zogenoemde 'Debye sheath'. Dit is een spanningsval die de overgang vormt tussen plasma en een wand. De sheath is extreem gelokaliseerd en reikt vanaf de ITER divertorplaten slechts enkele micrometers het plasma in. Toch is de spanning over deze sheath een cruciale parameter voor de wisselwerking van het plasma met deze platen, omdat die spanning de ionenenergie aan de oppervlakte bepaalt. De verandering van de sheathspanning is mogelijk bijzonder sterk in ITER waar condities gunstig zullen zijn voor het ontstaan van sterke elektrische velden. Dit is deels vanwege de lage elektrontemperatuur, zodat de elektrische weerstand hoog is. Het is ook deels vanwege de hoge ionenfluxen, waardoor grote stromen kunnen lopen omdat elektrische stroom door divertoroppervlakten gelimiteerd is door de ionenflux.

We zullen zien dat neutrale deeltjes ook de randcondities in de ITER divertor zullen beïnvloeden. Dit komt doordat - in tegenstelling tot bestaande tokamakdivertors - de ionenflux zo hoog zal zijn dat het plasma niet meer transparant is voor neutrale atomen. Atomen zullen daardoor energie en impuls uitwisselen met plasmadeeltjes. Het is duidelijk dat experimenten nodig zijn om het effect te bestuderen van neutrale deeltjes en ook van elektrische velden op randplasmacondities bij ITER relevante parameters.

Om deze experimenten systematisch uit te kunnen voeren, hebben we de voorspelde plasmacondities voor de ITER divertor zo goed mogelijk gecreëerd in een lineair laboratorium experiment, Pilot-PSI. Dit experiment is niet alleen uniek in het produceren van de verwachte deeltjes- en warmtefluxen in de ITER divertor, het kan ook de parameters bereiken van alle bestaande tokamakdivertors. Als lineaire machine biedt het grote voordelen vergeleken met experimenten in tokamakdivertors. De toegankelijkheid voor diagnostieken is significant beter en plasmaparameters kunnen directer afgeregeld worden.

We zijn begonnen aan het project door twee meettechnieken te ontwikkelen die de condities in de plasmabundel van Pilot-PSI niet verstoren. Eén techniek werd opgezet voor het bepalen van elektrische velden en één voor neutrale dichtheden. De eerste gebruikt optische emissiespectroscopie om elektrische velden af te leiden van de $\vec{E} \times \vec{B}$ ionenrotatiedrift. Hoewel de roterende ionen geen straling uitzenden, kan hun driftsnelheid geschat worden door straling waar te nemen van aangeslagen neutrale atomen. De eigenschappen van deze atomen zijn gekoppeld aan die van zowel de hete, roterende ionen als aan koude niet-roterende neutralen. Een procedure is ontwikkeld om ionenrotatiesnelheden en ook ionentemperaturen te bepalen uit gemeten spectra. Radiale elektrische velden leiden we vervolgens af. Elektrische velden in Pilot-PSI hebben sterktes tot 16 kV/m.

Ten tweede hadden we metingen nodig van de neutrale atoomdichtheid. Laser geïnduceerde fluorescentie (LIF) is hier over het algemeen een goed geschikte meettechniek voor, omdat het directe metingen oplevert van grondtoestanddichtheden, met hoge ruimtelijke resolutie. Vanwege de hoge elektronendichtheid in Pilot-PSI werd de grootte van het fluorescentiesignaal echter sterk beperkt en het achtergrondsignaal was hoog. Gevoelige LIF-metingen waren daardoor onmogelijk. Absorptiespectroscopie bleek een goed alternatief. Hiermee hebben we een bovenlimiet bepaald voor de atoomdichtheid in het centrum van de bundel, waarmee we vervolgens de ionisatiegraad konden berekenen ($> 85\%$ dichtbij de plasmabron). We zagen ook, dat bij een toename van de elektronendichtheid in Pilot-PSI tot ITER relevante waarden, er een bijbehorende sterke toename was in de neutrale atoomdichtheid in de bundel en ook in de fractie van sterk rovibrationeel geëxciteerde moleculen. Elektrische velden en ionentemperaturen konden ook bepaald worden en waren in overeenstemming met waarden van optische emissie spectroscopie. Als laatste hebben we schattingen gemaakt van de dissociatiegraad in het vat ($\sim 7\%$) en van de fractie van rovibrationeel geëxciteerde moleculen die de bundel binnendringen ($\sim 30\%$).

De volgende stap was het leren begrijpen en manipuleren van de elektrische velden in de bundel van Pilot-PSI. We concludeerden dat de elektrische velden bij de uitgang van de plasmabron toenamen met de diameter van de bronopening en met de magnetische veldsterkte. We leidden daaruit af bepaalden dat elektrische velden (en bijbehorende elektrische stromen) de bundel buiten de plasmabron binnendringen met een karakteristieke lengte die toeneemt met de magnetisatie van de bundel.

Gewapend met deze kennis konden we de situatie in een tokamak nabootsen waarbij elektrische velden in het plasma in aanraking komen met elektrisch geleidende divertoroppervlaktes. Experimenten bevestigden dat elektrische stroom door deze geleidende oppervlaktes zal lopen. Verder hebben we bevestigd dat de lokale sheathspanning significant kan toenemen van de waarde voor een floating trefplaat, $2.5kT_e/e$ tot het totale aanwezige spanningsverschil. De sheathspanning neemt toe bij posities waar de stroom naar de trefplaat toe positief is. Doordat de sheathspanning de ionenenergie bij de trefplaat bepaalt, kan dit negatieve consequenties hebben voor de levensduur van divertormaterialen. Vooral als er zware onzuiverheden aanwezig zijn in de divertor, zou de drempel voor fysieke sputtering overschreden kunnen worden. Experimenten bevestigden dat een isolerend inzetstuk in een floating trefplaat sheathspanningtoename voorkomt, door oppervlaktestroom tegen te houden. We concluderen dat het compartimenteren van elek-

trisch floating divertorplaten met isolatiestukken kan zorgen voor een afname in materiaalschade in tokamakdivertors.

Tenslotte keken we naar het verhittingseffect van neutrale deeltjes die gereflecteerd worden van divertorplaten. De energie die ionen opdoen in de sheath voeren ze namelijk terug naar het plasma wanneer ze als neutralen gereflecteerd worden. Dit verhittingseffect zal belangrijk zijn in ITER vanwege een sterke koppeling tussen ionen en neutralen. We hebben het effect in Pilot-PSI bestudeerd door het eerst uit te vergroten met een opgevoerde sheathspanning, gerealiseerd met trefplaatbiasing. Het resultaat was een toename van de elektronentemperatuur, gemeten dicht bij de trefplaat. Ook zagen we een afname van de elektronendichtheid bij gelijkblijvende ionenflux naar de trefplaat. Omdat elektronen- en ionendichtheden gelijk zijn in een quasineutraal plasma, duidt dit op een plasmaverdunning veroorzaakt door versnelling van het plasma. We schrijven deze versnelling toe aan het Bohm criterium, dat stelt dat de snelheid van het plasma aan de rand van de sheath minstens gelijk is aan de geluidssnelheid. Doordat een temperatuuroptename samenhangt met een toename in de geluidssnelheid, is het resultaat een extra versnelling naar de trefplaat toe.

Deze resultaten zijn significant omdat ze laten zien dat neutrale atomen die gereflecteerd worden van divertorplaten in ITER een significante invloed zullen hebben op de plasmacondities dicht bij de platen. Deze invloed zal ook doorwerken in de frequenties van een scala van processen die plaatsvinden in de wisselwerking tussen plasma en wand. Een belangrijk voorbeeld is de redepositiesnelheid van geërodeerd divertorplaatmateriaal. De waargenomen effecten zijn bijzonder markant wanneer de sheathspanning vergroot wordt hetzij door elektrische velden in het plasma, hetzij door negatieve trefplaatbiasing, maar ze zullen ook een rol spelen als divertorplaten floating of geaard zijn.

Tot slot, dit proefschrift presenteert een experimentele studie van de invloed van elektrische velden en neutrale deeltjes op de randcondities bij tokamakdivertorplaten. Doordat diagnostieke toegang tot tokamakdivertors beperkt is en metingen van dichtheden, temperaturen, snelheden en ionenenergieën minimaal zijn, is zorg geboden bij het voorspellen van waarden van deze parameters. Bij condities relevant voor de ITER divertor worden bijzonder sterke effecten verwacht, vanwege sterke elektrische velden en sterke wisselwerking tussen ionen en neutrale deeltjes.

Contents

1	Introduction	1
1.1	The tokamak divertor	2
1.2	The importance of electric fields and neutral particles in the divertor . . .	3
1.3	The ITER divertor plasma	4
1.4	The relevance of Pilot-PSI	5
1.5	This thesis	6
1.6	Publications	7
2	Experimental arrangement	13
2.1	Experimental	13
2.1.1	The plasma generator	13
2.1.2	Diagnostics	15
3	Rotation of a strongly magnetized hydrogen plasma column	21
3.1	Introduction	22
3.2	Experimental	23
3.2.1	The linear plasma generator Pilot-PSI	23
3.2.2	Optical emission spectroscopy set up	25
3.3	Spectrum analysis	26
3.3.1	Measured Balmer- β line shape and intensity profile	26
3.3.2	Hollow emission profile	28
3.3.3	Asymmetric line profile: double Voigt fit	30
3.3.4	Results and discussion for rotation and ion temperature	31
3.3.5	Assessment of fit based on density and temperature predictions	34
3.4	Consideration of underlying plasma processes	37
3.4.1	H*(n=4) production mechanisms	37
3.4.2	Hollow emission profiles from reaction balance	37
3.4.3	Discussion of two populations	38
3.5	Rotation of the plasma jet	40
3.6	Conclusion	43
3.7	Acknowledgment	44
4	Diagnosing ions and neutrals via n=2 excited hydrogen atoms	49
4.1	Introduction	50
4.2	Analysis of the population balance of n=2 excited atoms	51
4.2.1	Production mechanisms of n=2 excited neutrals	51

4.2.2	Local population balance of $n=2$ excited atoms	53
4.2.3	Influence of the escape factor in the population balance	54
4.2.4	Radial dependencies of the population balance	54
4.3	Experiment	55
4.3.1	Experimental set-up	55
4.3.2	Overview of the plasma conditions	57
4.3.3	Analysis of data	57
4.4	LIF and absorption Measurements	60
4.4.1	Measurement data	60
4.4.2	Spectral analysis	66
4.5	Monte Carlo simulation of the radiation transport	67
4.5.1	Method	67
4.5.2	Results	70
4.6	Interpretation of the results	72
4.6.1	Estimation of the escape factor from spectral analysis	72
4.6.2	Examination of the $n=2$ density behavior for determination of neutral densities	73
4.6.3	Summary of determined neutral densities	76
4.7	Discussion of the diagnostic method for determination of ion parameters	76
4.8	Conclusion	77
5	Current effects on a magnetized plasma in contact with a surface	81
5.1	Introduction	82
5.2	Experimental	82
5.3	Modelling	84
5.3.1	Background	84
5.3.2	Modelling electric fields and currents in plasma beam	85
5.3.3	Modelling the effect of current through a surface on the plasma- wall sheath	87
5.3.4	Combination of modelling in beam and at plasma-wall transition	89
5.4	Experimental approach	91
5.5	Results	92
5.6	Conclusions	97
5.7	Acknowledgements	97
6	Plasma acceleration on negative biasing	101
6.1	Introduction	102
6.2	The plasma-wall interface in Pilot-PSI	103
6.2.1	Debye sheath	103
6.2.2	Pre-sheath	103
6.3	Experimental	104
6.4	Study of electric current configuration as a function of bias	105
6.5	Study of plasma parameters as a function of bias	106
6.6	Interpretation: plasma heating by energetic target reflected neutrals . . .	113

6.7	Quantitative evaluation of the effect of target reflected neutrals	116
6.7.1	Power balance as a function of axial distance	116
6.7.2	Evaluation of separation of ion and electron temperatures	121
6.8	Discussion: comparison of measurements with calculations	123
6.9	Conclusion	124
7	Discussion	127
7.1	Conclusions	127
7.2	Implications for further research on Pilot-PSI	129
7.3	Implications for tokamaks	130
7.4	Implications for ITER and beyond	131
	Acknowledgements	135
	Curriculum vitae	137

Chapter 1

Introduction

Nuclear fusion appeared recently in a list of "12 events that will change everything" in the Scientific American [1]. That is certainly the case: It is clean and safe, the fuel resources are practically limitless and available to all and the land requirements are small. The challenges are just as large as the rewards. In the tokamak design (see Fig. 1.1), turbulent plasma at a temperature of 150 million degrees must be stabilized, floating in a magnetic field to keep it from the walls of the vessel. Superconducting magnetic coils need to

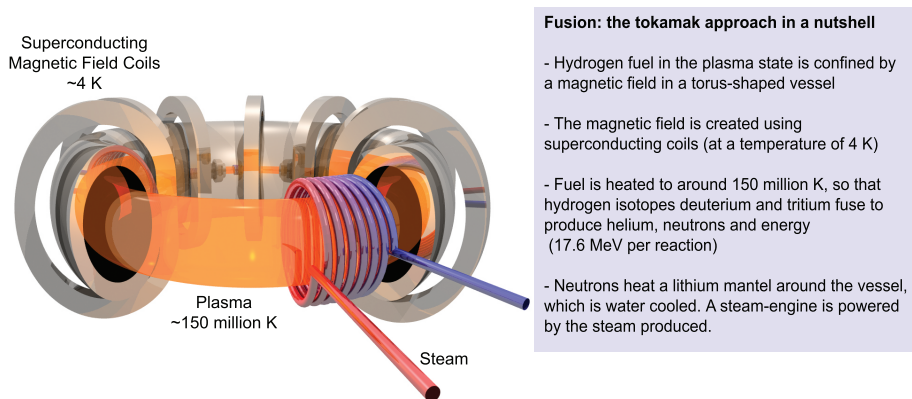


Figure 1.1: Fusion: the tokamak approach in a nutshell. Picture by Mark Westra.

be maintained at a temperature of 4 K at a distance of tens of centimeters from the hot plasma, constituting one of the largest temperature gradients in the universe.

The total power produced will be comparable to the power produced in for example a coal plant, but in a much smaller volume, since the energy in nuclear bonds is millions of times larger than the energy in chemical bonds. As the fuel of the reaction is renewed, exhaust products will need to be removed. It is unavoidable that these products, in the form of high heat and particle fluxes will come into contact with a surface during this removal process. The fluxes involved are more than ten times larger than those endured by a space shuttle on re-entry [2; 3]. In addition, for fusion to be economically feasible these fluxes must be endured continuously for months on end.

The design of the international fusion experiment, ITER (see Fig. 1.2), includes a so-called divertor in which the fusion products are removed from the machine. By the use

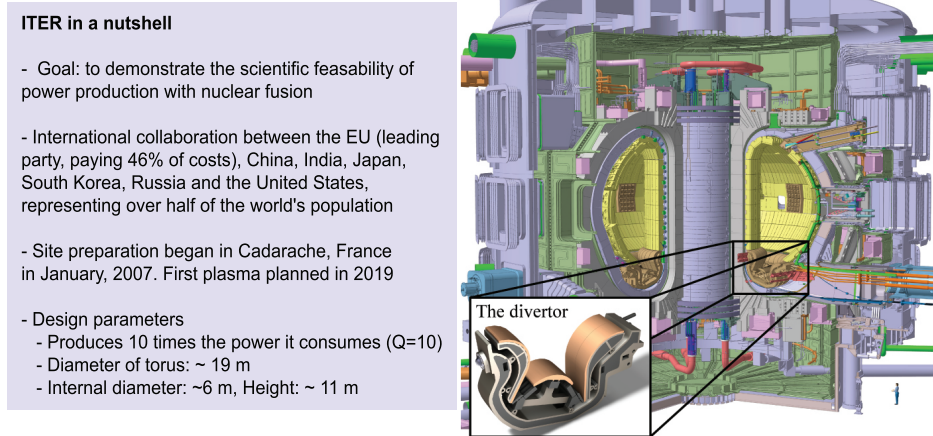


Figure 1.2: Design of the experimental fusion reactor ITER. The inset is an illustration of the divertor. ITER image from www.iter.org, compilation with divertor by Jeroen Westerhout.

of various cooling techniques, the temperature of the plasma reaching the ITER divertor plates is reduced to 1-7 eV ($1 \text{ eV} \equiv 11600 \text{ K}$). This is required to keep the energy of the particles that hit the divertor plates below the sputtering threshold. Energy and particle fluxes are nonetheless expected to be high: 10 MW and 10^{24} particles/m²/s.

1.1 The tokamak divertor

The divertor concept was proposed in 1951 by Spitzer [4] as a way of isolating the point where exhaust products are extracted from the vessel (where the plasma hits the wall) from the main fusion plasma. This is done as depicted in Fig. 1.3. The main fusion plasma is confined by closed magnetic field lines. At the so-called separatrix, or last closed flux surface (LCFS), the field lines ‘open up’ at an ‘x-point’ and intercept divertor plates. Plasma particles that diffuse radially outward across the separatrix into the so-called scrape-off layer, follow the field lines and are dumped on the divertor plates. Pumps behind these plates carry away the particles, whereafter the fuel is separated from the exhaust and re-injected into the vessel.

Design of the divertor is a large challenge as it must fulfil several requirements simultaneously. The divertor must ensure [5] manageable power flux to the plasma facing components, efficient pumping of helium (the ash of the fusion reaction) out of the vessel, screening of impurities produced in or added to the divertor region from the main

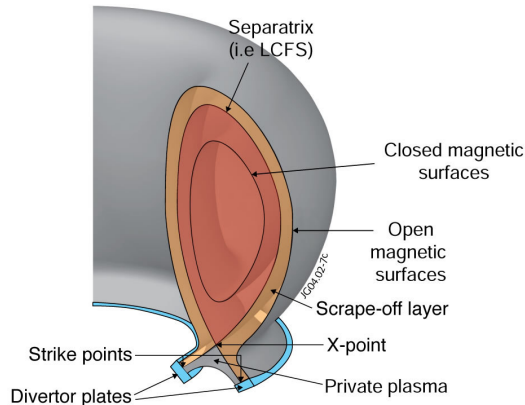


Figure 1.3: The divertor concept in a tokamak. From <http://www.jet.efda.org>.

plasma, while at the same time maintaining good confinement and relatively high core plasma density in the main plasma and ensuring survival of the divertor plates [6].

With the aim of achieving all of these goals simultaneously, much work has been done on understanding and manipulating the divertor power balance. This has been done using a wide variety of methods. To name a few: by material choice [6], magnetic [7] and spatial [8] divertor configuration, impurity seeding for radiative cooling [9; 10] and manipulation of plasma parameter profiles to achieve different regimes such as so-called detachment [11]. In all of these approaches, the electric field configuration and neutral particle density can play an important role. These two parameters may also be specifically tweaked for optimization of the functionality of the divertor.

1.2 The importance of electric fields and neutral particles in the divertor

Electric fields have played a significant role in improvement of the tokamak divertor design. Divertor biasing (and limiter or electrode biasing [12]) has been used for the achievement of higher confinement regimes [13]. It has also been used [14; 15] to increase impurity retention in the divertor region and to improve the helium exhaust. Staebler [16] showed plasma heating by divertor biasing such that the plasma expands to match the width of the divertor plates (thus spreading the plasma energy over a larger area).

These uses of electric fields as a tool in tokamak divertors require an understanding of their effect on the plasma. It is useful to understand how an electric field and its accompanying electric current will be distributed in the plasma, since this determines where the Ohmic power is dissipated. Also, the influence of electric fields on the plasma-wall

sheath - the region of positive charge at a plasma-wall interface - is important. It determines the energy of ions impinging on the target, which is crucial for example for the erosion of the divertor plate material.

Much work has already been done on understanding what happens when an electric field exists in a divertor, however most of the literature focuses on fields arising from temperature differences. Such fields arise because the plasma-wall sheath voltage depends linearly on electron temperature and develops in front of an equipotential surface. The so-called thermoelectric currents that result were described theoretically for the first time by Harbour [17] and are given a detailed treatment by Stangeby [18]. Experimental tokamak studies [19; 20] confirm these results. The current configuration measured due to induced voltage loops in the scrape-off layer [21] and electric fields from divertor plate biasing [16; 22] is similar.

Shortcomings of these studies include the multitude of parameters at work in a tokamak which complicate direct comparison of results with theory. Also, diagnostic measurements are limited by the accessibility of the divertor region and the fact that probe measurements influence the plasma conditions that are being measured. Interpretation of probe measurements in a magnetic field is also controversial [23]. Systematic experimental confirmation of the theoretical effects of electric fields at a conducting surface would therefore be highly desirable.

Neutrals are also of great importance in determining the plasma conditions in the divertor. Via ion-neutral friction, they are responsible for the so-called detached regime [11] in which a drastic drop of particle fluxes to the divertor plates is observed. Molecular assisted recombination [24] and the associated radiation by neutrals [25] are also instrumental in the dissipation of energy in this regime.

For a tokamak divertor with high electron densities (such as ITER), neutral particles can also have an influence on the pre-sheath voltage. This is the small fraction of the plasma-wall sheath potential that extends into the plasma and accelerates ions to the sound velocity (or above) at the sheath edge [26]. The pre-sheath in the divertor is important since it influences the plasma parameters at the divertor plates, which determine particle interaction rates and therefore plasma-wall interaction processes. One example is the probability of re-deposition of eroded target material [6].

The tokamak divertor is not conducive to detailed measurement of the pre-sheath, however such measurements have been made in the linear divertor simulator, PSI-2 [27]. Similar experiments in the ITER divertor plasma regime would be useful for extrapolation to ITER.

1.3 The ITER divertor plasma

To quote Stangeby and Pitcher [5], "The conditions expected in ITER are far removed from those found in existing devices (Janeschitz et al 1995 [28]) and thus extrapolating present divertor results towards future machines requires a detailed understanding of the present operation."

Important characteristics of the projections for the ITER divertor are [28] a high

plasma flux density ($\sim 10^{24} \text{ m}^{-2}\text{s}^{-1}$), a correspondingly high electron density $\sim 10^{20} \text{ m}^{-3}$ and low electron temperatures $\sim 1\text{-}7 \text{ eV}$. An appreciable neutral density is expected close to the target due to neutrals reflected from the target and ion-neutral interactions will be important in the momentum and energy balance. The low temperature expected in the ITER divertor plasma is interesting, in that it straddles the sharp rise in the Saha equilibrium [29] between an ionizing and a recombining plasma. The temperature will increase from the divertor plates towards the main plasma such that at an ionization front is encountered.

Plasma at the projected low electron temperature conditions will have high resistivity ($> 10^{-4} \Omega\text{m}$ along the field lines). Electric currents through plasma and divertor plates, which are always limited by the ion flux at the plates, can be large due to the high projected ion fluxes (160 kA/m^2 at $\Gamma = 10^{24} \text{ m}^{-2}\text{s}^{-1}$). This combination will allow large electric fields to exist in the ITER divertor.

1.4 The relevance of Pilot-PSI for the study of electric fields and neutral particles in the ITER divertor

Pilot-PSI is a linear plasma generator that simulates the conditions projected close to the divertor plates of ITER in a plasma beam that impinges on an exchangeable target. Such a divertor simulator is indispensable in the study of divertor physics, as it enables systematic studies in a controlled environment. Furthermore, the plasma is much more easily accessible for diagnostics than in a tokamak.

Pilot-PSI is the first linear divertor simulator to reach the plasma fluxes expected in the divertor of ITER [28]. Fig. 1.4 shows the range of plasma conditions that has been achieved at its target. The particle fluxes are calculated from the Bohm flux [18] $\Gamma = 0.5n_e c_s$, which assumes a density drop of 0.5 from the measurement position (15 mm from the target) to the target. Note that the conditions projected for the ITER divertor, $\Gamma \approx 10^{24} \text{ m}^{-2}\text{s}^{-1}$, $n_e = 10^{20}\text{-}10^{21} \text{ m}^{-3}$ and the lower part of the electron temperature range (1-3 eV) are well covered.

As in any simulation, there are some aspects of the plasma-wall conditions in ITER that are not reproduced exactly. One is the higher part of the ITER divertor temperature range. Pilot-PSI thus specifically reproduces the ITER divertor conditions in regions downstream of the ionization front. Another aspect is the difference in geometry, for example, the angle at which the magnetic field lines intersect the divertor plates. In Pilot-PSI, magnetic field lines are perpendicular to the target, while in ITER this angle will be ≈ 20 degrees [28]. It will be possible to mount the target at an angle to the magnetic field in the Pilot-PSI upgrade, Magnum-PSI. Extrapolation of results must consider these differences.

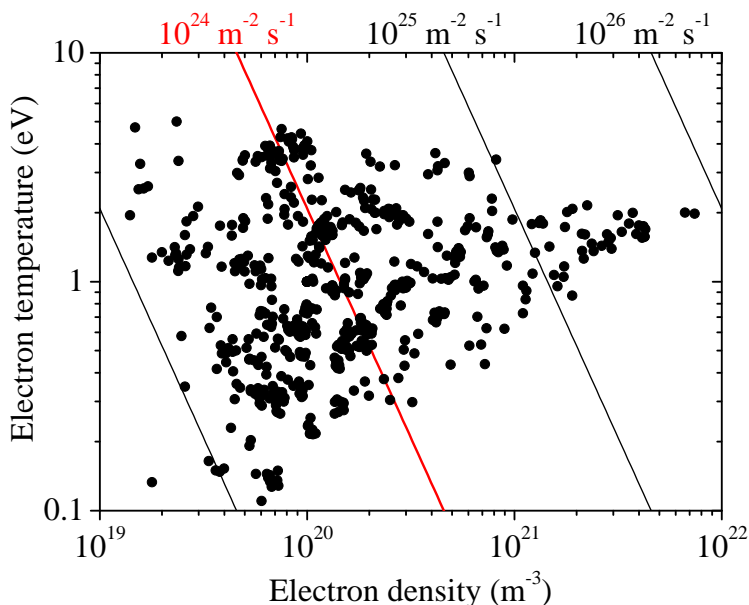


Figure 1.4: The range of conditions produced at the target in Pilot-PSI. Corresponding flux densities are indicated with diagonal lines. The red line at $10^{24} \text{ m}^{-2} \text{ s}^{-1}$ indicates the nominal ITER value. This graph was compiled by Jeroen Westervhout and Wouter Vijvers and is taken from [30]

1.5 This thesis

We have seen that for the achievement of tokamak divertor specifications, electric fields are important tools and neutral particles play an important role. The goal of this thesis is to support tokamak divertor experiments by providing systematic, experimental studies of the effect of electric fields and neutral particles on the sheath and pre-sheath region of a plasma-wall transition. The experiments are performed at the same plasma parameters as projected for the ITER divertor, so that the studies are as relevant as possible for this next generation fusion experiment. We address the following questions:

1. When electric fields are applied or come into existence in a magnetized plasma near a conducting target, how will the electric current be distributed, and how will the plasma-wall sheaths be affected?
2. How will the plasma parameters in a high electron density plasma in front of a conducting target be affected by target reflected neutrals when the target plate is biased?

We approach the study with the combination of an experimental study in the linear plasma generator Pilot-PSI and simple modeling. Two sub-questions must be addressed

before we can study the main research questions of this thesis:

- a. How can we non-intrusively measure the electric fields and neutral particle densities in Pilot-PSI?
- b. What is the origin of the radial electric fields in Pilot-PSI and how can we manipulate them?

We require non-intrusive electric field and neutral particle measurements and avoid using electrical probes not only because they disturb the plasma conditions, but also because they produce ambiguous results in the presence of a magnetic field [23]. In Chap. 3 we develop a method using optical emission spectroscopy to determine the radial electric fields via the ion $\vec{E} \times \vec{B}$ drift. Since hydrogen ions do not radiate, we rely for this method on the coupling between radiating neutrals with plasma ions. A method using absorption spectroscopy is also developed in Chap. 4 to estimate the atomic neutral density in the plasma - important at these plasma conditions where interactions between the plasma and neutrals has a significant influence on the dynamics of the plasma.

The next step (Chap. 5) is to characterize the radial electric field behaviour in Pilot-PSI using measurements with the diagnostic developed in combination with simple modelling. Having learned how to manipulate these fields, we then study the effect of inserting a conducting target. Measurements and modelling reveal the reaction of the electric field and current distribution as well as the plasma-wall sheaths at the target. Results are also compared to a second situation in which electric current flow through the target is inhibited by an insulator.

After studying effects of electric fields at a target, we turn in Chap 6 to effects caused by a very specific electric field, that of the pre-sheath. We are interested in the effect that neutrals will have on this field, specifically on the resulting plasma parameters. We measure the plasma parameters at several positions in front of the target via Thomson scattering while monitoring the ion saturation current. A simple model aids us in exploring the influence that neutrals reflected from the target have in causing the observed dependencies.

1.6 Publications

Two chapters of this thesis have been published:

- **Rotation of a strongly magnetized hydrogen plasma column determined from an asymmetric Balmer-beta spectral line with two radiating distributions**
A. E. Shumack, V. P. Veremiyenko, D. C. Schram, H. J. de Blank, W. J. Goedheer, H. J. van der Meiden, W. A. J. Vijvers, J. Westerhout, N. J. Lopes Cardozo and G. J. van Rooij, *Phys. Rev. E*, **78**, 046405 (2008)
- **Diagnosing ions and neutrals via n=2 excited hydrogen atoms in plasmas with high electron density and low electron temperature**

A. E. Shumack, D. C. Schram, J. Biesheuvel, W. J. Goedheer and G. J. van Rooij, *Phys. Rev. E*, **83**, 036402 (2011)

Other first author publications:

- **LIF and absorption in a high electron density plasma**

A. E. Shumack, J. Biesheuvel, R. A. H. Engeln, W. J. Goedheer, N. J. Lopes Cardozo, H. J. van der Meiden, J. Rapp, D. C. Schram, W. A. J. Vijvers, J. Westerhout, G. M. Wright and G. J. van Rooij, *Conference Proceedings of XXIX International Conference on Phenomena in Ionized Gases*, **1**, 299 (2009) ISBN:978-1-61567-694-1

The author of this thesis was a co-author in the following publications:

- **Materials research under ITER-like divertor conditions at FOM Rijnhuizen**

G. M. Wright, J. Westerhout, R. S. Al, E. Alves, L. C. Alves, N. P. Barradas, M. A. van den Berg, D. Borodin, S. Brezinsek, S. Brons, H. J. N. van Eck, B. de Groot, A. W. Kleyn, W. R. Koppers, O. G. Kruijt, J. Linke, N. J. Lopes Cardozo, M. Mayer, H. J. van der Meiden, P. R. Prins, et al., *J. Nucl. Mater.* (2011), doi:10.1016/j.jnucmat.2010.12.209

- **Experimental and theoretical determination of the efficiency of a sub-atmospheric flowing high power cascaded arc hydrogen plasma source**

W. A. J. Vijvers, D. C. Schram, A. E. Shumack, N. J. Lopes Cardozo, J. Rapp and G. J. van Rooij, *Plasma Sources Sci. Technol.*, **19**, 065016 (2010)

- **Carbon film growth and hydrogenic retention of tungsten exposed to carbon-seeded high density deuterium plasmas**

G. M. Wright, R. S. Al, E. Alves, L. C. Alves, N. P. Barradas, A. W. Kleyn, N. J. Lopes Cardozo, H. J. van der Meiden, V. Philipps, G. J. van Rooij, A. E. Shumack, W. A. J. Vijvers, J. Westerhout, E. Zoethout, J. Rapp, *J. Nucl. Mater.*, **396**, 176-180 (2010)

- **Thomson scattering at Pilot-PSI and Magnum-PSI**

G. J. van Rooij, H. J. van der Meiden, M. H. J. 't Hoen, W. R. Koppers, A. E. Shumack, W. A. J. Vijvers, J. Westerhout, G. M. Wright and J. Rapp, *Plasma Phys. Controlled Fusion*, **51** 124037 (2009)

- **Hydrogenic retention in tungsten exposed to ITER divertor relevant plasma flux densities**

G. M. Wright, A. W. Kleyn, E. Alves, L. C. Alves, N. P. Barradas, G. J. van Rooij, A. J. van Lange, A. E. Shumack, J. Westerhout, R. S. Al, W. A. J. Vijvers, B. de Groot, M. J. van de Pol, H. J. van der Meiden, J. Rapp, N. J. Lopes Cardozo, *J. Nucl. Mater.*, **390-391**, 610-613 (2009)

- **Multiple discharge channels in a cascaded arc to produce large diameter plasma beams**

W. A. J. Vijvers, B. de Groot, R. S. Al, M. A. van den Berg, H. J. N. van Eck, W. J. Goedheer, A. W. Kleyn, W. R. Koppers, O. G. Kruijt, N. J. Lopes Cardozo, H. J. van der Meiden, M. J. van de Pol, P. R. Prins, J. Rapp, D. C. Schram, A. E. Shumack, P. H. M. Smeets, J. Westerhout, G. M. Wright and G. J. van Rooij, *Fusion Eng. Des.*, **84**, 1933-1936 (2009)

- **Chemical erosion of different carbon composites under ITER-relevant plasma conditions**

J. Westerhout, D. Borodin, R. S. Al, S. Brezinsek, M. H. J. 't Hoen, A. Kirschner, S. Lisgo, H. J. van der Meiden, V. Philipps, M. J. van de Pol, A. E. Shumack, G. De Temmerman, W. A. J. Vijvers, G. M. Wright, N. J. Lopes Cardozo, J. Rapp and G. J. van Rooij, *Phys. Scripta*, 014017 (2009)

- **High sensitivity imaging Thomson scattering for low temperature plasma**

H. J. van der Meiden, R. S. Al, C. J. Barth, A. J. H. Donné, R. Engeln, W. J. Goedheer, B. de Groot, A. W. Kleyn, W. R. Koppers, N. J. Lopes Cardozo, M. J. van de Pol, P. R. Prins, D. C. Schram, A. E. Shumack, P. H. M. Smeets, W. A. J. Vijvers, J. Westerhout, G. M. Wright and G. J. van Rooij, *Rev. Sci. Instrum.*, **79**, 013505 (2008)

- **Emission spectroscopy of hydrogen lines in magnetized plasmas: Application to PSI studies under conditions foreseen in ITER**

S. Ferri, J. Rosato, Y. Marandet, L. Godbert-Mouret, M. Koubiti, R. Stamm, A. E. Shumack, J. Westerhout, J. Rapp and G. J. van Rooij, *AIP Conf. Proc.*, *Spectral Line Shapes: Volume 15 - 19th International Conference on Spectral Line Shapes*, **1058**, 216-218 (2008)

- **On the power balance at the end plate of the plasma column in Pilot-PSI**

C. Costin, V. Anita, R. S. Al, B. de Groot, W. J. Goedheer, A. W. Kleyn, W. R. Koppers, N. J. Lopes Cardozo, H. J. van der Meiden, R. J. E. van de Peppel, R. P. Prins, G. J. van Rooij, A. E. Shumack, M. L. Solomon, W. A. J. Vijvers, J. Westerhout, G. Popa, 34th EPS Conference on Plasma Phys. Warsaw, 2 - 6 July 2007 *ECA Vol.31F*, P-5.084 (2007)

- **Cooling down MiniGRAIL to milli-Kelvin temperatures**

A. de Waard, L. Gottardi, M. Bassan, E. Coccia, V. Fafone, J. Flokstra, A. Karbalai-Sadegh, Y. Minenkov, A. Moleti, G. V. Pallottino, M. Podt, B. J. Pors, W. Reincke, A. Rocchi, A. Shumack, S. Srinivas, M. Visco and G. Frossati, *Classical Quant. Grav.*, **21**, S465 (2004)

- **MiniGRAIL, the first spherical detector**

A. de Waard, L. Gottardi, J. van Houwelingen, A. Shumack and G. Frossati, *Classical Quant. Grav.*, **20**, S143 (2003)

- **Two-stage SQUID systems and transducers development for MiniGRAIL**

L. Gottardi, M. Podt, M. Bassan, J. Flokstra, A. Karbalai-Sadegh, Y. Minenkov, W.

Reinke, A. Shumack, S. Srinivas, A. de Waard and G. Frossati, *Classical Quant. Grav.*, **21**, S1191 (2004)

Conference contributions:

- **Laser induced fluorescence and absorption in a high electron density plasma**
Poster presentation at XXIX International Conference on Phenomena in Ionized Gases, July 12-17, 2009, Cancún, México
- **The influence of electric currents on fusion relevant plasma surface interaction**
Poster presentation at 21st NNV-symposium on Plasma Physics and Radiation Technology, March 03-04, 2009, Lunteren
- **Anomalous plasma acceleration near a negatively biased target in the linear plasma generator Pilot-PSI**
Oral presentation at the 11th Workshop on the Exploration of Low Temperature Plasma Physics, November 25-26, 2008, Rolduc, Kerkrade
- **Plasma potential probed with $\mathbf{E} \times \mathbf{B}$ rotation**
Poster presentation at 20th NNV-symposium on Plasma Physics and Radiation Technology, 2008, Lunteren
- **Rotation and forward velocity in the Pilot-PSI hydrogen plasma column**
Oral presentation at the 7th Workshop on Frontiers in Low Temperature Plasma Diagnostics, 1 - 5 April 2007, Beverley, United Kingdom
- **Rotation velocity and ion-neutral coupling in the Pilot-PSI hydrogen plasma column**
Poster presentation at the 7th International Conference on Dissociative Recombination: Theory, Experiments, and Applications, 2007, Ameland
- **Rotation and forward velocity in the Pilot-PSI hydrogen plasma column**
Poster presentation at 19th NNV-symposium on Plasma Physics and Radiation Technology, 2007, Lunteren
- **Two-photon absorption Laser Induced Fluorescence on Pilot-PSI**
Oral presentation at the 17th NNV/CPS-Symposium on Plasma Physics and Radiation Technology, 2005, Lunteren

References

- [1] C. Q. Choi *et al.*, “12 events that will change everything,” *Scientific American Magazine*, June, 2010.
- [2] M. W. Winter, M. Auweter, and C. Park, “Determination of temperatures and particle densities in a subsonic high enthalpy plasma flow from emission spectroscopic measurements,” *32nd AIAA Plasmadynamics and Lasers Conference*, 2001.
- [3] Website. [http://www.columbiassacrifice.com/\\$D_temperature.htm](http://www.columbiassacrifice.com/$D_temperature.htm).
- [4] L. Spitzer, “US atomic energy commission report,” tech. rep., 1951. NYO-993 (PM-S-1).
- [5] C. S. Pitcher and P. C. Stangeby, “Experimental divertor physics,” *Plasma Phys. Controlled Fusion*, vol. 39, no. 779-930, 1997.
- [6] J. Roth *et al.*, “Recent analysis of key plasma wall interaction issues for ITER,” *J. Nucl. Mater.*, vol. 390-391, pp. 1–9, 2009.
- [7] D. Meade *et al.* *Plasma Physics and Controlled Nuclear Fusion Research*, vol. I, no. 665, 1980. IAEA-CN-38/X-1.
- [8] M. R. Wade *et al.*, “Helium exhaust studies in the DIII-D tokamak,” *J. Nucl. Mater.*, vol. 220-222, pp. 178–182, 1995.
- [9] S. L. Allen *et al.*, “Recent DIII-D divertor research,” *Plasma Phys. Controlled Fusion*, vol. 37, no. 11A, p. A191, 1995.
- [10] The JET Team (presented by G.F. Matthews), “Highly radiating and detached plasmas on carbon and beryllium targets,” *Plasma Phys. Controlled Fusion*, vol. 37, no. 11A, p. A227, 1995.
- [11] P. C. Stangeby, “Can detached divertor plasmas be explained as self-sustained gas targets?,” *Nucl. Fusion*, vol. 33, no. 1695, 1993.
- [12] R. R. Weynants *et al.*, “Confinement and profile changes induced by the presence of positive or negative radial electric fields,” *Nucl. Fusion*, vol. 32, no. 837, 1992.
- [13] A. Boileau, “Tokamak plasma biasing,” *Nucl. Fusion*, vol. 33, no. 1, 1993.
- [14] B. Terreault *et al.*, “Improvements in recycling and impurity control obtained by divertor biasing,” *Nucl. Fusion*, vol. 34, no. 6, p. 777, 1994.
- [15] R. Décoste, “Various divertor biasing configurations and improved divertor performance with biasing on Tokamak de Varennes (TdeV),” *Phys. Plasmas*, vol. 1, no. 5, 1994.
- [16] G. M. Staebler, “Divertor bias experiments,” *J. Nucl. Mater.*, vol. 220-222, pp. 158–170, 1995.

- [17] P. J. Harbour, “Current flow parallel to the field in a scrape-off layer,” *Contrib. Plasm. Phys.*, vol. 28, pp. 417–419, 1988.
- [18] P. C. Stangeby, *The Plasma Boundary of Magnetic Fusion Devices*. Taylor & Francis Group, 2000.
- [19] G. M. Staebler and F. L. Hinton, “Currents in the scrape-off layer of diverted tokamaks,” *Nucl. Fusion*, vol. 29, no. 10, 1989.
- [20] R. Pitts, S. Alberti, P. Blanchard, J. Horacek, H. Reimerdesa, and P. C. Stangeby, “ELM driven divertor target currents on TCV,” *Nucl. Fusion*, vol. 43, no. 1145-1166, 2003.
- [21] A. Kallenbach *et al.*, “Divertor power and particle fluxes between and during type-I ELMs in the ASDEX upgrade,” *Nucl. Fusion*, vol. 48, no. 085008, 2008.
- [22] V. Rozhansky and M. Tendler, “The impact of a biasing radial electric field on the scrape-off layer in a divertor tokamak,” *Phys. Plasmas*, vol. 1, no. 8, 1994.
- [23] G. F. Matthews, “Tokamak plasma diagnosis by electrical probes,” *Plasma Phys. Controlled Fusion*, vol. 36, no. 1595, 1994.
- [24] R. K. Janev, “Alternative mechanisms for divertor plasma recombination,” *Phys. Scripta*, vol. T96, pp. 94–101, 2002.
- [25] D. Lumma, J. L. Terry, and B. Lipschultz, “Radiative and three-body recombination in the Alcator C-mod divertor,” *Phys. Plasmas*, vol. 4, no. 7, 1997.
- [26] D. Bohm, *The Characteristics of Electric Discharges in Magnetic Fields*. New York: McGraw-Hill, 1949. Chap. 3.
- [27] T. Lunt, G. Fussmann, and O. Waldmann, “Experimental investigation of the plasma-wall transition,” *Phys. Rev. Lett.*, vol. 100, no. 175004, 2008.
- [28] G. Janeschitz, K. Borrass, G. Federici, Y. Igitkhanov, A. Kukushkin, H. D. Pacher, G. W. Pacher, and M. Sugihara, “The ITER divertor concept,” *J. Nucl. Mater.*, vol. 220-222, pp. 73–88, 1995.
- [29] C. Garrot, *Statistical Mechanics and Thermodynamics*. Oxford University Press, 1995.
- [30] W. A. J. Vijvers, *A high-flux cascaded arc hydrogen plasma source*. PhD thesis, Technische Universiteit Eindhoven, 2011.

Chapter 2

Experimental arrangement

2.1 Experimental

The experimental set-up of the linear divertor simulator Pilot-PSI is covered briefly in each of the chapters 3-6. For clarity, we also explain the set-up separately in this chapter. A schematic of the linear plasma generator Pilot-PSI is shown in Fig. 2.1. It schematically depicts the main optical diagnostics used in this thesis.

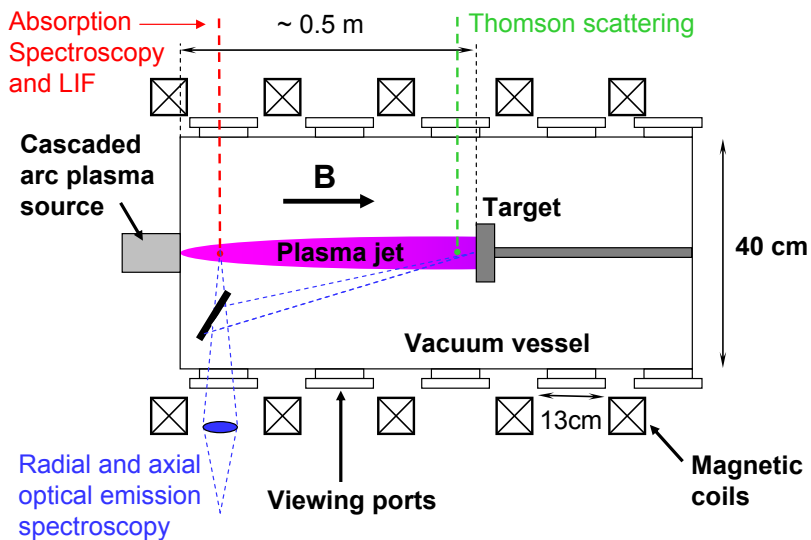


Figure 2.1: Schematic drawing of the experimental arrangement of Pilot-PSI and its diagnostics.

2.1.1 The plasma generator

The plasma in Pilot-PSI is produced with a cascaded arc [1], depicted in Fig.2.2. Its design is based on extensive work at the Eindhoven University of Technology [2; 3; 4].

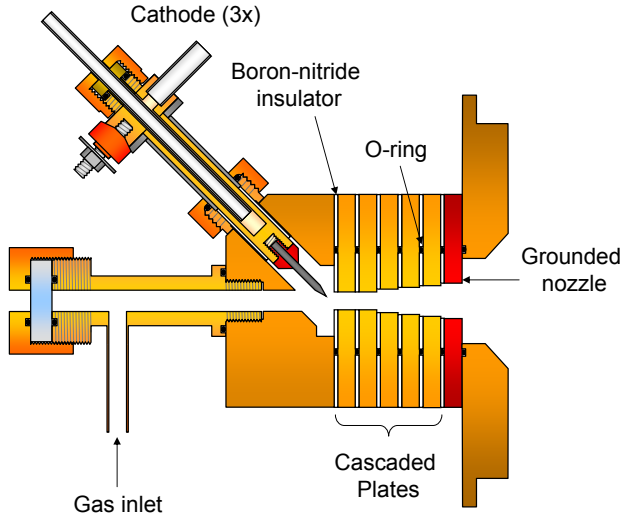


Figure 2.2: Schematical drawing of the cascaded arc used to produce plasma in Pilot-PSI. Picture by Jeroen Westerhout.

The working gas enters the plasma source via the gas inlet. It is ionized in the arc channel of the cascaded plates due to the discharge between the three cathodes and the anode. The nozzle is electrically connected to the anode which is in contact with the electrically grounded vessel wall. The cascaded plates are insulated from one another and are electrically floating.

For the plasma conditions described in this thesis, the gas flow into the source was 1-3 standard litres per minute (slm)*, the discharge current was 80-200 A and the cathode voltage 100-250 V. The cathode tips are constructed from tungsten, the cascaded arc plates are from copper and are insulated from one another by boron-nitride spacers. The anode is made of copper-tungsten. For most of the experiments in this thesis, the so-called ‘trumpet source’ design is used. In this design the diameter of the channel in the cascaded plates increases from the cathode to the anode side. Channel diameters are 5, 5.5, 5, 6, 7, and 8 mm, with a nozzle opening of 9.5 mm. This design differs only in Chap. 3 where a straight channel is used (see Fig. 3.2).

Plasma expands out of the high pressure source (10^4 Pa in the cathode region) into a meter long, 40 cm diameter vacuum vessel. During operation, the background pressure is typically 1-5 Pa. An axial magnetic field directed away from the source confines the plasma to form a ~ 1 cm diameter beam. The field strength can be varied continuously from 0.01-0.1 T and in steps of 0.4 T from 0.4-1.6 T. The magnetic field duration is limited by the cooling of the coils and has a maximum of 160 seconds for 0.4 T and 9.9 sec-

* 1 slm $\approx 4.5 \cdot 10^{20}$ particles/s

ends at 1.6 T. The plasma beam extends to the opposite end of the vessel at 0.5 m distance where it impinges on a water-cooled, removable target. The particle flux to the target is typically $10^{24} \text{ m}^{-2}\text{s}^{-1}$, with a heat flux of $\sim 10 \text{ MW}$. Radial electron and temperature profiles are approximately Gaussian, with peak values in the range $T_e = 0.3 - 3 \text{ eV}$ and $n_e \approx 5 \cdot 10^{19} - 5 \cdot 10^{21} \text{ m}^{-3}$.

2.1.2 Diagnostics

Thomson scattering

Radial electron temperature and density profiles of the Pilot-PSI beam are measured routinely with Thomson scattering [5]. Full details of this diagnostic can be found in [6; 7]. The diagnostic is based on the scattering of laser light from free electrons in the plasma. The spectrum of this scattered light is Doppler broadened due to the velocity distribution of the electrons. From the Doppler width of the spectrum, the electron temperature can therefore be obtained. The electron density can also be determined; it is proportional to the intensity of the scattered light.

Measurements are made at two fixed axial positions, $\sim 4 \text{ cm}$ from the source and $\sim 2 \text{ cm}$ from the target, as determined by the position of the laser beam. The laser used is a neodymium doped yttrium aluminium garnet (Nd:YAG) laser operating at the second harmonic (532 nm), with a pulse rate of 10 Hz and energy of 0.4-0.5 J/pulse. Scattered light is collected at an angle of 90 degrees and focused onto a quartz fiber array using a double lens system. The effective focal length is 160 mm and the lens diameter is 8.15 cm. The magnification is 0.66. The fiber array consists of 48 fibers, each with a diameter of 0.4 mm. A 30 mm chord of the plasma beam can thus be measured with a spatial resolution of 0.6 mm.

The signal is analyzed with a spectrometer in Littrow configuration. A two-dimensional output signal results (with spatial and spectral resolution) that is amplified by an image intensifier and recorded on an intensified CCD (ICCD) camera. The first image intensifier is gated such that signal is only recorded in a 30 ns time window around each $\sim 7 \text{ ns}$ laser pulse. The total signal recorded over the duration of the magnetic field pulse (typically 3 seconds) is absolutely calibrated with Rayleigh scattering. For this calibration, the vessel is filled with argon at a pressure of 50 Pa. The stray light signal is measured separately and is subtracted from the raw measurement signal. A wavelength calibration of the detection system is performed by illumination with a tungsten lamp [8].

Optical emission spectroscopy set up

Optical emission spectroscopy measurements (see for example [9; 10; 11; 12; 13; 14; 15]) were performed to obtain temperature and velocity information on $n=3$ and $n=4$ excited hydrogen atoms. Spontaneous emission on either the Balmer- α or the Balmer- β line was collected and spectrally analyzed. Temperatures could be calculated from the Doppler broadening of the spectra. Velocities were obtained from the Doppler shift with respect to the reference spectrum from a hydrogen lamp.

For the optical emission spectroscopy diagnostic, light is collected with a lens system and imaged onto an array of 40 individual 0.4 mm diameter quartz fibers, thus recording a radial profile of the beam. A polarizer mounted in front of the fibers selects the π -component of Zeeman-split spectral lines [16]. For measurements of the rotation velocity, the collection angle is perpendicular to the jet axis. The viewing system in Chap. 3 had a magnification of 0.4, and a lens with diameter 6 cm and focal length 20 cm. For rotation measurements in other chapters, the magnification was 0.55 and a double lens system was used with lens diameter 8.15 cm and effective focal length 160 mm. For the axial measurements in Chap. 6, the same lenses were used and a square mirror (10×12 cm) was mounted in the vessel to ensure a collection angle of 13 degrees to the jet axis. The magnification was between 0.225 and 0.26.

Collected light is relayed via the optical fiber array to a spectrometer in Littrow configuration. In this way, spatial information is preserved and a spectral range of approximately 4 nm can be investigated over the entire 2–3 cm width of the plasma jet profile simultaneously. The output of the fiber array is imaged onto an adjustable slit. Behind the slit, light is collimated by an achromatic lens of 15 cm in diameter with a focal length of 2.25 m. The blazed diffraction grating is optimized for the second diffraction order (blaze angle 17.45°). It has dimensions of 11 x 11 cm and a groove density of 1200 per mm. The signal is detected on a CCD (Charged Coupled Device) camera. For the measurements in Chap. 3 the camera consists of 298×1152 pixels of size $22.5 \times 22.5 \mu\text{m}$. For other chapters a CCD camera with 2048×2048 pixels, $13.5 \times 13.5 \mu\text{m}$ in size was used. The exposure time of the CCD camera is several seconds. Fast temporal fluctuations are thus averaged. The wavelength resolution is determined predominantly by the slit width. For a $50 \mu\text{m}$ slit, the wavelength resolution is ~ 6 pm for Balmer- α and ~ 8 pm for Balmer- β .

Absorption spectroscopy and Laser Induced Fluorescence

Absorption spectroscopy and Laser Induced Fluorescence (LIF) [17; 18; 19; 20; 21; 22] were used to obtain density measurements of the $n=2$ excited atoms. The optical set-up for absorption and LIF is depicted in Fig. 4.2. Absorption was measured on the Balmer- α line from excited level $n=2$ to $n=3$. The LIF signal measured was the spontaneous radiative decay back to the $n=2$ level. We used a tunable external cavity diode laser (Vortex 6000, New Focus, wavelength range: 656.33–656.60 nm, horizontal polarization, spectral linewidth < 300 kHz). The laser power and wavelength were monitored real time, the latter with a Fabry-Perot cell. The laser was always at an angle to the windows to minimize interference effects. Scans as a function of electron density were mostly performed with an expanded laser beam (laser spot diameter up to $\phi = 1$ cm) with the aim of maximizing the fluorescence signal for LIF. Lateral scans across the width of the beam were performed with laser diameter $\phi < 1.5$ mm.

For absorption, the laser was scanned across the width of the plasma beam to obtain a lateral profile, by adjustment of the angle of the last mirror in front of the vessel. After a single pass through the plasma beam, the laser beam was focused onto a photodiode which measured the transmitted laser power. This photodiode was positioned at 1.5 m from the vessel to suppress background emission. The collection optics were adjusted

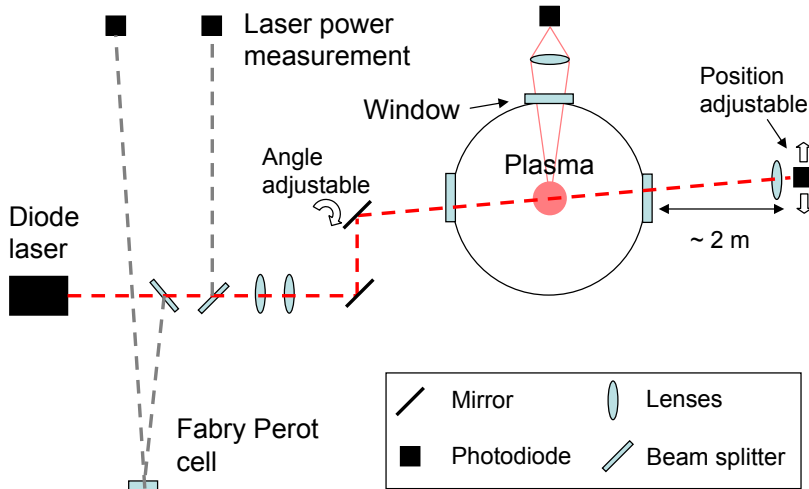


Figure 2.3: Diagnostic set-up for absorption spectroscopy and Laser Induced Fluorescence

during a radial scan, so that the laser beam was always focused onto the photodiode. The laser wavelength was scanned across the spectrum with a repetition frequency of 10 Hz with 10 averages. Directly following each measurement a calibration measurement was made with the magnetic field turned off. This reduced the laser absorption to $\ll 10^{-5}$.

Fluorescence was also collected onto a photodiode. Since the background emission was expected to be more than 1000 times stronger than the fluorescence, several techniques were employed to suppress it. Firstly lock-in detection was used with a mechanical chopper at 4 kHz, a spectrum scan at 0.05 Hz and a typical integration time of two seconds. Also, both a Balmer- α filter and a slit were mounted in front of the photodiode such that only relevant light from regions where fluorescence was expected was imaged onto the photodiode.

References

- [1] H. Maecker, "Ein zylindrischer bogen für hohe leistungen," *Z. Naturforsch.*, vol. 11a, no. 457, 1956.
- [2] M. C. M. van de Sanden, J. M. de Regt, G. M. Janssen, J. J. A. M. van der Mullen, D. C. Schram, and B. van der Sijde, "A combined Thomson-Rayleigh scattering diagnostic using an intensified photodiode array," *Rev. Sci. Instrum.*, vol. 63, pp. 3369–3377, 1992.
- [3] G. M. W. Kroesen, D. C. Schram, and J. C. M. de Haas, "Fast deposition of amorphous hydrogenated carbon films using a supersonically expanding arc plasma," *Plasma Chem. Plasma Proc.*, vol. 10, p. 531, 1990.
- [4] M. de Graaf, Z. Qing, H. Tolido, and D. Schram, "A cascaded arc atomic hydrogen source," *J. High Temp. Chem. Processes*, vol. 1, p. 11, 1992.
- [5] J. Sheffield, *Plasma Scattering of Electromagnetic Radiation*. Academic, New York, 1975.
- [6] H. J. van der Meiden *et al.*, "High sensitivity imaging Thomson scattering for low temperature plasma," *Rev. Sci. Instrum.*, vol. 79, p. 013505, 2008.
- [7] G. J. van Rooij *et al.*, "Thomson scattering at Pilot-PSI and Magnum-PSI," *Plasma Phys. Controlled Fusion*, vol. 51, p. 124037, 2009.
- [8] C. J. Barth, C. C. Chu, M. N. A. Beurskens, and H. J. van der Meiden, "Calibration procedure and data processing for a TV Thomson scattering system," *Rev. Sci. Instrum.*, vol. 72, no. 9, 2001.
- [9] T. Fujimoto, *Plasma Spectroscopy*. Clarendon Press Oxford, 2004.
- [10] H. R. Griem, *Principles of Plasma Spectroscopy*. Cambridge University Press, 1997.
- [11] H. R. Griem, *Plasma Spectroscopy*. New York: McGraw-Hill, 1964.
- [12] U. Fantz, "Basics of plasma spectroscopy," *Plasma Sources Sci. Technol.*, pp. S137–S147, 2006.
- [13] J. J. Leijssen, "Rotation velocities of magnetized plasma in a linear plasma generator," Bachelor Thesis, Saxion Hogescholen Academy Life Science, Engineering and Design, 2008.
- [14] A. H. van den Langenberg, "Analysis of the Pilot-PSI plasma using optical emission spectroscopy," Masters Thesis, Universiteit Utrecht, 2008.
- [15] N. den Harder, Masters Thesis, Universiteit Utrecht, 2011.

- [16] T. Fujimoto and A. Iwamae, *Plasma Polarization Spectroscopy*. Springer, 2007.
- [17] J. Biesheuvel, “Laser induced fluorescence and absorption in the magnetized plasma jet of Pilot-PSI,” Masters Thesis, Universiteit Utrecht, 2009.
- [18] A. J. M. Buuron, *Plasma deposition of carbon materials*. PhD thesis, Technische Universiteit Eindhoven, 1993.
- [19] W. Demtröder, *Laser Spectroscopy, Basic Principles*, vol. 1. Springer-Verlag, 2008.
- [20] A. Rousseau, E. Teboul, and N. Sadeghi, “Time-resolved gas temperature measurements by laser absorption in a pulsed microwave hydrogen discharge,” *Plasma Sources Sci. Technol.*, vol. 13, pp. 166–176, 2004.
- [21] J. G. Liebeskind, R. K. Hanson, and M. A. Cappelli, “Laser-induced fluorescence diagnostic for temperature and velocity measurements in a hydrogen arcjet plume,” *Appl. Optics*, vol. 32, no. 30, 1993.
- [22] G. van der Star, Masters Thesis, Universiteit Utrecht, 2011.

Chapter 3

Rotation of a strongly magnetized hydrogen plasma column determined from an asymmetric Balmer- β spectral line with two radiating distributions*

Abstract

A potential build up in front of a magnetized cascaded arc hydrogen plasma source is explored via $\vec{E} \times \vec{B}$ rotation and plate potential measurements. Plasma rotation approaches thermal speeds with maximum velocities of 10 km/s. The diagnostic for plasma rotation is optical emission spectroscopy on the Balmer- β line. Asymmetric spectra are observed. For the first time a detailed consideration is given on the interpretation of such spectra with a two distribution model. This consideration includes radial dependence of emission determined by Abel inversion of the lateral intensity profile. Spectrum analysis is performed considering Doppler shift, Doppler broadening, Stark broadening and Stark splitting.

*Published as: A. E. Shumack, V. P. Veremiyenko, D. C. Schram, H. J. de Blank, W. J. Goedheer, H. J. van der Meiden, W. A. J. Vijvers, J. Westerhout, N. J. Lopes Cardozo and G. J. van Rooij, Phys. Rev. E **78**, 046405 (2008). Small changes in this thesis: layout of some figures changed, some black and white figures are now in colour. Fig. 3.1 has been adjusted to give a more accurate depiction of the plasma beam.

3.1 Introduction

A potential build-up at the exit of the magnetized cascaded arc hydrogen plasma source of Pilot-PSI has been shown to lead to high fluxes and a high source efficiency [1]. This has facilitated the production of unique plasma conditions. Pilot-PSI reproduces the hydrogen plasma conditions expected in the diverter of the international fusion experiment ITER, in a linear machine. Particle fluxes of up to $10^{24} \text{ m}^{-2}\text{s}^{-1}$ are obtained with energy fluxes up to 10 MW/m^2 and electron temperatures of $1 - 5 \text{ eV}$. Plasma surface interaction research in support of ITER is currently being carried out [2; 3].

The cause of the potential build up at the exit of the source is the source current path, which in contrast to similar linear plasma devices does not lie entirely within the source itself. The path of the electron current from the cathodes must cross the magnetic field in the radial direction to reach the anode. Due to magnetic confinement, the plasma resistivity in the radial direction is higher than in the axial direction. To follow the path of least resistance, the electron current spreads itself out in the axial direction until the effective radial resistance is the same as the axial resistance. Electric fields associated with the current path drive plasma rotation via an $\vec{E} \times \vec{B}$ force.

$\vec{E} \times \vec{B}$ drift rotation has been well studied in the literature [4; 5; 6; 7; 8]. As already indicated in [1], rotation velocities in Pilot-PSI can be up to 10 km/s , one order of magnitude higher than expected from the ambipolar fields. This paper reports on the measurements of plasma rotation, which form the basis of an exploration of the potential build-up in front of the source.

The plasma rotation is studied by Optical Emission Spectroscopy (OES). Direct passive spectroscopy is not possible for hydrogen ions which do not radiate. Instead we analyze the light emitted by the neutral atoms. This approach was successfully followed by others (e.g. Meyer et al.[6]) by virtue of an efficient coupling of the excited atoms to the ions via fast symmetric charge exchange.

Asymmetry is observed in the Balmer- β spectra measured for the high density, magnetized hydrogen plasma under study. Asymmetric spectra have been observed earlier [4; 7; 9; 10; 11] and analyzed with the assumption of two radiating populations. The assumption of two distributions is given a thorough consideration in this paper for the plasma conditions present.

The method of spectrum analysis is assessed on the basis of the residue of the fitting procedure and the plasma densities and temperatures that it predicts. Thomson scattering measurements form the basis of quantitative comparison.

In section 3.2, the plasma device is described and the experimental conditions given. Section 3.3 presents the optical emission spectroscopy measurements, explains the method of spectrum analysis and gives the results. Section 3.4 explores the mechanisms behind the light production and the shape of the spectral emission line. The rotation of the plasma in relation to the radial electric field which causes it is discussed in section 3.5.

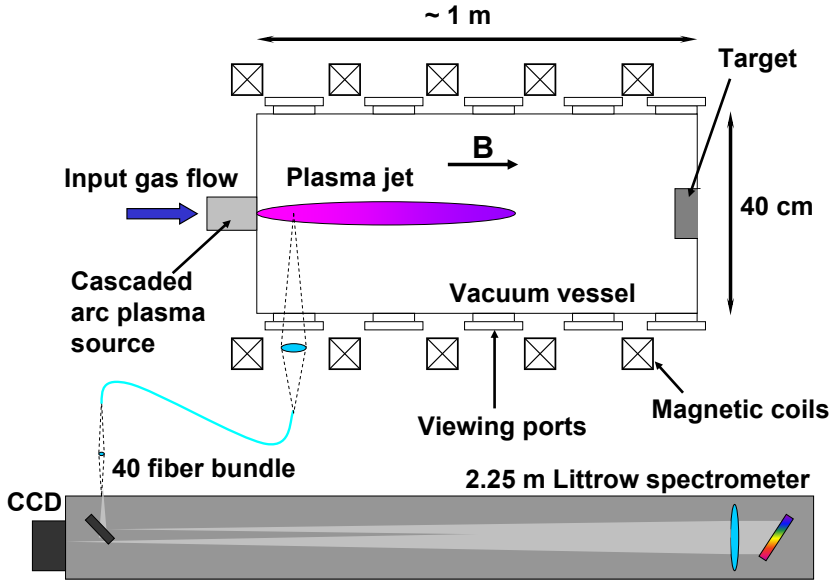


Figure 3.1: Schematical drawing of the experimental arrangement of Pilot-PSI and its optical emission spectroscopy diagnostic.

3.2 Experimental

3.2.1 The linear plasma generator Pilot-PSI

The hydrogen plasma under study in this work was produced in the linear plasma generator Pilot-PSI [1]. Figure 3.1 shows the experimental arrangement of Pilot-PSI and the emission spectroscopy diagnostic.

Plasma is produced with a cascaded arc, see Fig.3.2. Its design is based on extensive work at the Eindhoven University of Technology [12; 13]. Hydrogen flows at 2.5 standard litres per minute or 10^{21} H₂/s through a discharge channel, 32 mm long and 4 mm in diameter. A discharge current is stabilized to 80 A between three tungsten cathodes and a 5-8 mm diameter copper-tungsten nozzle that serves as the anode. Unless stated otherwise, the nozzle diameter for the measurements presented in this paper is 8 mm. The plasma expands out of the high pressure source (10^4 Pa in the cathode region) into a 1 m long, 40 cm diameter vacuum vessel. During operation, the background pressure is typically 1-5 Pa. An axial magnetic field directed away from the source with a variable strength in steps of 0.4 T to a maximum of 1.6 T confines the plasma to form a jet. The magnetic field duration is limited by the cooling of the coils and is set to 30 seconds for 0.4 T and 3 seconds for higher fields. The plasma beam extends to the opposite end of the vessel where it impinges on a water-cooled target. The potential distribution over

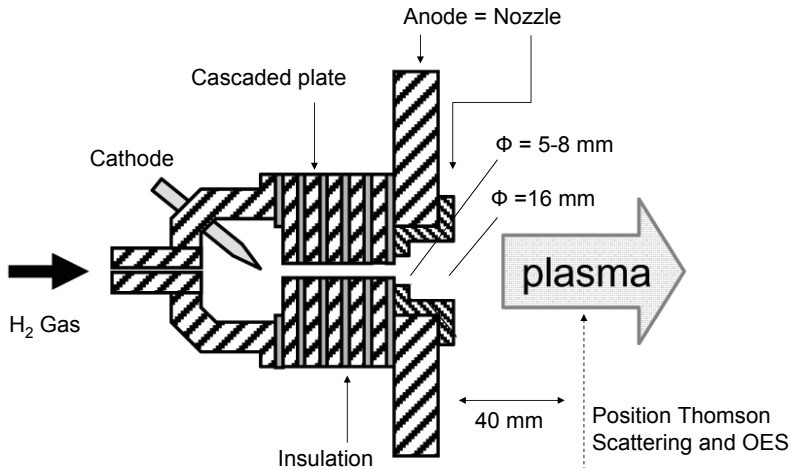


Figure 3.2: The cascaded arc plasma source. The working gas enters the plasma source via the gas inlet. It is ionized in the arc channel of the cascaded plates due to the discharge between the three cathodes and the anode. The nozzle is electrically connected to anode which is attached to the vessel wall. Plasma exits the source through the nozzle. Thomson scattering and OES measurements are performed at 40 mm from the nozzle.

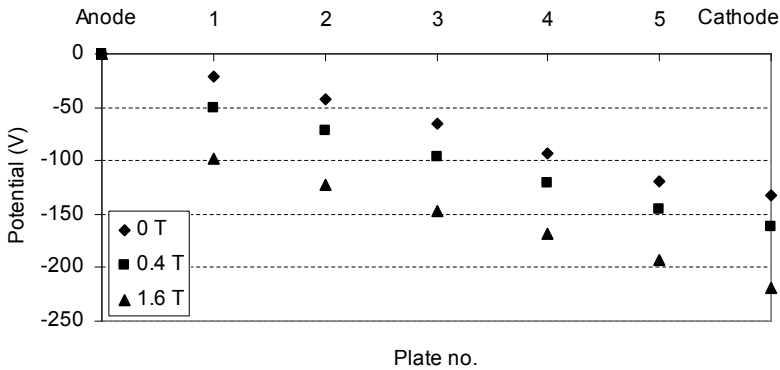


Figure 3.3: A potential distribution over cascaded plates in a hydrogen plasma. In a magnetic field the voltage over the arc is significantly higher. The extra voltage drops mainly between the anode and the first plate.

the cascaded arc plates is shown in Fig. 3.3 for different magnetic field values. Without magnetic field, the 130 V discharge potential is distributed evenly over all plates. A magnetic field only affects the potential difference between the anode and the first cascaded plate. The electron temperature (T_e) and density (n_e) of the plasma are measured with

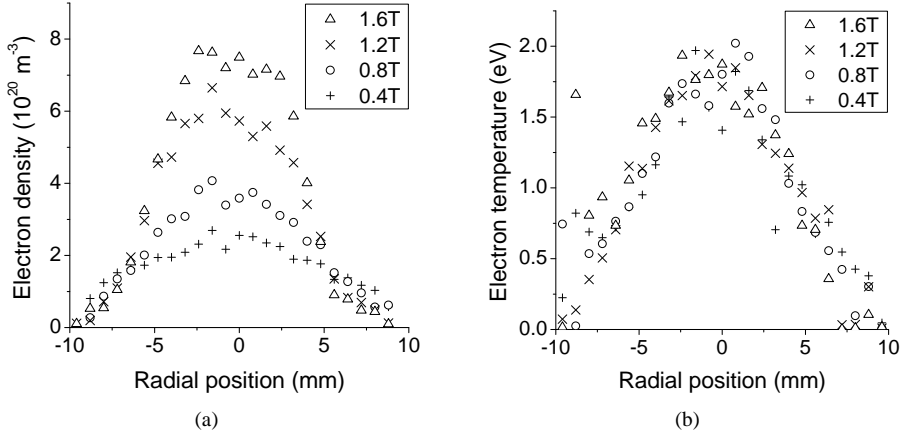


Figure 3.4: The radial electron (a) density and (b) temperature profiles of the hydrogen plasma jet measured with Thomson scattering at 40 mm from the source in a magnetic field of 0.4, 0.8, 1.2 and 1.6 T.

Thomson scattering at 40 mm from the nozzle of the source. Full details of this diagnostic can be found in [14]. Thomson scattering is performed with a 532 nm Nd:YAG second harmonic laser at 10 Hz with 0.4 J/pulse. The signal is averaged over the duration of the magnetic field pulse. A fiber array is used to collect the scattered light so that the entire plasma diameter is observed simultaneously in 40 channels. The Thomson scattering spectra are absolutely calibrated with Rayleigh scattering on argon in the vessel at a pressure of 50 Pa. The electron density and temperature profiles at the four magnetic field settings discussed in this paper are shown in Fig. 3.4. The electron density increases with increasing magnetic field because of improved plasma confinement. This can also be seen in the narrowing of the density profiles. The influence of the magnetic field on the temperature profile is minimal. For a discussion of these plasma conditions, see [1].

3.2.2 Optical emission spectroscopy set up

The OES arrangement is depicted in Fig. 3.1. Plasma light is collected at an axial distance of 40 mm from the nozzle of the source with a lens (diameter 6 cm, focal length 20 cm) in the direction perpendicular to the jet axis, at magnification $M=0.4\times$. A polarizer selects π -components of Zeeman-split spectral lines. An array of 40 individual 0.4 mm diameter quartz fibers relays the collected light to an in-house constructed, single-pass spectrometer in Littrow configuration. In this way, spatial information is preserved

and a spectral range of approximately 1 nm can be investigated over the entire 2–3 cm width of the plasma jet profile simultaneously.

The output of the fiber array is imaged on an adjustable slit. Behind the slit, light is collimated by an achromatic lens of 15 cm in diameter with a focal length of 2.25 m. The blazed diffraction grating is optimised for the second diffraction order (blaze angle 17.45°). It has dimensions of 11 x 11 cm and a groove density of 1200 per mm. The signal is detected on a 298x1152 pixel CCD (Charged Coupled Device) camera. The instrument function of the spectrometer, determined with He-Ne laser light, has a width smaller than 0.003 nm (full width at $1/e$), corresponding approximately to 1 pixel at the wavelength of the Balmer- β transition.

The exposure time of the CCD camera is several seconds, the maximum time allowed by the duration of the magnetic field pulse. Fast temporal fluctuations are thus averaged. These fluctuations were studied in an independent experiment using a photodiode. Variations of typically $\pm 30\%$ with respect to the mean value were observed with a frequency of close to 1 MHz.

This paper reports on spectroscopy data taken at one axial position, at 4 cm from the nozzle of the plasma source. Although not presented in this paper, the plasma parameters do display axial dependence. The ion rotation velocity decreases in the axial direction with a characteristic decay length of about half a meter. The reason for the decrease is the penetration depth of the electric field which causes it, as explained in section 3.5. The temperature and density also decrease slowly along the axis due to plasma recombination.

3.3 Spectrum analysis

In this section we develop the methodology for interpretation of the OES data. We start with a detailed consideration of a representative measurement.

3.3.1 Measured Balmer- β line shape and intensity profile

Figure 3.5(a) shows a typical OES measurement at a magnetic field of 1.6 T. Here, we see part of a raw CCD-image of the spatially (vertical axis) as well as spectrally (horizontal axis) resolved Balmer- β line, indicating plasma rotation. The complete width of the CCD-image corresponds approximately to 1 nm around the wavelength of the Balmer- β line. Only the central part of ~ 0.35 nm is shown in the figure. The vertical axis is the spatial coordinate, in the lateral direction (perpendicular the plasma propagation), spanning approximately 40 mm, about 16 mm of which is shown in the figure. We call this the ‘lateral direction’, distinguishing it explicitly from the ‘radial direction’ because the measurement is a line of sight integration. The different bands in the CCD image correspond to the individual fibres in the array. The finer structures within these bands are due to imperfections in the spectrometer slit. The spectral lines appear Doppler shifted to the red at the bottom of the plasma jet and to the blue at the top, indicating rotation of the radiating species. Towards the edges of the beam the rotation is damped and the profile

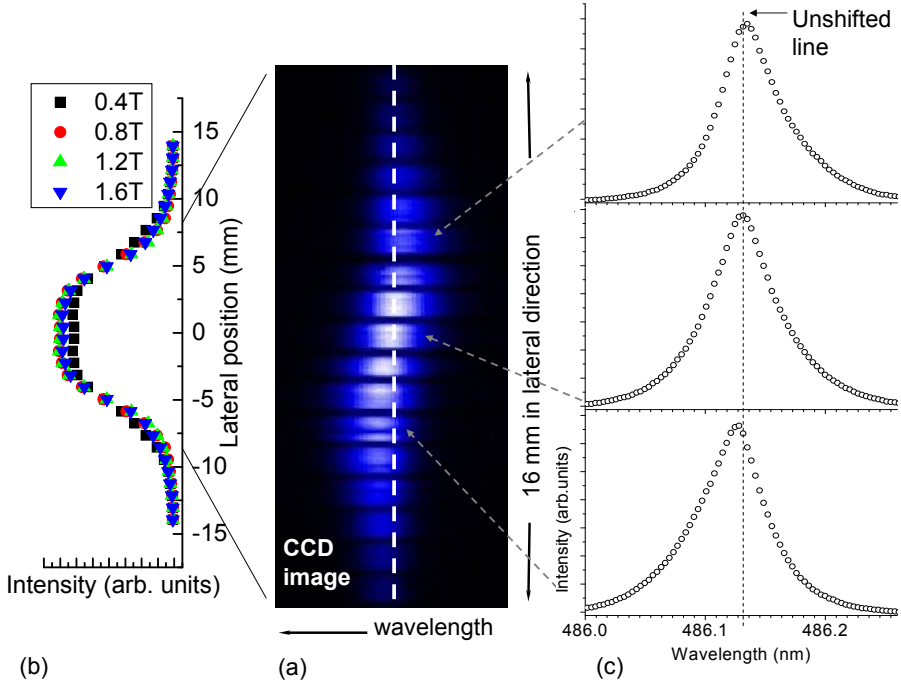


Figure 3.5: A typical OES measurement at a magnetic field strength of 1.6 T. (a) Part of a raw CCD-image of the spectrally as well as spatially resolved Balmer- β light, indicating plasma rotation. The 17 bands of light correspond to individual optical fibres. The spectral line appears shifted to the red at the bottom of the plasma jet and to the blue at the top. At the jet edges it is unshifted. The spectral shift reveals rotation of the radiating species. The maximum Doppler shift from the central wavelength value is about five pixels. This corresponds to a velocity of $9.3 \text{ km/s} \pm 10\%$ (b) The corrected lateral intensity profile displaying a flat top, pointing to a hollow emission profile. (c) Spectral profiles from respectively above, on and under the jet axis. The off-centre profiles are clearly asymmetric, with the direction of asymmetry depending on the lateral position. In the jet centre, the profile is symmetric.

is unshifted. The direction of rotation is clockwise as viewed from the source, looking towards the target.

We can estimate the value of the maximum rotation velocity at 1.6 T from Fig. 3.5(a). We focus on the off-centre fibre images with the largest wavelength shift. Their entire Doppler broadened band appears to be shifted from the central line by approximately five pixels. This corresponds to a Doppler shift of 0.015 nm at the wavelength of the Balmer- β transition and a velocity of 9.3 km/s \pm 10%.

Fig. 3.5(b) shows the lateral intensity profile corresponding to the entire CCD image. This was obtained by integration over the wavelength axis of the CCD image and over the spatial band corresponding to each fiber. The intensity profiles measured at other magnetic field strengths are plotted on the same graph. We corrected for variations in the transmittance of the individual fibers. A cut-off in the spectrometer throughput at the lower fibers (left side of the profile) was corrected for by mirroring the right side of the profile to the left.

We observe that the intensity profiles do not change significantly as the magnetic field and thereby also the electron density is varied. Furthermore, the profiles are flat in the center which points to a hollow emission profile. Abel inversions of the intensity profile are given in section 3.3.2, along with the implications of a hollow emission profile shape. The mechanisms leading to the hollow emission profiles are set out in section 3.4.2.

In Fig. 3.5(c) typical spectral emission lines are shown corresponding to different lateral positions. The line profile in the middle of the plasma column is symmetric, off-centre the profiles are shifted and become asymmetric. This asymmetry is caused by the presence of two populations of radiating (excited) neutrals, one hot, rotating and coupled to the ions, the other cold and only slowly rotating. The profiles can hence be fit with a double Voigt function to obtain information on rotation velocity, temperature and density. The fit methodology is described in section 3.3.3.

3.3.2 Hollow emission profile

Figures 3.6(a) and 3.6(b) show the lateral intensity profiles for a magnetic field of 0.4 T and 1.6 T respectively. We perform a fit of the profiles with the sum of two Gaussian profiles, one of which is inverted. The fit approximates the edges of the intensity profile better for 0.4 T than for 1.6 T. Abel inversion of the lateral intensity profile gives the radial emission profile. Since Gaussian functions are invariant under Abel inversion [15], the chosen fit function allows for simple analysis. Abel inversion does not affect the shape of the Gaussian functions themselves, only changes the ratio between them. We see the result in Fig. 3.7 for all four magnetic field values. The profiles are clearly hollow. In section 3.4.2 we show that this can be expected from a balance of the plasma processes present.

The practical consequence of the hollow emission profile is that the strongest light emission does not occur at the centre of the jet where the electron density is highest. As shown in Fig. 3.7, most light collected is emitted from a ring, at a position where the electron density and temperature are substantially lower than the maximum value.

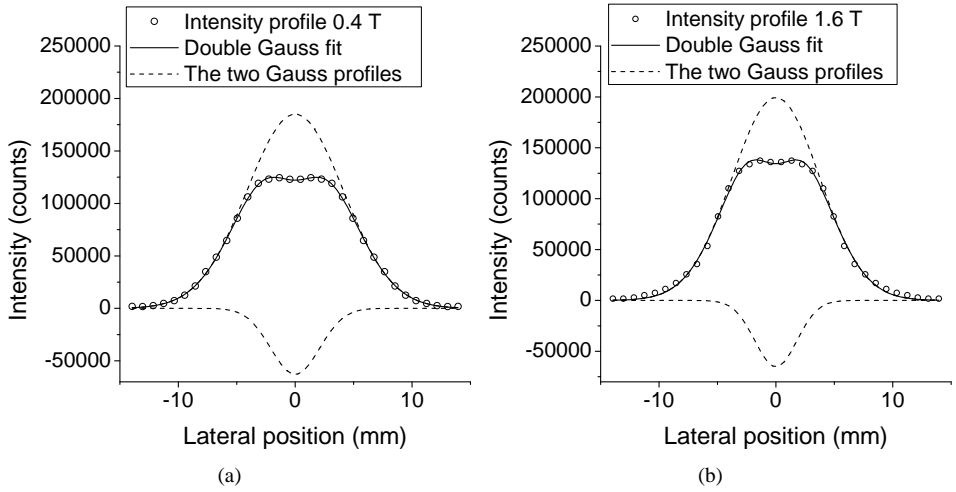


Figure 3.6: Lateral intensity profiles at (a) 0.4 T and (b) 1.6 T. Data is fit with the sum of two Gauss profiles, one of which is inverted.

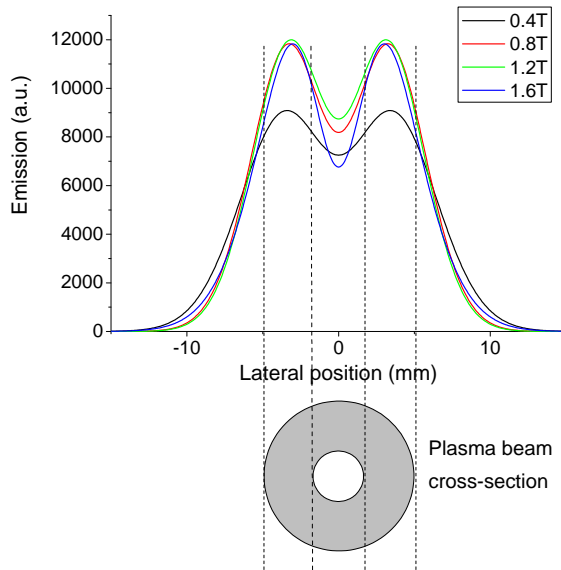


Figure 3.7: Radial emission profiles for the four magnetic field values, obtained by Abel inverting the fit of the intensity profiles. Emission profiles are clearly hollow in the centre of the plasma beam. A schematic cross-section of plasma beam is shown indicating positions of strongest emission by shading.

3.3.3 Asymmetric line profile: double Voigt fit

In section 3.3.1, Fig. 3.5(c) we saw that the emission profiles above and below the plasma axis are asymmetric. The direction of this asymmetry is reversed for profiles recorded above the plasma jet axis as compared to those recorded below the axis. We fitted these profiles assuming two populations of radiating hydrogen atoms, a procedure also followed by [7; 10; 11], see Fig. 3.8.

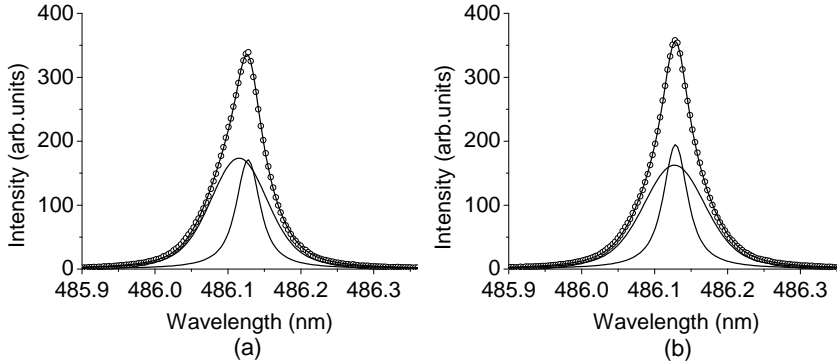


Figure 3.8: A double Voigt fit of spectra taken at 1.6 T from (a) below the jet axis (b) on the jet axis. The two single Voigt components are shown, one corresponding to the hot, rotating population, the other to the cold and almost non-rotating population.

One population is coupled to the ions. It is 'hot', with a temperature of several eV, and rotates at high speed, up to 10000 m/s. The other is 'cold' - 0.1 to 0.5 eV - and rotates only very slowly, at maximum 10% of the velocity of the hot component.

We fitted the spectrum from each population with a Voigt profile, the convolution between a Gauss and a Lorentz profile. This is required for the plasma densities and temperatures in our plasma, where both Doppler broadening (Gaussian) and Stark broadening (Lorentzian) of the Balmer- β spectral line are important. For example, at a temperature of 1 eV and a density of 10^{20} m^{-3} the Gaussian from Doppler broadening has a FWHM (Full Width Half Maximum) of 37.4 pm. The Lorentz profile from Stark broadening of the Balmer- β line has a FWHM of 36.6 pm [16].

In our double Voigt fitting procedure, 8 parameters are left free: these are the baseline (offset), the amplitudes (or areas) of the two Voigt components, their Doppler widths and one Lorentz width (the same for both), the exact position of the 'cold' component and the shift of the 'hot' component with respect to the 'cold' one. We take the same Lorentz width for both components because total free fits return equal values for these two fit parameters. Also, the ratio between the amplitudes of the hot and cold components remains constant along the lateral direction indicating that the emission from both components originates from the same position. From the double Voigt fit we are able to obtain the ion

rotation velocity and temperature from respectively the spectral shift and Doppler width of the 'hot' component. The electron density is determined from the Lorentz width, but as we will see in section 3.3.5 this quantity is not well determined.

A double Voigt fit shows improvement compared to a single Voigt fit as seen in Fig. 3.9. The residues are smaller, around 1%, and more stochastic. The remaining struc-

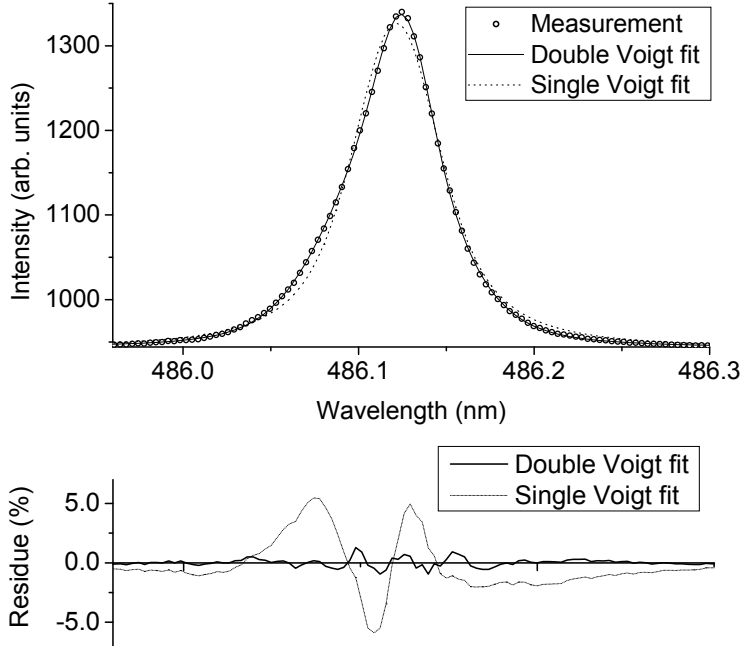


Figure 3.9: An off-centre asymmetric Balmer- β -line fitted with a single and a double Voigt profile ($B = 1.2$ T). The residues for the double Voigt fit are significantly smaller and more stochastic.

ture in the very small residue can be understood as an artifact of the instrument function.

3.3.4 Results and discussion for rotation and ion temperature

Figure 3.10 shows the results for the ion rotation. Rotation velocities of up to 10 000 m/s, are obtained for the highest magnetic field strength, 1.6 T. This is conform to estimates from the raw CCD image in Fig. 3.5(a). As shown in section 3.5 electric field strengths are available to drive $\vec{E} \times \vec{B}$ rotation of this magnitude.

The peak rotation velocities have values up to a half of the ion acoustic velocity in which range ion viscous heating [5; 7; 17] becomes significant. Ion neutral friction and charge exchange are responsible for damping of the rotation towards the edges of the

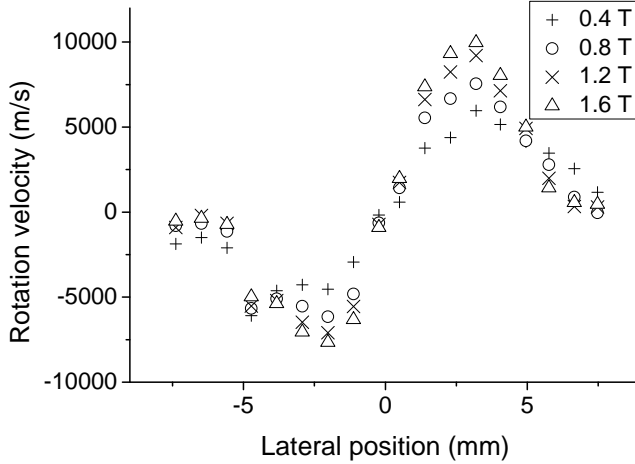


Figure 3.10: Lateral profiles of rotation velocity determined from a double Voigt fit of the Balmer- β line shape at magnetic field strengths of 0.4 T, 0.8 T, 1.2 T and 1.6 T.

beam while heating the neutrals. This enhancement of velocity shear significantly enhances ion viscous heating. Ion temperatures are indeed somewhat higher than the electron temperature given in Fig. 3.4. The results of the double Voigt fit for ion temperature are given in Fig. 3.11.

We estimate the strength of the viscous heating to determine whether it is indeed an important heating channel. The viscous heating term is given by Braginskii [18]:

$$Q_{visc} = -\Pi_{\alpha\beta} \frac{\partial v_{\alpha}}{\partial x_{\beta}} \quad (3.1)$$

where $\Pi_{\alpha\beta}$ is the stress tensor. We take $\partial v_{\theta}/\partial R$ to be the largest systematic component. For Hall factor $\omega_{ci}\tau_{ii} \sim 1$, true for all plasma conditions under study, this term is of the order:

$$Q_{visc} \sim n_i k_B T_i \tau_{ii} \left(\frac{v_{i\theta}(R)}{R} \right)^2 = \frac{e \hat{T}_i^{5/2} \cdot 2 \cdot 10^{13} \Omega_i^2}{\ln \Lambda} \quad (3.2)$$

where we have approximated $\partial v_{i\theta}(R)/\partial R$ by $v_{i\theta}(R)/R$. n_i is the ion density [m^{-3}], k_B is Boltzmann's constant [J/K], T_i is the ion temperature [K], τ_{ii} is the ion-ion collision time [s], v_{θ} is the azimuthal velocity [m/s], R is the radius [m], e is electron charge [C], \hat{T}_i is the ion temperature [eV], Ω is the rotation frequency [rad/s] and $\ln \Lambda$ is the Coulomb logarithm. Filling in values for the off axis plasma, $r = 2\text{mm}$, at a magnetic field of 1.2 T gives Q_{visc} in the order of 10^8 W/m^3 .

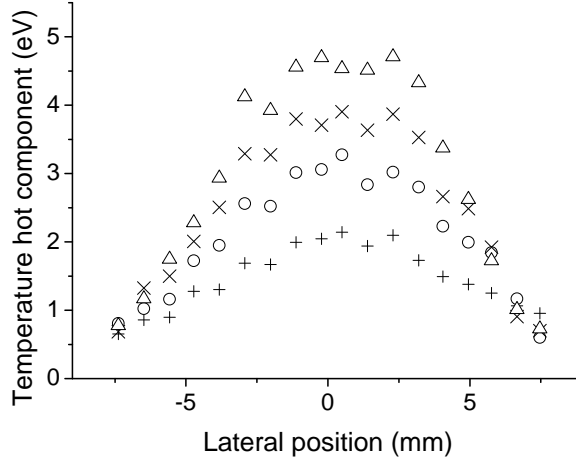


Figure 3.11: Lateral profiles of ion temperature determined from a double Voigt fit of the Balmer- β line shape at magnetic field strengths of 0.4 T, 0.8 T, 1.2 T and 1.6 T.

We can judge the importance of viscous heating at the edge of the plasma by comparison with the central heat input by ohmic loss:

$$Q_{ohmic} = \sigma_{\parallel} E_z^2 \quad (3.3)$$

where σ_{\parallel} is the conductivity parallel to the magnetic field and E_z is the axial electric field. Because of magnetic field confinement, the source plasma current penetrates into the vessel as shown in Fig. 3.12. The penetration depth is about half a meter. This current is associated with a strong radial electric field E_r and a weak axial electric field E_z . These fields are discussed in more detail in section 3.5. For an estimation of E_z , we assume an axial potential drop of 50 V (close to half of the source potential). This falls over half a meter, giving $E_z = 100$ V/m. The conductivity from Spitzer [19] is:

$$\sigma_{\parallel} = \frac{2 \cdot 10^4 T_e^{\hat{3}/2}}{\ln \Lambda} \quad (3.4)$$

The result is an Ohmic heating of about 10^8 W/m³, of the same order as viscous heating at the edges. Hence, we conclude that ion viscous heating can be important, the occurrence of which agrees with the observed high ion temperatures.

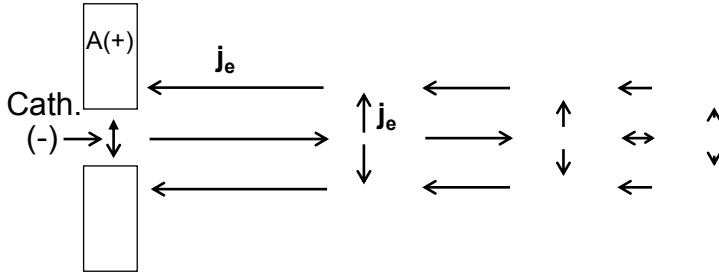


Figure 3.12: The electrons cannot close the circuit within the source due to their limited mobility across the magnetic field. The radial electron current path spreads out in the axial direction until the resistance of the axial and radial current paths are equal.

3.3.5 Assessment of fit based on density and temperature predictions

From Abel inversion of the intensity profiles shown in Fig. 3.7 we know that the radial emission profile of the plasma is hollow. We therefore expect the densities resulting from the fit of the spectra to be lower than the peak electron densities measured by Thomson scattering. This is because most emission originates from a ring towards the edges of the beam where the electron density is lower.

There is uncertainty in the position of the emission ring as determined by Abel inversion. The analysis is very sensitive to the asymptotic behavior of the intensity profile for $r \rightarrow \infty$. Also, the instrument function provides an extra broadening of the profile which is more significant for the narrower inverse Gauss profile than for the broader Gauss profile. Accounting for this effect could either shift the emission ring in the Abel inverted profile to larger or smaller radii.

Keeping this uncertainty in mind, we consider the densities that could be expected from spectra originating from an emission ring at the position determined from Abel inversion. This radial position is approximately 2-6 mm, see Fig. 3.7. Here, the electron density from Thomson scattering ranges from $2 \cdot 10^{20} \text{ m}^{-3}$ up to almost the maximum electron density for each magnetic field strength.

Other densities can be expected from a consideration of the processes behind the formation of a hollow emission profile. Based on a reaction balance, we predict emission to originate from a plasma position with densities ranging between 0.5 and $1.5 \cdot 10^{20} \text{ m}^{-3}$. This is explained in section 3.4.2.

Results for the electron density from the double Voigt fit are shown in Fig. 3.13(a). The peak electron densities lie in the range between $2 \cdot 10^{19} \text{ m}^{-3}$ and $1 \cdot 10^{20} \text{ m}^{-3}$. Especially for low magnetic fields, this is somewhat lower than expected. There are several mechanisms that could explain this.

It is well known that the profile for a purely Stark broadened Balmer- β profile de-

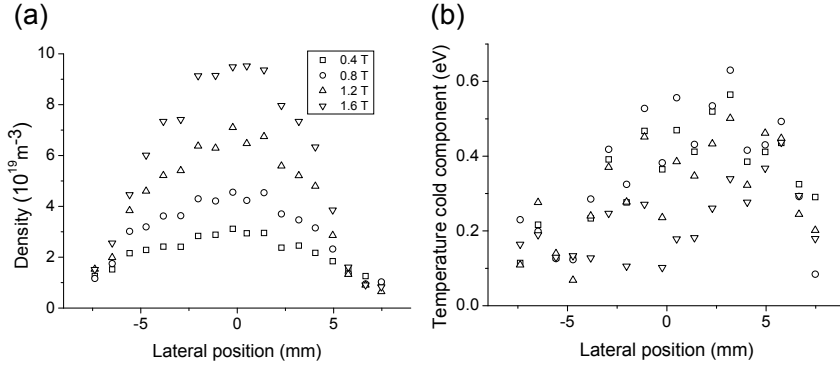


Figure 3.13: Lateral profiles of (a) electron density and (b) temperature of the ‘cold’ neutral population determined from a double Voigt fit of the Balmer- β line shape at magnetic field strengths of 0.4 T, 0.8 T, 1.2 T and 1.6 T.

viates from a single Lorentzian because of Stark splitting [20; 21]. It exhibits structure at its peak (a dip), and thus seems broader than a single Lorentz. If one attempts to fit such a profile with a Voigt function, the Stark part may be partly interpreted as Gaussian because of this extra structure. This effect means that a Gaussian and Stark broadened profile fitted with a double Voigt function may overestimate the Doppler widths and underestimate the Stark width, thus underestimating the electron density. We confirmed that this is a possibility by fitting high density Balmer lines from the literature with a Voigt function. An example is the Balmer- β line from Thomson and Helbig [16] at a density of $8 \cdot 10^{20} \text{ m}^{-3}$ and a temperature of 13500 K. We would expect a Voigt fit of this profile to return a mostly Lorentzian broadened profile. The result of such a fit is in fact a Gaussian component with a width of 137 pm and a Lorentzian width of only 60 pm.

The misinterpretation of part of the Stark profile must of course also have consequences for the ion temperature determination. The total width of the cold Gaussian component can give us an upper limit on the Gaussian interpretation of the density. Here we also take into account the instrument function and a minimum background gas temperature. From the upper limit determined, we conclude that Gaussian interpretation of the density will not cause overestimation of the ion temperature by more than 10%.

To investigate the influence of Stark splitting on the fit, we simulate it by replacing each of the Lorentz components of the double Voigt fit function with two Lorentz profiles shifted with respect to one another. The distance d separating a pair of Lorentz profiles is set at a multiple of the Half Width Half Maximum (HWHM) of a single Lorentz component. This multiple, d , is determined from fits of profiles traced from the literature [16; 20] and from fits of spectral profiles from the Pilot-PSI plasma. The best fits result from a shift d of 1.0 times the HWHM. Such a fit of the Balmer- β spectrum measured by Helbig and Nick [20] for a density of $10.8 \cdot 10^{22} \text{ m}^{-3}$ gives a HWHM of each Lorentz

profile of 1.370 nm. This conversion factor between density and Lorentz width, in combination with experimental scaling $w_L(HWHM) \propto n^{2/3}$ from [22], is the basis of density determination in fits with Stark splitting simulation.

As seen in Fig. 3.14 the density determined from the fit with Stark splitting was higher than without splitting. The values corresponding to the highest and lowest field also lie closer together. Peak densities of $4 \cdot 10^{19} \text{ m}^{-3}$ to $1.1 \cdot 10^{20} \text{ m}^{-3}$ resulted. The residue of the fit remained below 1%. The temperature and rotation were also affected, with a greater spread in the temperature parameter over the different magnetic field values and a smaller spread in the rotation. We note here that the value of the rotation velocity with and without Stark splitting remains the same within about 10%, emphasizing the suitability of the spectral analysis for rotation velocity determination.

The temperature of the ‘cold’ component, shown in Fig. 3.13 is typically $\sim 0.2\text{--}0.4 \text{ eV}$. This is reasonable for a background gas in close proximity to a hot plasma. This temperature may be somewhat overestimated because of a partial Gauss interpretation of the density.

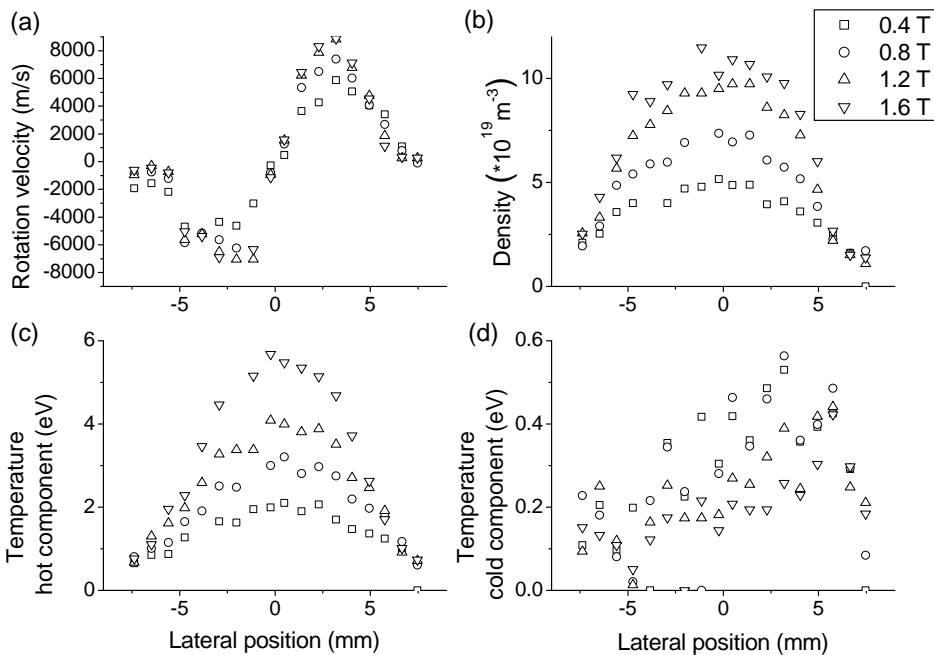
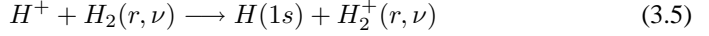


Figure 3.14: Results from a double Voigt fit of the Balmer- β line shape in which each Lorentz profile is replaced by a double Lorentz profile in order to simulate Stark splitting. The lateral profiles shown are of the (a) rotation velocity, (b) electron density (c) ion temperature and (d) ‘cold’ neutral population.

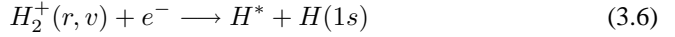
3.4 Consideration of underlying plasma processes

3.4.1 $H^*(n=4)$ production mechanisms

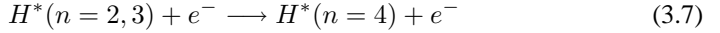
Molecular Activated Recombination (MAR) [23; 24; 25] is a significant production path of excited neutrals under the Pilot-PSI plasma conditions. First, a molecular ion is produced via charge exchange between an ion and a rovibrationally excited background gas molecule:



This is followed by the fast dissociative recombination of the molecular ion resulting in two hydrogen atoms one of which is carrying an excess of internal energy and ends up in at least the $n = 2$ level, or most probably in $n = 3$ [26]:



$H(n = 4)$ is produced by direct fast electron excitation from the $n = 2$ and $n = 3$ levels.



For the prevailing conditions with $n_e = n_i$ of the same order as n_{H_2} , the first step (3.5) in the MAR sequence is the slowest one and sets the rate of MAR. At an electron temperature of 1-2 eV, the rate is $4\text{-}7 \cdot 10^{-17} \text{ m}^3 \text{ s}^{-1}$ [26]. This rate can be one hundred times higher if the hydrogen molecule is vibrationally excited with $\nu \geq 4$ [27]; around $4\text{-}7 \cdot 10^{-15} \text{ m}^3 \text{ s}^{-1}$.

Other possible H^* production mechanisms have lower rates. The rate of direct electron excitation from the ground state to $n = 2$ is: $10^{-17} \text{ m}^3 \text{ s}^{-1}$ at 1 eV and $10^{-16} \text{ m}^3 \text{ s}^{-1}$ at 2 eV. This is in contrast to comparable linear plasma devices, Pisces ($T_e = 3\text{-}35$ eV) [28], NAGDIS-I ($T_e = 5\text{-}10$ eV) [29] and PSI-I ($T_e = 5$ eV) [6], with much higher electron temperatures, where direct excitation is thus important. Three particle recombination having a small reaction rate, but with high densities available, will give a small contribution to the H^* production.

3.4.2 Hollow emission profiles from reaction balance

In this section we show how a hollow radial emission profile follows from the production mechanism of $n=4$ excited atoms and a balance of the reactions involved.

From equations (3.5) and (3.6), radiation and electron de-excitation, the balance of population and de-population processes for H_2^+ ions and $H^*(n = 3)$ excited atoms respectively can be written as:

$$n_{H^+} n_{H_2} \cdot k_{cx} = n_{H_2^+} n_e \cdot k_{dr} \quad (3.8)$$

$$n_{H_2^+} n_e \cdot k_{dr} = n_{H(n=3)} (n_e K_3 + A_3) \quad (3.9)$$

with k_{cx} and k_{dr} denoting the rates of ‘charge exchange’ and ‘dissociative recombination’ respectively, and $K_3 \equiv \sum_{i \neq 3} k_{3i}$, where k_{ij} is the rate of (de-)exitation from the i^{th} to the j^{th} level, $A_3 = \sum_{i < 3} A_{3i}$ and $n \equiv$ density.

From reaction (3.7), radiation and electron de-excitation, the balance of $H^*(n=4)$ is:

$$n_{H(n=3)}n_e \cdot k_{34} = n_{H(n=4)}(n_e K_4 + A_4) \quad (3.10)$$

with $K_4 \equiv \sum_{i \neq 4} k_{4i}$ and $A_4 \equiv \sum_{i < 4} A_{4i}$.

If $n_e > A_3/K_3$ and $n_e > A_4/K_4$ - true for $n_e > 5 \cdot 10^{19} \text{ m}^{-3}$ (data from [30; 31]) - then we can eliminate A_3 and A_4 . Assuming also that $K_3 \simeq k_{34}$, we obtain a balance between underlying processes for $H^*(n=4)$:

$$n_{H^+}n_{H_2}k_{cx} \simeq n_{H(n=4)}n_e K_4 \quad (3.11)$$

Quasineutrality gives $n_e = n_{H^+}$ and thus:

$$n_{H(n=4)}k_{cx} \simeq \frac{n_{H_2}k_{cx}}{K_4} \quad (3.12)$$

At sufficiently high electron densities ($n_e > 5 \cdot 10^{19} \text{ m}^{-3}$) de-excitation of the $H^*(n=4)$ level outweighs radiation. The line emission thereby becomes independent of n_e and depends only on n_{H_2} . According to the Thomson scattering measurements shown in Fig. 3.4, this occurs at a radius of about 8 mm.

The shape of the emission profile above an electron density of $5 \cdot 10^{19} \text{ m}^{-3}$ depends entirely on the shape of the n_{H_2} profile. This profile is hollow, due to the high dissociation degree of the plasma and the short penetration depth of H_2 , limited by charge exchange with neutrals. We estimate the density of H_2 to decrease significantly from a radius of 7 mm inwards and to be fairly well burnt out at a radius of 3-4 mm. This is based on a charge exchange reaction rate of between $4 \cdot 10^{-15} \text{ m}^3 \text{ s}^{-1}$ and $10^{-14} \text{ m}^3 \text{ s}^{-1}$, reasonable estimations for the plasma conditions present. From the work of Vankan [32], we expect the molecular hydrogen in the beam to be highly rovibrationally excited. Krstk [27] shows that vibrational excitation can influence charge exchange reaction cross-sections by a factor of one hundred. We expect rotational excitation to increase the cross-section even further. The charge exchange rate without rovibrational excitation is $4 \cdot 10^{-17} \text{ m}^3 \text{ s}^{-1}$ [26]. Assuming a strong molecular density decay from a radius of 7 mm through to 3-4 mm, and emission being solely dependent on the molecular hydrogen density from a radius of 8 mm inwards, we can expect the strongest radiation at radii of around 7-8 mm, corresponding to electron densities from Thomson scattering (Fig. 3.4) of $0.5 - 1.5 \cdot 10^{20} \text{ m}^{-3}$. The expected emission profile is depicted schematically in Fig. 3.15.

3.4.3 Discussion of two populations

We now consider possible origins of the two (hot and cold) $H^*(n=4)$ populations via their coupling with other species in the plasma. We show that the existence of two populations of radiating $H(n=4)$ atoms is plausible.

The neutral atoms in the $n=4$ excitation state are produced by MAR as explained in section 3.4.1. The H_2^+ ion resulting from the first MAR reaction (3.5) participates

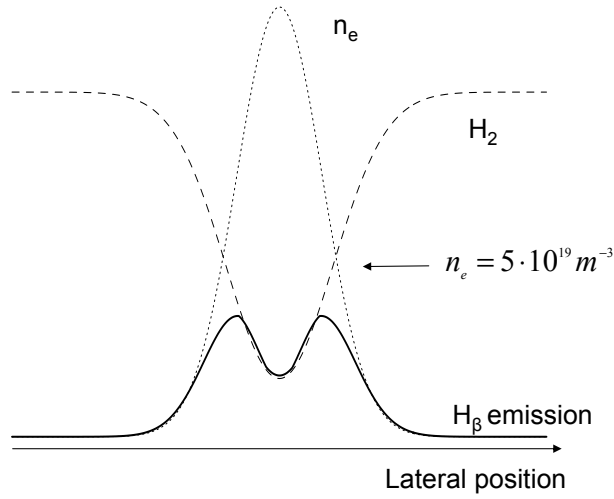


Figure 3.15: Schematic picture of expected plasma emission on the basis of radial electron density profile and molecular hydrogen profile. The molecular hydrogen density profile is hollow due to a high dissociation degree and short penetration depth due to charge exchange. The emission is proportional to both electron density and molecular hydrogen density for low electron densities, however above about $n_e > 5 \cdot 10^{19} \text{ m}^{-3}$, the emission is solely proportional to n_{H_2} . The result is that the measured emission originates mostly from a ring at a radius depending on the penetration depth of molecular hydrogen into the beam.

in an average of six ion-ion collisions before undergoing dissociative recombination. It thereby equilibrates with the ion temperature while also undergoing $\vec{E} \times \vec{B}$ -drift rotation. In the next step, equation (3.6), the H_2^+ ion dissociatively recombines to form H^* , which partly inherits the temperature and velocity of the ions. A possible subsequent electron excitation to $n = 4$ does not change this. Next, the hot radiating species couple very effectively to the atomic ions by resonant charge exchange:



The time constant for charge exchange at an ion density of $1 \cdot 10^{20} \text{ m}^{-3}$ is $4.6 \cdot 10^{-8} \text{ s}$ [26]. This is shorter than the characteristic radiation time of the Balmer- β transition: $1.2 \cdot 10^{-7} \text{ s}$. Thus, following the above consideration, we would expect the radiating $H^*(n=4)$ atoms to have a velocity and temperature resembling those of the ion population.

However, particularly towards the edges of the plasma beam, where most emission originates, the radiating species also encounters neutrals: H atoms and H_2 molecules. Collisions with H atoms are resonant and have large rates. With n_H in the same order as

$n_e = n_i$, we estimate the time constant of these collisions (reaction cross-section from [33]) to fall within the radiation time of the Balmer- β transition. Thus part of the $H^*(n=4)$ atoms will adopt a neutral, colder and almost non-rotating distribution. As neutrals in the ground state have lower collision rates with ions (their mean-free path is of the same order as the diameter of the plasma beam) they will have clearly different properties to the ions. In conclusion, the Balmer- β light will carry information both on the hot rotating ions and on the cold background gas.

These predictions are in line with results from hollow cathode arc plasmas in the literature where the ion motion can be measured. Theuws [10] experiments with argon plasma. A model predicts two neutral populations by considering on the one hand neutral-ion collisions and charge exchange reactions and on the other hand neutral-neutral collisions. The existence of these two populations is confirmed by a fit of a time-of-flight spectrum. Pots [9] also experiments in Argon and fits a spectrum measured with a Fabry-Perot interferometer. He finds two populations which he explains as those neutrals that have undergone a charge exchange or neutral-ion collision and those that have not. Timmermans [7] finds similar results for argon with a Fabry-Perot interferometer.

3.5 Rotation of the plasma jet

In this section we characterize the dependence of the jet rotation in Pilot-PSI on the magnetic field and nozzle diameter in order to explore the mechanisms behind the rotation. An understanding of these mechanisms is important since the electric fields associated with the rotation are responsible for higher power input into the plasma and this results in extra ionization and higher source efficiency.

Plasma rotation in a magnetized arc driven by an $\vec{E} \times \vec{B}$ force is well described in the literature (for example [4; 5; 6; 7; 8]). In the absence of friction, inertia and viscosity, the velocity of the $\vec{E} \times \vec{B}$ rotation drift is given by

$$\vec{v}_{rot} = \frac{\vec{E} \times \vec{B}}{B^2} \quad (3.14)$$

In the Pilot-PSI plasma, two possible sources of the radial electric field are worth considering. They are the ambipolar field and the electric field that is related to the arc current. The ambipolar field in Pilot-PSI is a few hundred Volts per meter, too small to account for the rotation velocities observed of kilometers per second.

The field causing the rotation is provided by the potential drop over the cascaded arc. In a magnetic field, the potential drop between the first plate of the cascaded arc and the anode (see Fig. 3.2) is larger than the potential drop between each of the other plates in the arc (see Fig. 3.3). The size of this extra potential drop is strongly dependent on magnetic field and the size of the anode nozzle as shown in Fig. 3.16. We can explain the phenomena shown in Fig. 3.16 by considering the magnetic confinement of the beam. The resistivity is low in the axial direction parallel to the magnetic field and high in the radial direction perpendicular to the field. The radial electron current path therefore spreads out in the axial direction until the resistance of the axial and radial current paths

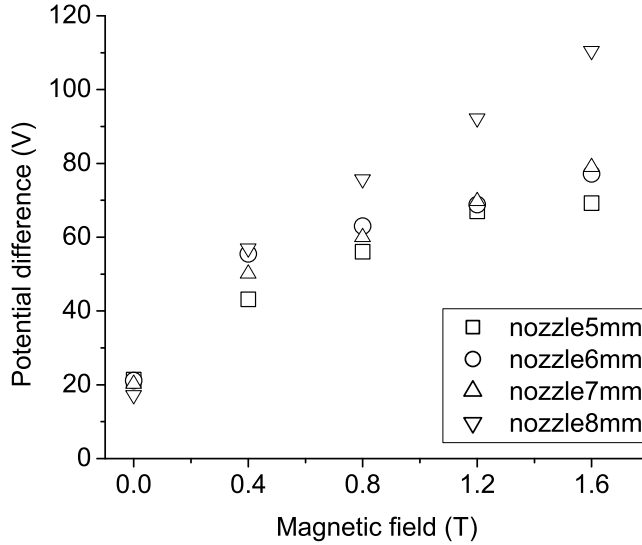


Figure 3.16: Potential difference between the anode and the first cascaded plate plotted against the magnetic field for a nozzle diameter of 5, 6, 7 and 8 mm. The voltage increases with both magnetic field and nozzle diameter.

are equal. This is shown schematically in Fig. 3.17. The resistance of this current channel causes a potential build-up between the first plate of the cascaded arc and the anode. The effect becomes stronger as the radial confinement increases with increasing magnetic field. The effect also increases with increasing nozzle opening radius, because the length travelled by the current in the vessel increases.

The radial electric field associated with the built-up potential can be estimated as the potential divided by the plasma radius. The field varies from 50 to 100 volts over the radius of a few millimeters and is much larger than the ambipolar field which corresponds to a voltage of around 1 V over the plasma radius. The $\vec{E} \times \vec{B}$ -drift resulting from this field before inclusion of damping effects towards the edge of the beam is a strong rotation. Fig. 3.18 shows such a strong rotation velocity, and its dependence on magnetic field and nozzle diameter. Plotted is the maximum velocity of the lateral profile. It increases with nozzle diameter and with magnetic field, in the same fashion as the potential build-up does in Fig. 3.16.

To establish that the field strengths needed to drive the rotation are available, we compare the radial electric fields estimated from the potential build-up in the source to those needed to drive the rotation frequency. The measured rotation frequency is shown in Fig. 3.19 as a function of lateral position. The frequency is calculated as the rotation velocity in Fig. 3.10 divided by the lateral position at which it is measured. We take the

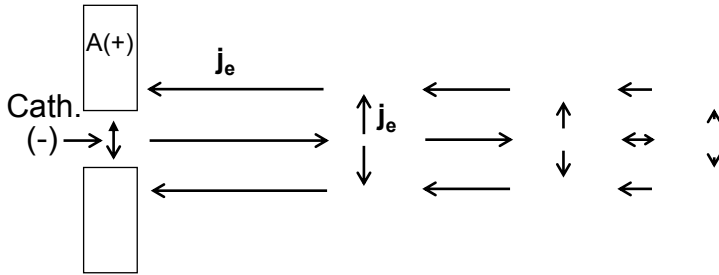


Figure 3.17: The electrons cannot close the circuit within the source due to their limited mobility across the magnetic field. The radial electron current path spreads out in the axial direction until the resistance of the axial and radial current paths are equal.

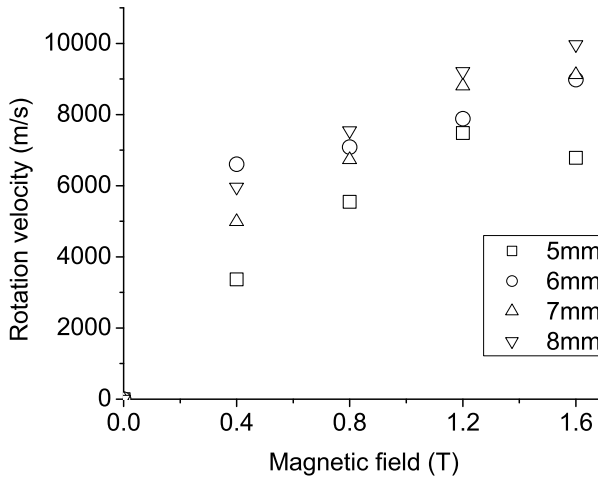


Figure 3.18: Rotation velocities of the plasma jet (the maxima of the lateral profile) derived from the Doppler shift of the Balmer- β line plotted against magnetic field. The measurements were performed for nozzle opening diameters of 5, 6, 7 and 8 mm for magnetic field settings, 0.4, 0.8, 1.2 and 1.6 T. The velocity increases approximately linearly with magnetic field.

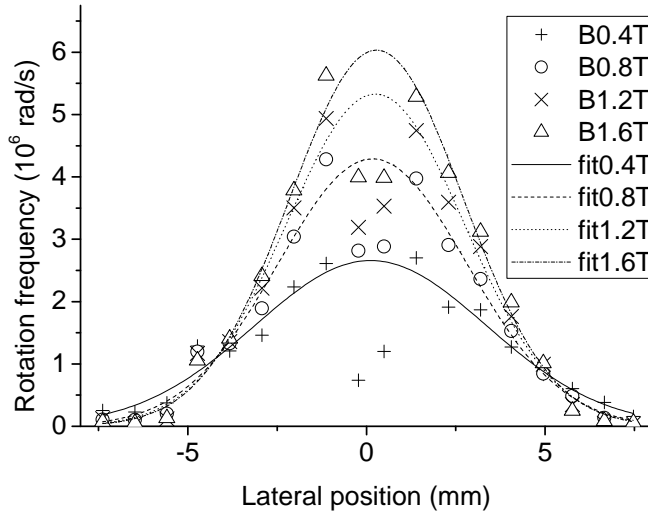


Figure 3.19: The lateral rotation frequency profiles for each of the four magnetic field settings, 0.4, 0.8, 1.2 and 1.6 T.

central value from the fit of the rotation frequency and calculate the minimum electric field required to drive it: $E = vB = r\omega B$. We use the width of the rotation frequency profile in the calculation of the available electric field strength. A comparison of the available and minimum required electric field is shown in Fig. 3.20.

We observe that the electric fields available and required for rotation lie within the same range. For higher values of the magnetic field, the field available seems to be a little less than that required. This can be understood since we compare an average electric field to the field required for the maximum rotation frequency.

3.6 Conclusion

Large rotation velocities reaching 10 km/s in the high density, magnetized plasma of Pilot-PSI have been measured. A correlation has been shown between the rotation velocity and both the magnetic field strength and the nozzle diameter of the cascaded arc plasma source. This supports the existence of an extra source of plasma heating, source current that penetrates axially into the vessel due to magnetic confinement. The potential build-up due to this current path has been shown to be strong enough to drive the rotation velocities measured by spectroscopy via an $\vec{E} \times \vec{B}$ force.

The rotation velocities observed support the methodology developed to analyze an asymmetric Balmer- β optical emission spectrum in our plasma. The method involves fitting the spectrum with a double Voigt profile. This assumes the existence of two radiating populations, whereby one is strongly coupled to the ion population. Results from

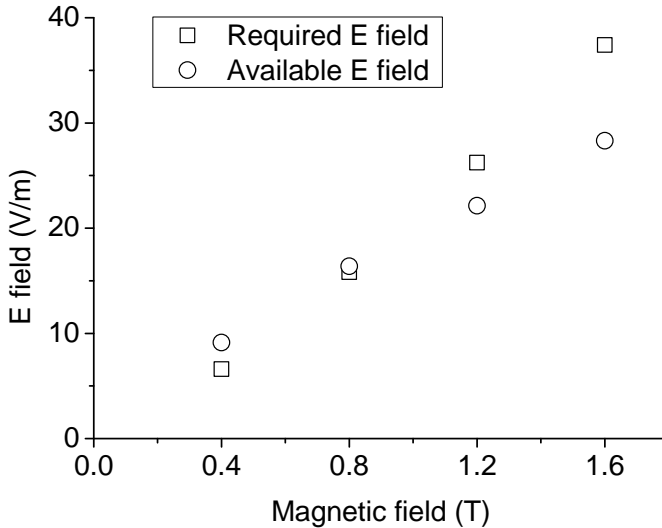


Figure 3.20: A comparison between the electric fields available and those needed to drive the maximum rotation frequency. The available electric field is calculated from the potential drop between the anode and the first cascaded plate. The radial distance of this potential drop is taken to be the width of the rotation frequency profile. The maximum rotation frequency is taken to be the highest data point in the fit of the rotation frequency. The electric field required to drive it is calculated from $E = vB = r\omega B$.

the fitting procedure agree with predictions based on a survey of the reactions involved, the emission profile and Thomson scattering measurements.

3.7 Acknowledgment

This study is part of the research programme of the ‘Stichting voor Fundamenteel Onderzoek der Materie’ (FOM), which is financially supported by the ‘Nederlandse Organisatie voor Wetenschappelijk Onderzoek’ (NWO). It is supported by the European Communities under the contract of Association between EURATOM and FOM and carried out within the framework of the European Fusion Programme.

References

- [1] G. J. van Rooij *et al.*, “Extreme hydrogen plasma densities achieved in a linear plasma generator,” *Appl. Phys. Lett.*, vol. 90, p. 121501, 2007.
- [2] A. W. Kleyn, W. Koppers, and N. J. Lopes Cardozo, “Plasma-surface interaction in ITER,” *Vacuum*, vol. 80, pp. 1098–1106, 2006.
- [3] J. Westerhout *et al.*, “PSI research in the ITER divertor parameter range at the FOM PSI-lab,” *Phys. Scripta*, vol. T128, pp. 18–22, 2007.
- [4] V. M. Lelevkin, D. K. Otorbaev, and D. C. Schram, *Physics of non-equilibrium plasmas*. North-Holland, Amsterdam, 1992.
- [5] D. C. Schram, J. J. A. M. van der Mullen, B. F. M. Pots, and C. J. Timmermans, “On the pressure balance and plasma transport in cylindrical magnetized arcs,” *Z. Naturforsch.*, vol. 38a, pp. 289–303, 1983.
- [6] H. Meyer, S. Klose, E. Pasch, and G. Fussmann, “Plasma rotation in a plasma generator,” *Phys. Rev. E.*, vol. 61, no. 4, p. 4347, 2000.
- [7] C. J. Timmermans, A. Lunk, and D. C. Schram, “The rotation of ions and neutrals in a cylindrical magnetized hollow cathode argon arc,” *Contrib. Plasm. Phys.*, vol. 21, no. 2, pp. 117–126, 1981.
- [8] F. Anderegg *et al.*, “Ion heating due to rotation and collision in magnetized plasma,” *Phys. Rev. Lett.*, vol. 57, no. 3, pp. 329–332, 1986.
- [9] B. F. M. Pots, J. J. H. Coumans, H. J. Cornelissen, D. C. Schram, and B. van der Sijde, “The velocity distribution of neutral particles in the arc of a hollow cathode discharge,” *Proc. 4th ESCAMPIG*, no. C80, p. 132, 1978.
- [10] P. G. A. Theuws, H. C. W. Beijerinck, D. C. Schram, and N. F. Verster, “Molecular-beam sampling of a hollow-cathode discharge in argon as a plasma diagnostic and a source for fast neutrals,” *J. Appl. Phys.*, vol. 48, no. 6, p. 2261, 1977.
- [11] O. Waldmann, H. Meyer, and G. Fussman, “Anomalous diffusion in a linear plasma generator,” *Contrib. Plasm. Phys.*, vol. 47, no. 10, pp. 691–702, 2007.
- [12] M. C. M. van de Sanden, J. M. de Regt, G. M. Janssen, J. J. A. M. van der Mullen, D. C. Schram, and B. van der Sijde, “A combined Thomson-Rayleigh scattering diagnostic using an intensified photodiode array,” *Rev. Sci. Instrum.*, vol. 63, pp. 3369–3377, 1992.
- [13] G. M. W. Kroesen, D. C. Schram, and J. C. M. de Haas, “Fast deposition of amorphous hydrogenated carbon films using a supersonically expanding arc plasma,” *Plasma Chem. Plasma Proc.*, vol. 10, p. 531, 1990.

- [14] H. J. van der Meiden *et al.*, “High sensitivity imaging Thomson scattering for low temperature plasma,” *Rev. Sci. Instrum.*, vol. 79, p. 013505, 2008.
- [15] T. J. Obernhuber, “Velocity-map ion-imaging of the NO fragment from the UV-photodissociation of nitrosobenzene,” *Phys. Chem. Chem. Phys.*, vol. 5, pp. 2799 – 2806, 2003.
- [16] C. Thomson and V. Helbig, “Determination of the electron density from the Stark broadening of Balmer Beta-comparison between experiment and theory,” *Spectrochim. Acta*, vol. 46B, no. 8, pp. 1215–1225, 1991.
- [17] J. M. M. J. Vogels, J. C. M. de Haas, D. C. Schram, and A. Lunk, “Experiments on the longitudinal ion momentum balance in a magnetized plasma,” *J. Appl. Phys.*, vol. 59, no. 1, pp. 71–79, 1986.
- [18] S. I. Braginskii, *Reviews of modern Physics*, ch. Transport processes in a plasma, pp. 205–311. Consultants Bureau, New York, M.A. Leontovich Vol. 1 ed., 1965.
- [19] L. Spitzer, *Physics of Fully Ionized Gases*. New York: Interscience Publishers, 1962.
- [20] V. Helbig and K.-P. Nick, “Investigation of the Stark broadening of Balmer beta,” *J. Phys. B*, vol. 14, pp. 3573–3583, 1981.
- [21] C. G. Parigger, D. H. Plemmons, and E. Oks, “Balmer series H_{β} measurements in a laser-induced hydrogen plasma,” *Appl. Optics*, vol. 42, no. 30, pp. 5992–6000, 2003.
- [22] V. Helbig, “Starkeffekt-verbreitung von balmerlinien bei mittleren elektronendichten,” *Contrib. Plasm. Phys.*, vol. 31, no. 2, pp. 183–197, 1991.
- [23] N. Ohno, N. Ezumi, S. Takamura, S. I. Krasheninnikov, and A. Yu. Pigarov, “Experimental evidence of molecular activated recombination in detached recombining plasmas,” *Phys. Rev. Lett.*, vol. 81, no. 4, 1998.
- [24] N. Ezumi, D. Nishijima, and H. Kojima, “Contribution of molecular activated recombination to hydrogen plasma detachment in the divertor plasma simulator NAGDIS-II,” *J. Nucl. Mater.*, vol. 337, pp. 266–269, 1999.
- [25] M. J. de Graaf, R. Severens, R. P. Dahiya, M. C. M. van de Sanden, and D. C. Schram, “Anomalous fast recombination in hydrogen plasma involving rovibrational excitation,” *Phys. Rev. E*, vol. 48, p. 2098, 1993.
- [26] J. K. Janev, W. D. Langer, J. K. Evans, and J. D. E. Post, *Elementary Processes in Hydrogen-Helium Plasmas*. Springer-Verlag, 1987.
- [27] P. S. Krstic, “Inelastic processes from vibrationally excited states in slow $H^+ + H_2$ and $H + H_2^+$ collisions: Excitations and charge transfer,” *Phys. Rev. A*, vol. 66, p. 042717, 2002.

-
- [28] R. P. Doerner, D. G. Whyte, and D. M. Goebel, "Sputtering yield measurements during low energy xenon plasma bombardment," *J. Appl. Physics*, vol. 93, no. 9, 2003.
- [29] M. Y. Ye *et al.*, "Blister formation on tungsten surface under low energy and high flux hydrogen plasma irradiation in NAGDIS-I," *J. Nucl. Mater.*, vol. 313-316, pp. 72–76, 2003.
- [30] W. L. Wiese, M. W. Smith, and B. M. Glennon, *Atomic transition probabilities. Vol.: Hydrogen through Neon. A critical data compilation.* National Bureau of Standards, 1966.
- [31] J. J. A. M. van der Mullen and D. C. Schram, "On the atomic state distribution function in inductively coupled plasmas-III. Rate coefficients and properties of atomic states," *Spectrochim. Acta, Part B: Atomic Spectroscopy*, vol. 45B, no. 3, pp. 233–247, 1990.
- [32] P. Vankan, D. C. Schram, and R. Engeln, "Relaxation behavior of rovibrationally excited H₂ in a rarefied expansion," *J. Chem. Phys.*, vol. 121, no. 20, pp. 9876–9884, 2004.
- [33] T. Watanabe, "Collisional excitation transfer of S-P type between identical atoms," *The Physical Review*, vol. 138, no. 6A, pp. A 1573–A 1581, 1965.

Chapter 4

Diagnosing ions and neutrals via n=2 excited hydrogen atoms in plasmas with high electron density and low electron temperature *

Abstract

Ion and neutral parameters are determined in the high electron density, magnetized, hydrogen plasma beam of an ITER divertor relevant plasma via measurements of the n=2 excited neutrals. Ion rotation velocity (up to 7 km/s) and temperature (2-3 eV $\sim T_e$) are obtained from analysis of H- α spectra measured close to the plasma source. The methodology for neutral density determination is explained whereby measurements in the linear plasma beam of Pilot-PSI are compared to modelling. Ground state atomic densities are obtained via the production rate of n=2 and the optical thickness of the Lyman- α transition (escape factor ~ 0.6) and yield an ionization degree $> 85\%$ and dissociation degree in the residual gas of $\sim 4\%$. A 30% proportion of molecules with a rovibrational excitation of more than 2 eV is deduced from the production rate of n=2 atoms. This proportion increases by more than a factor of four for a doubling of the electron density in the transition to ITER divertor relevant electron densities, probably because of a large increase in the production and confinement of ground state neutrals. Measurements are made using Laser Induced Fluorescence (LIF) and absorption, the suitability of which are evaluated as diagnostics for this plasma regime. Absorption is found to have a much better sensitivity than LIF, mainly due to competition with background emission.

*Published as: A.E. Shumack, D.C. Schram, J. Biesheuvel, W.J. Goedheer and G.J. van Rooij. *Phys. Rev. E* **83**, 036402 (2011). Small changes in this thesis: some figures have been spread over two pages, some black and white figures are now in colour. In Fig. 4.1, the position of target has been adjusted to give a more accurate depiction of the experiment. Some references have been changed to refer to Chap. 3 instead of to the corresponding article.

4.1 Introduction

The plasma conditions expected in the divertor of the experimental fusion reactor ITER, constitute a new regime in plasma physics. The high electron density ($\sim 10^{20} \text{ m}^{-3}$) ensures that the (hydrogen) plasma is not transparent for neutrals (produced by recombination at the divertor plates) and the low electron temperature ($\sim 1\text{-}5 \text{ eV}$) is such that the plasma balances on the boundary between an ionizing and recombining plasma. Especially the interaction between charged and neutral species in this plasma regime is not trivial. For the progression of plasma-wall interaction studies in fusion research [1], a good understanding of this plasma regime is imperative. Quantities that need to be measured to achieve this are density, temperature and velocity of electrons, protons, atoms and (rovibrationally excited) molecules. Electron temperature and density can be easily measured with excellent statistics in a high electron density plasma using Thomson scattering [2; 3]. Protons and ground state atoms are more difficult to access non-intrusively.

More readily accessible via active spectroscopy are n=2 excited atoms. In this paper we analyze the production and destruction processes of the n=2 excited atom population (Sect. 4.2) and show how we can use this species in an ITER divertor relevant regime to access density information on ground state atoms and rovibrationally excited molecules and temperature and velocity information on protons.

Experiments are performed in the magnetized plasma beam of Pilot-PSI (described in Sect. 4.3), a linear, magnetized hydrogen plasma generator. This machine simulates the energy flux to the divertor plates expected in ITER. It also uniquely produces plasmas of such high electron density (at temperatures of a few eV) that - as expected in the divertor of ITER - interaction between ground state atoms and ions is important and rovibrationally excited molecules have very short mean free paths (of only a few millimeters).

One major difference between the plasma of Pilot-PSI and the ITER divertor is the fact that the beam of Pilot-PSI is surrounded by gas. Rovibrationally excited molecules will penetrate the edge of the beam and play a significant role in the plasma dynamics. For high electron density conditions (ITER divertor relevant electron densities), these molecules will not reach the centre of the beam. The dynamics at a distance from the divertor plates in ITER are therefore well simulated in the centre of the beam of Pilot-PSI. Another difference between Pilot-PSI and the ITER divertor concerns the surface area of the impinging beam. To properly study the plasma at the ITER divertor plates, the beam should be wider than the mean free paths of the most important processes. This is not necessarily the case for the $\sim 1 \text{ cm}$ diameter beam of Pilot-PSI.

The results presented in this paper are measured in both the central and edge regions of the plasma beam. They are relevant for the understanding of linear divertor simulators in general, as well as (especially in the case of information about the centre of the beam) for understanding of the ITER divertor itself. This paper also forms a framework for future measurements in the upgrade of Pilot-PSI - Magnum-PSI [4] - in which the plasma beam diameter will be larger and the effect of background molecules therefore less important.

Parameters that are varied in this paper are electron density, background pressure

and lateral position. We study the density behavior of various neutral populations in the transition from the weakly magnetized, low electron density, hydrogen plasma regime [5; 6; 7; 8] up to ITER divertor relevant electron densities. The effect of background pressure is explored by varying the background pressure from low (~ 6.5 Pa, i.e. close to the 1 Pa neutral pressure expected in the ITER divertor) to high (~ 50 Pa). Lateral scans across the diameter of the beam allow study of the penetration of molecules into the beam. Measurements are made at a large distance from the target, so that in the interpretation recycling effects at the target need not be considered. An overview of the plasma conditions studied in this paper is given in Sect. 4.3.2.

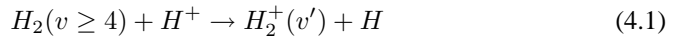
We measure the n=2 atoms using both Laser Induced Fluorescence (LIF) and absorption spectroscopy. Data analysis is outlined in Sect. 4.3.3 and results are presented in Sect. 4.4. Ground state atom densities are estimated from these measurements via a Monte Carlo simulation of the reabsorption of Lyman- α photons (Sect. 4.5). Other neutral densities are determined in Sect. 4.6 by comparison of measurements with the population balance. The suitability of the two diagnostic techniques in the given plasma regime are compared in the discussion (Sect. 4.7), together with a discussion of the results on ion parameters. Conclusions are given in Sect. 4.8.

4.2 Analysis of the population balance of n=2 excited atoms

In this section, we identify the most dominant production and destruction mechanisms for n=2 excited neutrals. This will serve as a framework for understanding the measurement data. We set up a local model in order to predict the n=2 density that can be expected at a single position depending on densities of other species at that same position.

4.2.1 Production mechanisms of n=2 excited neutrals

The dominant population processes for n=2 in our plasma are Molecular Activated Recombination (MAR) and relaxation (via electron de-excitation and radiation) from the n=3 level, which is itself dominantly populated by MAR. MAR is charge exchange (c.x.),



followed by dissociative recombination (d.r.),



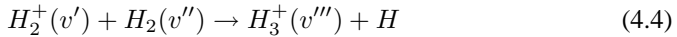
[6; 9; 10] $H_2(v \geq 4)$ is a rovibrationally excited hydrogen molecule, with an excitation energy larger than 2 eV. H^* indicates an excited hydrogen atom. The distribution of excited states from reaction 4.2 is assumed to be the same as for d.r. with $v = 0-9$ (10 % n=2, 45 % n=3, 22 % n=4, 23 % n>4)[11]). Above $n_e = 10^{19} \text{ m}^{-3}$, charge exchange is the slowest of the two reactions and thus rate determining. Above 1 eV, the rate coefficient $\langle \sigma v \rangle$ of charge exchange is $3 \cdot 10^{-15} \text{ m}^3 \text{ s}^{-1}$ [12] for molecules with a vibrational excitation $v \geq 4$. For molecules with a lower vibrational energy, the rate coefficients are about 100 times lower.

Other direct n=2 and n=3 production mechanisms are less important in our plasma. Direct electron excitation to n=2 has a total rate coefficient of $8 \cdot 10^{-16} \text{ m}^3 \text{ s}^{-1}$ at 3 eV [11] (decreasing fast at lower electron temperatures) and is slower for n=3. It may give a minor contribution to the population of the n=2 level, however we will show experimentally that it can be ignored. The net effect of three particle recombination ($\langle \sigma v \rangle < 2.9 \cdot 10^{-40} \text{ m}^6 \text{ s}^{-1}$ [13] for $T_e > 1 \text{ eV}$) corrected for by loss via direct ionization, only gives a significant contribution to n=2 and n=3 levels for electron densities higher than $7 \cdot 10^{21} \text{ m}^{-3}$. Mutual neutralization of H^- and H^+ has a high rate coefficient ($\sim 3 \cdot 10^{-15} \text{ m}^3 \text{ s}^{-1}$ for n=2 and $5 \cdot 10^{-14} \text{ m}^3 \text{ s}^{-1}$ for n=3), but at high electron density, there are a multitude of competing processes involving H^- . Dissociative recombination of H_3^+ to n=2 also has a high rate coefficient ($\sim 3 \cdot 10^{-14} \text{ m}^3 \text{ s}^{-1}$), but requires H_2^+ ions for production, the density of which is kept low by dissociative recombination and mutual neutralization. We thus conclude that MAR is the dominant direct excitation mechanism for both n=2 and n=3. We also include relaxation to n=2 from the level closest by, n=3. Estimations have shown that relaxation from other levels to n=2 and n=3 levels can be ignored.

The rate of MAR is $\alpha n_e n_{H_2^+} k_{dr}$, where n_e is the electron density [m^{-3}], k_{dr} is the rate of dissociative recombination [$\text{m}^3 \text{ s}^{-1}$] (all rate coefficients used in this paper are taken from [11] unless stated otherwise), α is the branching ratio for the relevant excited state (0.1 for n=2 and 0.45 for n=3 [11]) and $n_{H_2^+}$ [m^{-3}] is the density of H_2^+ calculated from the balance:

$$\begin{aligned} \frac{dn_{H_2^+}}{dt} &= 0 \\ &= n_{H^+} n_{H_2(v \geq 4)} k_{cx} - n_{H_2^+} (n_e k_{dr} + n_{H_2} (k_{H_3^+} + k_{cx_2})) \end{aligned} \quad (4.3)$$

where k_{cx} is the rate of charge exchange (reaction 4.1), k_{cx_2} is the rate of the charge exchange reaction between H_2^+ and H_2 and $k_{H_3^+}$ is the rate of the H_3^+ producing reaction [13]:



Finding an expression for $n_{H_2^+}$ in terms of n_e using quasineutrality, $n_e = n_{H_2^+} + n_{H^+}$, we obtain

$$n_{H_2^+} = \frac{n_e n_{H_2(v \geq 4)} k_{cx}}{n_e k_{dr} + n_{H_2(v \geq 4)} k_{cx} + n_{H_2} (k_{H_3^+} + k_{cx_2})} \quad (4.5)$$

At low electron densities (for $n_e < 10^{19} \text{ m}^{-3}$ at 6.5 Pa), $n_e k_{dr}$ can be ignored and $n_{H_2^+}$ becomes approximately proportional to n_e .

For $n_e > 10^{19} \text{ m}^{-3}$,

$$n_{H_2^+} \approx \frac{n_{H_2(v \geq 4)} k_{cx}}{k_{dr}} \quad (4.6)$$

4.2.2 Local population balance of n=2 excited atoms

Excited neutrals in the n=2 excited state are assumed to be produced and destroyed locally, since within the radiative lifetime, these atoms can travel less than 0.1 mm. Note that radiation transport *can* occur and effectively lead to transport of these neutrals. This effect is simulated in Sect. 4.5.

The main production process of the n=2 state is MAR and relaxation from the n=3 state, as described above. The main destruction processes are electron (de-)excitation and radiation. Absorption of laser radiation and stimulated emission is neglected since the transition is not in saturation.

Assuming a steady state plasma:

$$\begin{aligned} \frac{dn_2}{dt} &= 0 \\ &= 0.1n_{H_2^+}n_e k_{dr} + n_3(A_{32} + n_e k_{32}) \\ &\quad - n_2(A_{21}\Lambda_{21} + n_e K_2) \end{aligned} \quad (4.7)$$

n_j is the density of the n=j excited state, A_{ij} is an Einstein coefficient, Λ_{21} the escape factor for the Lyman- α line, k_{ij} the rate of electron (de-)excitation from level i to level j (from [14]) and $K_i = \sum_j k_{ij}$ (from [15]). This yields:

$$n_2 = \frac{0.1n_{H_2^+}n_e k_{dr} + n_3(A_{32} + n_e k_{32})}{A_{21}\Lambda_{21} + n_e K_2} \quad (4.8)$$

A balance for the density of the n=3 excited state is obtained using the same procedure:

$$n_3 = \frac{0.45n_{H_2^+}n_e k_{dr}}{A_3 + n_e K_3} \quad (4.9)$$

where $A_3 = \sum_i A_{3i}$. Solving Equations 4.8 and 4.9 with $k_{32}/K_3 \approx A_{32}/A_3 \approx 0.45$, gives approximately:

$$n_2 = \frac{0.3n_{H_2^+}n_e k_{dr}}{A_{21}\Lambda_{21} + n_e K_2} \quad (4.10)$$

We distinguish the following regimes:

a) For $n_e < 10^{19} \text{ m}^{-3}$: $n_{H_2^+} \propto n_e$ and $A_{21}\Lambda_{21} \gg n_e K_2$, therefore

$$n_2 \propto n_e^2 \quad (4.11)$$

b) For $10^{19} \text{ m}^{-3} < n_e \ll A_{21}\Lambda_{21}/K_2$: $n_{H_2^+} \approx n_{H_2(v \geq 4)} k_{cx}/k_{dr}$ and $A_{21}\Lambda_{21} \gg n_e K_2$, therefore

$$n_2 \approx \frac{0.3n_e n_{H_2(v \geq 4)} k_{cx}}{A_{21}\Lambda_{21}} \quad (4.12)$$

c) For $n_e \gg A_{21}\Lambda_{21}/K_2$: $n_{H_2^+} \approx n_{H_2(v \geq 4)}k_{cx}/k_{dr}$ and $A_{21}\Lambda_{21} \ll n_e K_2$, therefore

$$n_2 \approx \frac{0.3n_{H_2(v \geq 4)}k_{cx}}{K_2} \quad (4.13)$$

These expressions give simple n_e dependencies for n_2 in different electron density ranges. However, the dependency of the escape factor of Lyman- α , Λ_{21} on n_e is not yet considered. We consider the expected behavior of the escape factor, Λ_{21} below.

4.2.3 Influence of the escape factor in the population balance

The plasma becomes optically thick for Lyman- α (and to a lesser extent also for Lyman- β) if the ground state neutral density, n_H , in the plasma is sufficiently high. This density is expected to rise as a function of electron density in the plasma. However the dependency is difficult to predict, especially at the measurement position, 4 cm from the plasma source. Ground state atoms are long-lived and can travel several centimeters in the axial direction before escaping radially from the plasma beam. The flux of n_H in the beam at the exit of the plasma source is expected to increase with source current, since the electron density inside the source channel increases [16] and the mean free path of these neutrals decreases. Local production of n_H in the beam outside the plasma source is expected to increase linearly with electron density since the rates of its two main production mechanisms, MAR and electron dissociation of molecules[13], are both proportional to n_e .

The dependency of the ground state density near the plasma source will be estimated in this paper using the escape factor, Λ_{21} . For the low electron density regime described in Equation 4.12, the electron density dependency of the n=2 density is $H_2(v \geq 4)(n_e)n_e/\Lambda_{21}(n_e)$. Using measurements of the n=2 density vs n_e and calculations of Λ_{21} vs n_H , we will obtain combined information about n_H and $n_{H_2(v \geq 4)}$. The escape factor is taken from K. Behringer and U. Fantz [17], calculated for a cylindrical, hydrogen plasma with a parabolic emission profile and a purely Gaussian broadened spectral line. According to Rosado [18], the behavior of the escape factor for a Voigt spectral line shows almost identical behavior, down to an escape factor of less than 0.1. For an optical thickness, kr , of less than one, $\Lambda \approx 1/kr \propto 1/n_H$.

The other important role of the escape factor in the n=2 population balance is its influence on the relative importance of loss by radiation and electron de-excitation. If electron de-excitation dominates, the n=2 density as a function of the electron density will saturate (Eqn. 4.13). A lower escape factor will cause this saturation to occur at a lower value of the electron density.

4.2.4 Radial dependencies of the population balance

The radial density profile of n=2 excited neutrals depends sensitively on the radial profiles of n_e and $n_{H_2(v \geq 4)}$. According to Equations 4.11-4.13, at low electron densities the n=2 profile is dependent on the electron density and at high electron densities it depends only

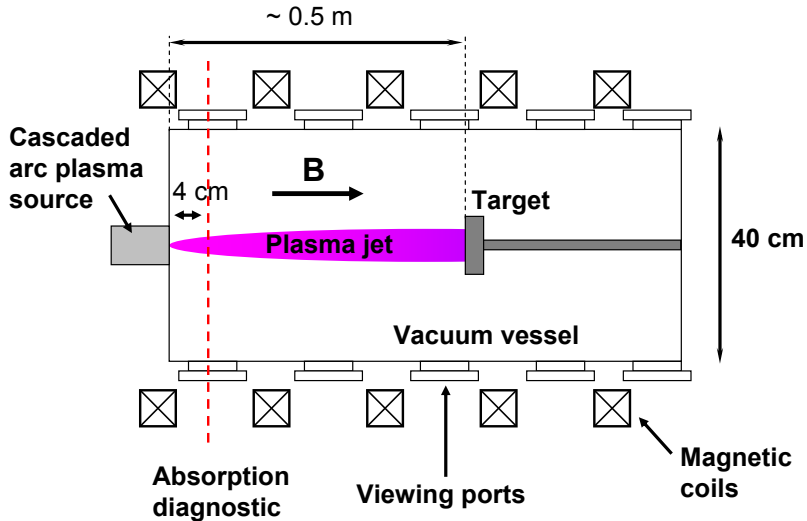


Figure 4.1: Plasma experiment Pilot-PSI.

on the $H_2(v \geq 4)$ density. The latter profile becomes hollow when the electron density is so high that the mean free path (determined by charge exchange in combination with elastic collisions) becomes significantly smaller than the plasma diameter. In that case, the resulting $n=2$ profile is also hollow.

Radiation transport of Lyman- α photons also affects the radial profile of $n=2$ excited neutrals. The radial density profile is broadened by reabsorption if the plasma is optically thick for these photons. A simple simulation of this effect has been carried out and is reported in Sect. 4.5.

4.3 Experiment

4.3.1 Experimental set-up

Pilot-PSI [19; 20] is a linear plasma generator, see Fig. 4.1. Hydrogen plasma is produced by a cascaded arc source [21; 16] and flows into a vacuum vessel (2-50 Pa). An axially directed magnetic field can be applied with a strength of up to 1.6 T. The beam is ~ 1 cm wide, 0.5 m long and impinges on a conducting target at floating potential. Absorption and Laser Induced Fluorescence (LIF) measurements are performed at 4 cm from the source. The electron density and temperature are measured at the same position with Thomson scattering [2; 3]. Statistics are excellent because of the high electron density.

The optical set-up for absorption and LIF is depicted in Fig. 4.2. Absorption is measured on the Balmer- α line from excited level $n=2$ to $n=3$. The LIF signal measured is the

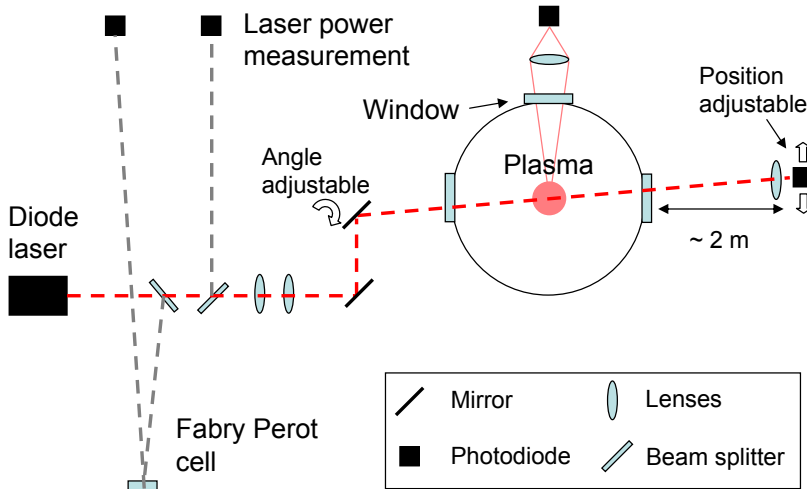


Figure 4.2: Diagnostic set-up.

spontaneous radiative decay back to the $n=2$ level. We use a tunable external cavity diode laser (Vortex 6000, New Focus, wavelength range: 656.33-656.60 nm, horizontal polarization, spectral linewidth <300 kHz). The laser power and wavelength are monitored in real time, the latter with a Fabry Perot cell. The laser is always at an angle to the windows to avoid interference effects. Scans as a function of electron density are mostly performed with expanded beam (laser spot diameter up to $\phi = 1$ cm, with the aim of maximizing the fluorescence signal for LIF). Lateral scans are performed with $\phi < 1.5$ mm.

For absorption, the laser is scanned across the radius of the plasma beam to obtain a lateral profile, by adjustment of the angle of the last mirror in front of the vessel. After a single pass through the plasma beam, the laser beam is focused onto a photodiode which measures the transmitted laser power. This photodiode is positioned at 1.5 m from the vessel to suppress background emission. The collection optics are adjusted during a radial scan, so that the laser beam is always focused onto the photodiode. The laser wavelength is scanned across the spectrum with a repetition frequency of 10 Hz with 10 averages. Directly following each measurement a calibration measurement is made with the magnetic field turned off. This reduces the laser absorption to $\ll 10^{-5}$.

Fluorescence is also collected onto a photodiode. Since the background emission is expected to be more than 1000 times stronger than the fluorescence, several techniques are employed to suppress it. Firstly lock-in detection is used with a mechanical chopper at 4 kHz, a spectrum scan at 0.05 Hz and a typical integration time of two seconds. Also, both a Balmer- α filter and a slit are mounted in front of the photodiode such that only relevant light from regions where fluorescence is expected is imaged onto the photodiode.

4.3.2 Overview of the plasma conditions

The plasma conditions studied in the LIF and absorption experiments are characterized with Thomson scattering. These conditions are varied via the magnetic field strength, the discharge current in the plasma source and the background pressure in the vessel. A low electron density range of $1 - 3 \cdot 10^{19} \text{ m}^{-3}$ is achieved at 0.015 T and a high density range of $2 - 10 \cdot 10^{20} \text{ m}^{-3}$ at 0.4 T.

Fig. 4.3 gives an overview of representative electron density and temperature profiles and the change of peak values as a function of operation parameters. Fig. 4.3(a) shows that the profiles are peaked and that the temperature profile is significantly wider than the density profile. In Fig. 4.3(b) peak electron density is plotted as a function of discharge current. Interpolations are given for the exact pressures at which laser spectroscopy was performed. Figures 4.3(c) and 4.3(d) show that the electron temperature and the plasma beam width are approximately independent of the discharge current.

4.3.3 Analysis of data

This section explains how $n=2$ densities are calculated from absorption and LIF signals. Also, the fitting procedure with which the spectra are analyzed in order to obtain ion velocity and temperature information is described.

Absorption data analysis

The $n=2$ density can be calculated from absorption on the non-saturated Balmer- α transition by [22]:

$$n_2(r) = \frac{8\pi g_2}{\lambda_0^2 g_3} \frac{\int k(\nu, r) d\nu}{A_{32}} \quad (4.14)$$

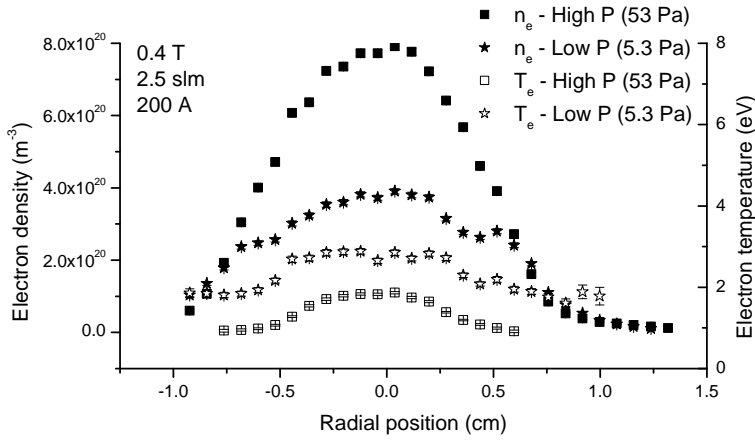
where λ_0 is the central wavelength of the absorption spectrum, g_i is the statistical weight of the i^{th} excited state, $k(\nu, r)$ is the absorption coefficient [m^{-1}] and ν is the frequency of the laser [Hz]. Note the units of $\int k(\nu) d\nu$: [$\text{m}^{-1} \text{ s}^{-1}$].

The absorption measurements are line of sight integrals and measure the average of the quantity $k(\nu, r)l$ across the beam, where l is the path length of the laser through the plasma. By spectrally integrating this data we obtain results in the unit s^{-1} with which average $n=2$ densities are calculated with an assumed beam width.

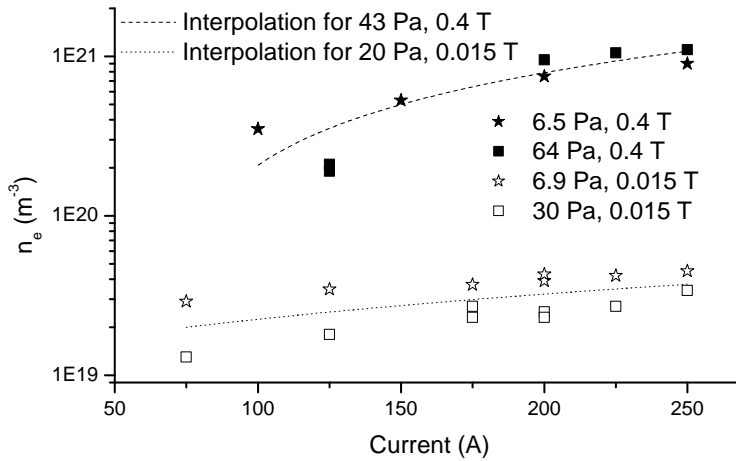
Where lateral scans are performed, Abel inversion is used (as well as spectral integration) to obtain the quantity $\int k(\nu, r) d\nu$ (and subsequently the $n=2$ density) at local position r .

LIF data analysis

When fluorescence on the (non-saturated) Balmer- α transition is induced by absorption on the same transition, the $n=2$ density can be calculated from the measured LIF signal as follows. The amount of fluorescence photons emitted per cubic meter per second by



(a)



(b)

Figure 4.3: Overview of plasma conditions studied in this paper. (a) Typical electron density and temperature profiles, corresponding to the lateral n=2 density measurements made at 0.4 T (b) Plasma conditions for electron density scans studied in this paper, characterized by peak electron density. Interpolations are for the background pressures in laser spectroscopy experiments. (c) Corresponding peak electron temperature and (d) Full width half maximum (FWHM) of electron density profiles. Neither vary significantly as a function of current.

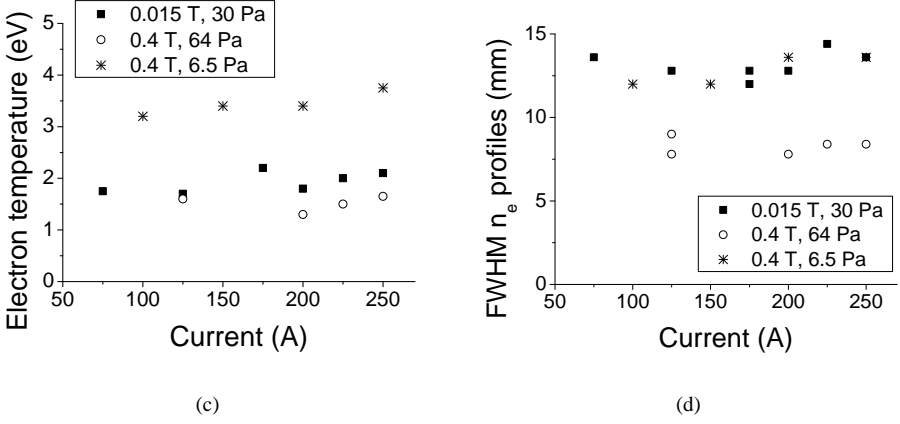


Figure 4.3: Continued.

the plasma is:

$$Y_{LIF}[\text{photons m}^{-3}\text{s}^{-1}] = A_{32}n_3^{LIF} \quad (4.15)$$

where n_3^{LIF} is the density of $n=3$ excited neutrals that are created by absorption of laser photons. Its value is determined from a steady state balance between its destruction and production processes:

$$n_3^{LIF}(A_3 + n_e K_3 + B_{32}\rho) = n_2 B_{23}\rho \quad (4.16)$$

ρ the laser power density [Jsm^{-3}] and B_{ik} is an Einstein coefficient. The signal is measured in W/nm, with a resolution in the order of 10 pm (from Stark broadening). Integrating the signal over the spectrum gives us the total measurement signal S_{LIF} in Watts. This is equal to:

$$S_{LIF} = Y_{LIF} \frac{\Omega}{4\pi} T V_{det} \frac{hc}{\lambda} \quad (4.17)$$

Ω is the volume angle of the detection system ($3 \cdot 10^{-2}$ sr), T is the transmission of the optics (estimated at 0.8) and V_{det} is the detection volume. Using expressions 4.15, 4.16 and 4.17, we can calculate the density of $n=2$ atoms from:

$$n_2 = \frac{S_{LIF}(A_3 + n_e K_3 + B_{32}\rho)}{\Omega/4\pi \cdot T \cdot V_{det} \cdot hc/\lambda \cdot A_{32}B_{23}\rho} \quad (4.18)$$

Spectral analysis

Spectra are analyzed with a Voigt function [23] since Doppler and Stark broadening have comparable importance in the plasma considered. Asymmetric spectra are analyzed with a double Voigt function (detailed in Chap.3). The asymmetry is attributed to the existence

of two distributions of n=2 excited neutrals, one coupled to the ions (hotter and rotating) and one not coupled to the ions (colder and not rotating). Ion properties can therefore be determined from (the ‘hot’ component of) asymmetric spectra; temperature from the Doppler width and velocity from the Doppler shift. The fine structure of H- α is simulated by splitting each Voigt function into two Voigt peaks shifted with respect to one another by 13 pm. One is 1.5 times higher than the other.

4.4 LIF and absorption Measurements

4.4.1 Measurement data

Absorption spectra are measured for two regimes: low electron density, at a magnetic field strength of 0.015 T and high electron density at 0.4 T. LIF could only be detected in the low electron density regime. In the high electron density regime, absorption measurements are made at high and low background pressure.

First we present the spectra measured in scans of the discharge current at different background pressures and magnetic field strengths, see Fig. 4.4. They are made for the following three combinations of magnetic field strength and background pressure: 0.015 T, 20 Pa; 0.4 T, 64 Pa and 0.4 T, 6.5 Pa. All spectra are measured at the centre of the beam except in Fig. 4.4(d), where the position was optimized for maximum signal. Absorption down to $7 \cdot 10^{-4}$ is measured (at high pressure and S/N of 50), limited not by the diagnostic, but by the lower discharge current limit of the plasma source. At low pressure the minimum S/N is 15. The LIF measurements have a much lower signal noise ratio and require lock-in detection (signal detectable down to 10^{-4}). Notable is that the spectra measured off-centre (Fig. 4.4(d)) are asymmetric (see Sect. 4.3.3 for explanation).

Fig. 4.5(a) displays the tests for saturation. The absorption and LIF signal are plotted as a function of laser power from zero to full power. The transition is clearly not saturated. Fluctuations in the signal are attributed to instability of the plasma. The tests are done at conditions of minimal quenching (where saturation is most probable). Low collisional de-excitation is ensured by low electron density at low magnetic field strength. Minimal escape of Lyman radiation is chosen via high ground state neutral density, achieved at high background pressure and high discharge current (see Sect. 4.6.2).

Next we present lateral scans performed at 0.4 T at both high and low background pressures. Figure 4.6 shows lateral absorption profiles at magnetic field strength 0.4 T and background pressures 6.5 Pa and 50 Pa. The scans are made with a laser spot of diameter < 1.5 mm. The profiles are fit with three Gauss functions, allowing Abel inversion since Gauss functions are invariant under this procedure [24]. Density profiles for n=2 neutrals calculated from the results of this Abel inversion are shown in Fig. 4.7. Electron density profiles measured with Thomson scattering are also included for comparison.

The n=2 density profiles comprise of three clear components: production inside the electron density profile, production outside the electron density profile by reabsorption of Lyman- α and a hollow region in the centre of the beam (no production at all). For both measurements, the n=2 profiles become strikingly hollow for an electron density above

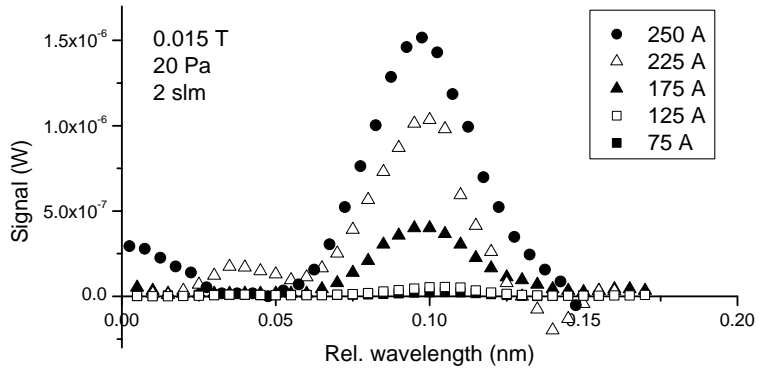
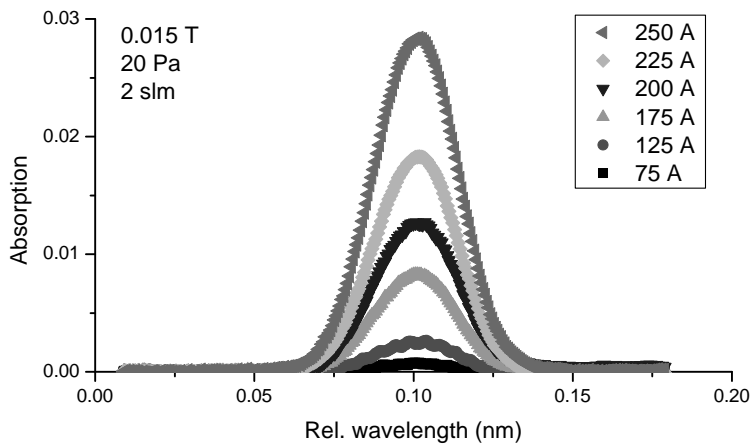
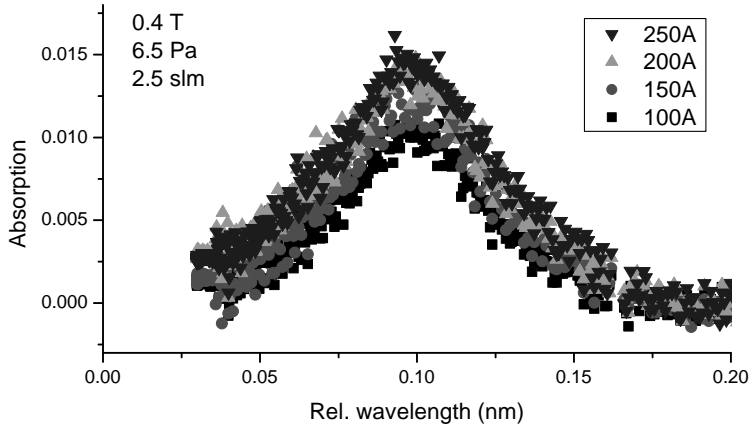
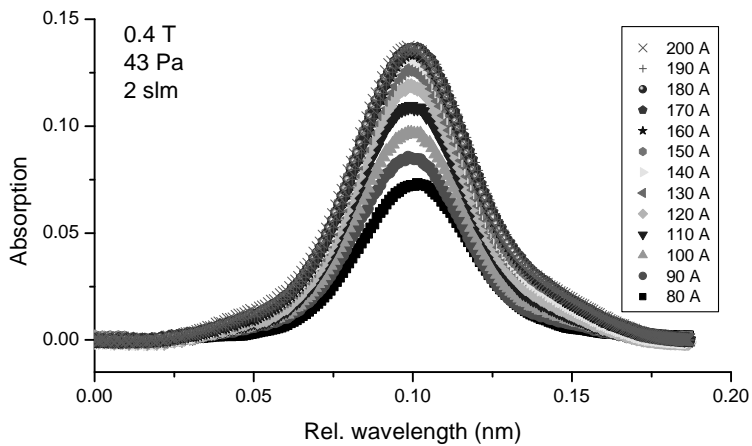
(a) LIF, low n_e , centre of beam, $\phi_{laser} \approx 3$ mm(b) Absorption, low n_e , centre of beam, $\phi_{laser} \approx 3$ mm

Figure 4.4: Absorption and LIF spectra for varying source currents for three different plasma conditions.



(c) Absorption, high n_e , low P, centre of beam, $\phi_{laser} < 1.5$ mm



(d) Absorption, high n_e , high P, off-centre, $\phi_{laser} \approx 1$ cm

Figure 4.4: Continued.

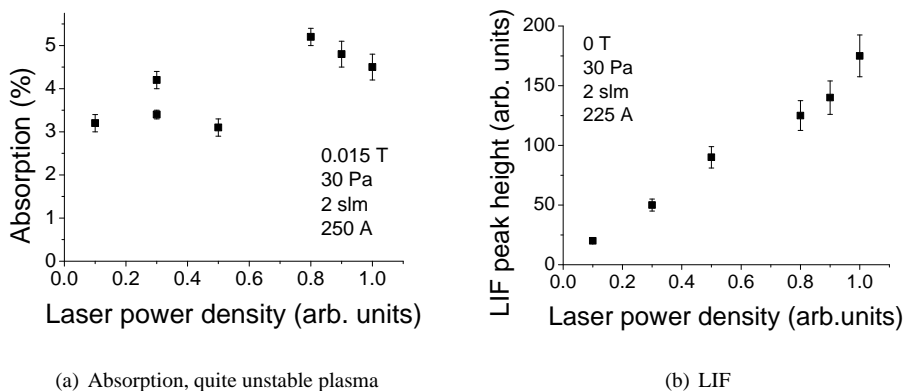
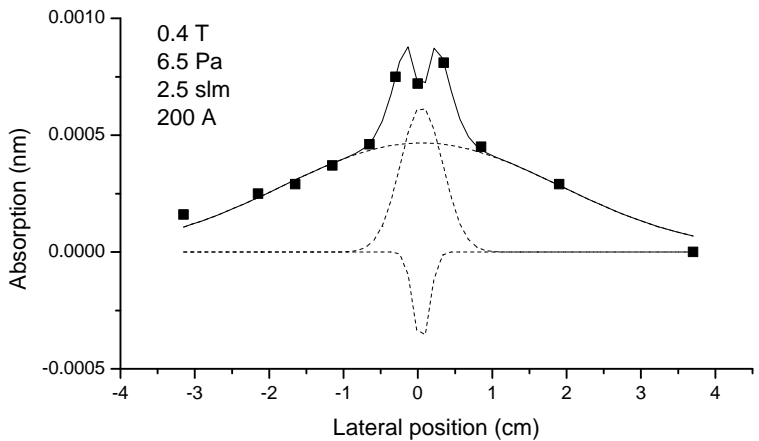


Figure 4.5: Absorption and LIF vs laser power density saturation test.

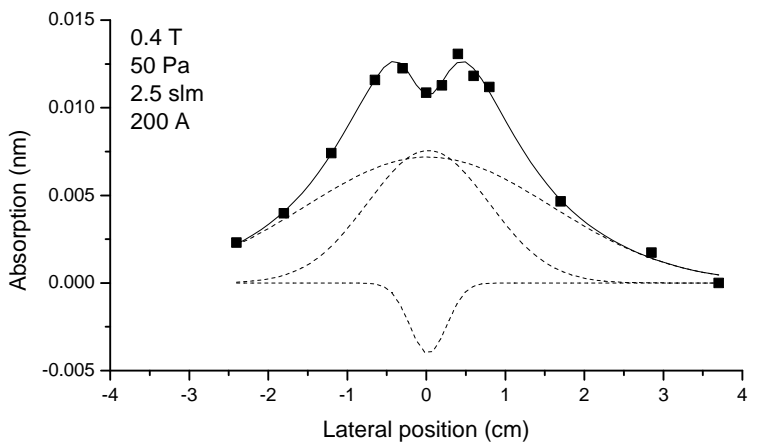
$n_e \approx 4 - 5 \cdot 10^{20} \text{ m}^{-3}$. For the 6.5 Pa measurement, the Abel inversion returns a negative density in the centre of the beam which probably indicates that the real profile is steeper than can be simulated with a Gauss function. To estimate the error made, we integrated the (positive parts of) the profile and compared it to the integrated density measured at the centre of the beam. This gives a discrepancy of 1 %. The largest difference between the lateral scans at high and low pressure is the profile shape of the reabsorption production outside the plasma beam. These profiles will be simulated and discussed further in Sect. 4.5.

Thirdly, we present $n=2$ densities calculated from the LIF and absorption spectra in Fig. 4.4 as a function of (central) electron density, see Fig. 4.8. As stated earlier, LIF could only be observed for the lowest electron density condition: $B = 0.015 \text{ T}$ and $P = 20 \text{ Pa}$. Where the background pressures are different for $n=2$ density and Thomson scattering measurements, interpolation is performed to obtain the electron density as shown in Fig. 4.3(b).

The densities from absorption spectra are averages over the diameter of the beam, whereas the densities from LIF spectra are averages over the central 3 mm of the beam (the laser spot diameter). In the calculation of the $n=2$ density from LIF, a detection volume $V_{det} = 3.4 \text{ cm}^3$ was chosen to obtain agreement with the absolute density determined from absorption. For the calculation of averages for absorption, the width of the $n=2$ density profile is assumed to be equal to the width of the electron density profile, see Fig. 4.3(d). For the high pressure case (0.4 T, 43 Pa) we make an exception. Here the $n=2$ profile is expected to be significantly wider than the electron density profile as evident from Fig. 4.7. We assume a width of 2 cm. For the low magnetic field case (0.015 T, 20 Pa), the beam width probably increases with current, as the reabsorption of Lyman- α due to increased ground state density (see Sect. 4.6.2) increases. The maximum $n=2$ density (at 0.015 T, 250 A) is therefore likely to be up to a factor of two lower than

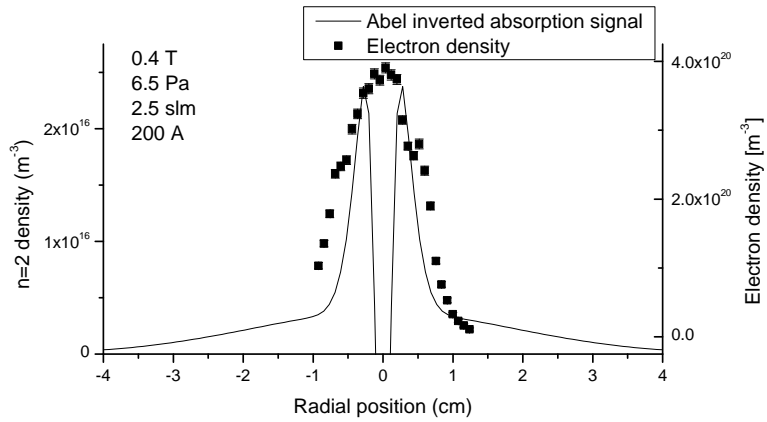


(a) 0.4 T, low P, $\phi_{laser} < 1.5$ mm

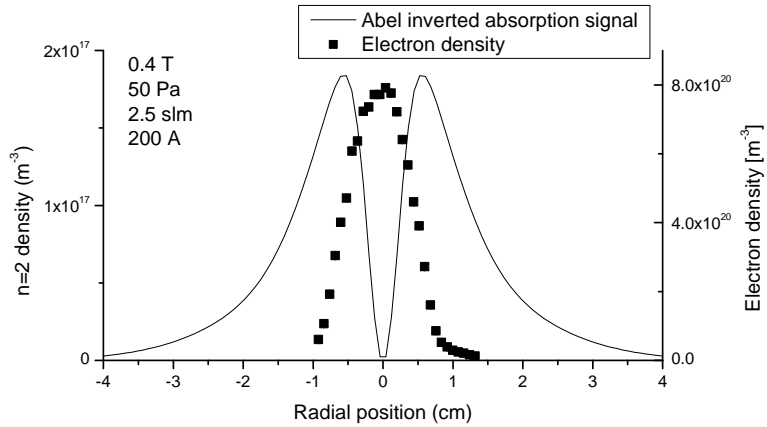


(b) 0.4 T, high P, $\phi_{laser} < 1.5$ mm

Figure 4.6: Absorption in nanometers measured as a function of lateral distance at different background pressures, fitted with three Gauss functions.



(a) 0.4 T, low P



(b) 0.4 T, high P

Figure 4.7: $n=2$ density as a function of radius determined from Abel inversion of lateral absorption scans. Electron density profiles are plotted for comparison.

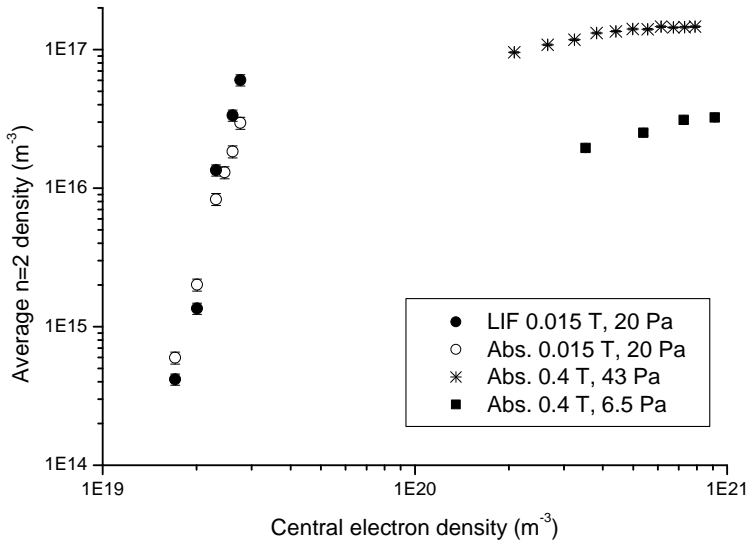


Figure 4.8: Average n=2 densities from LIF and absorption as a function of the central electron density. Where necessary, electron densities are calculated by interpolation in Fig. 4.3(b).

plotted.

4.4.2 Spectral analysis

Absorption spectra measured at high magnetic field strength (0.4 T) are found to be asymmetric (similar to the asymmetry found in H- β emission spectra in Chap. 3). This asymmetry is attributed to the existence of two populations of the excited neutrals being probed. In Chap. 3, the hotter population was attributed to charge exchange of excited neutrals with plasma ions and the colder population to collisions of excited neutrals with colder background neutrals.

Given the importance of reabsorption of Lyman- α observed in Fig. 4.7, we now propose an additional mechanism for the existence of two n=2 density distributions. The hot, rotating distribution is created by MAR, the last step of which, dissociative recombination, involves hot H₂⁺ ions and electrons. The H₂⁺ ions are coupled to the H⁺ ions since they undergo typically six collisions with these ions before dissociative recombination. The cold, non-rotating population is created by reabsorption. Lyman- α photons are reabsorbed by cold, non-rotating ground state atoms. These atoms do not live long enough to undergo charge exchange before they radiate again.

Assuming that this is the correct explanation for the double $n=2$ density distribution, we can measure the proportion of $n=2$ excited neutrals in the beam that are created by dissociative recombination and reabsorption respectively. We simply fit the spectra with a double Voigt function and compare the areas under the Voigt functions corresponding to the ‘hot’ and the ‘cold’ neutral populations. This ratio is $\sim 2/1$ for $P = 6.5$ Pa and 0.4 T and $\sim 2/3$ at the same conditions but a higher pressure of 50 Pa.

Ion temperature and velocity determinations are not affected by this additional explanation of the double distribution. These parameters are determined for the asymmetric spectra measured at high magnetic field (0.4 T), and plotted as a function of lateral position in Figs. 4.9 and 4.10, for high and low pressure respectively. The symmetric spectra outside of the plasma beam are fit with a Gauss function (accounting for fine splitting as explained in Sect. 4.3.3). The maximum rotation velocity is $5-7$ km/s in both cases. At lower pressure, the errors become larger. This is due to the lower density of $n=2$ and could be solved by improving the sensitivity of the diagnostic (see Sect. 4.7). The ‘hot’ and ‘cold’ neutral temperatures are plotted and compared to the electron temperature. The results for the temperatures of the $n=2$ distributions are reasonably systematic. One notable exception is the central point at high pressure. Here, the Stark width seems to have been overestimated and the Doppler width underestimated in the fitting procedure. The temperature of the ‘hot’ component is in reasonable agreement with the electron temperature. We should however remember that the spectra are line of sight measurements. Determined temperatures are averages over a chord of the plasma beam and are thus expected to be underestimates of the local, central ion temperature. As in Chap. 3, ion viscous heating is suggested as a cause for a hotter ion than electron temperature.

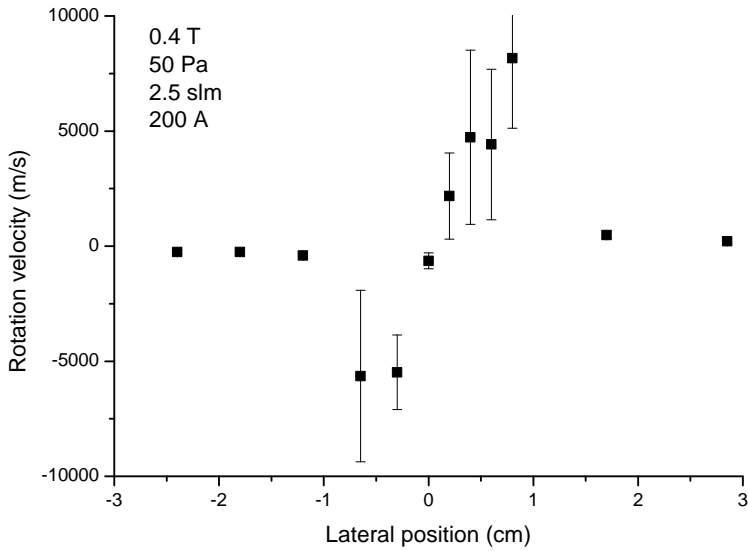
At low magnetic field strength (0.015 T), the spectra are symmetric and are fit with a single Voigt function; ion properties cannot be determined. Here, the temperature of the $n=2$ population is typically 0.3 eV, while the electron temperature is about 2 eV. The average of the whole $n=2$ population is poorly coupled to the ions.

4.5 Monte Carlo simulation of the radiation transport

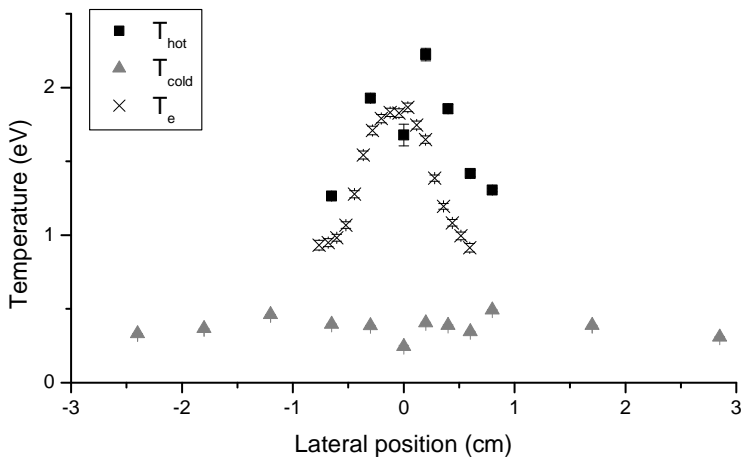
By simulating the $n=2$ production by reabsorption of Lyman- α photons and comparing this to the measurement profiles (Fig. 4.7), we are able to estimate the density of ground state neutrals just outside the plasma beam. These $n=2$ atoms could not be produced in any other way. MAR only takes place in the presence of electrons (in the plasma beam) and $n=2$ neutrals can only travel 0.1 mm or less within their life-time.

4.5.1 Method

Radiation transport in the plasma beam of Pilot-PSI was simulated in a Monte Carlo code by following a Lyman- α photon emitted in the plasma beam as it is continually emitted and reabsorbed until it hits the vessel wall at a radius of 20 cm. The simulation assumes a ‘hot’ population of $n=2$ excited atoms produced by MAR and a ‘cold’ population produced by reabsorption of Lyman- α photons as described in Sect. 4.4.2. At the start of

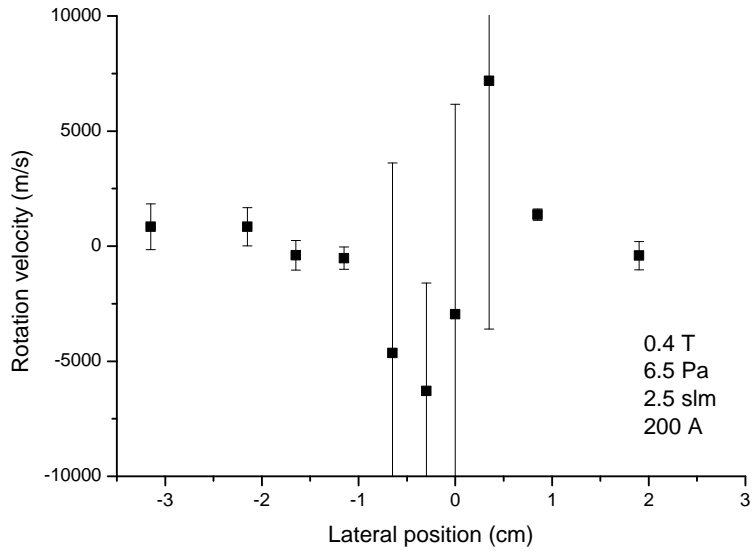


(a) Rotation velocity

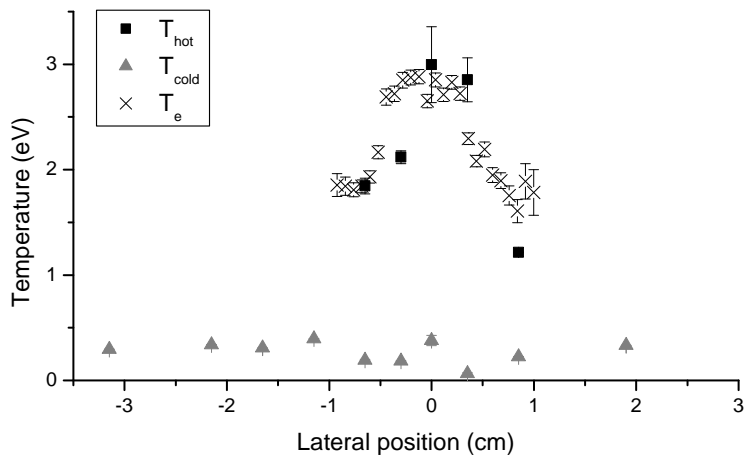


(b) Temperatures from DV fit compared to electron temperature

Figure 4.9: Rotation velocities and temperatures deduced from double Voigt fits of spectra measured in a lateral absorption scan of the plasma beam at 50 Pa and 0.4 T.



(a) Rotation velocity



(b) Temperatures from DV fit compared to electron temperature

Figure 4.10: Rotation velocities and temperatures deduced from double Voigt fits of spectra measured in a lateral absorption scan of the plasma beam at 50 Pa and 0.4 T.

the simulation, the photon is given a random frequency, with probabilities corresponding to a Doppler profile consistent with the measured temperature of the ('hot' population of) n=2 excited particles. After each subsequent reabsorption, a new random frequency is chosen for the photon from the expected Doppler spectral profile of colder ground state atoms. The number of reabsorptions is recorded in each volume $V = 2\pi r dr dz$. This calculation is repeated 10000 times and the result is averaged.

The rate of reabsorption in a certain volume V , is equal to the amount of reabsorptions, N_a , in that volume due to one photon, multiplied by the number of 'primary' photons produced per second in the plasma in slice dz . The rate of production of 'primary' photons is the number of 'primary' ('hot') n=2 atoms in the plasma beam in dz multiplied by the Einstein coefficient, A_{21} . We estimate the number of 'hot' n=2 excited neutrals as the density, n_2^{hot} , multiplied by the approximate volume in which they are created, V .

The plasma is at steady state, so we can set the rate of reabsorption of Lyman- α equal to the rate of destruction of 'secondary' n=2 neutrals:

$$N_a(r)n_2^{hot}V\alpha A_{21} = n_2(r)(A_{21} + n_e K_2) \quad (4.19)$$

So,

$$n_2(r) = \frac{A_{21}}{A_{21} + n_e K_2} N_a(r)n_2^{hot}V\alpha \quad (4.20)$$

The radiation transport calculation was carried out for ground state atoms n_H with a range of densities and temperatures. It was found that the n=2 density profile resulting from reabsorption was much less sensitive to the temperature of n_H than to its density. For the results presented in this paper, the temperature of ground state atoms was assumed to be 1000 K.

Our aim was to simulate as closely as possible the shape of the lateral absorption profiles shown in Fig. 4.7 measured at 6.5 Pa and 50 Pa in order to make an estimation of the density of n_H inside and outside of the beam. The tactic used was to assume a flat radial profile of n_H and to try different values of n_H such that the measured n=2 density was matched as closely as possible. The measured number of 'hot' n=2 excited atoms *in* the plasma was estimated by approximating the average n=2 density to be 2/3 of the peak value and taking the volume to be the region in which the electron density is between 1.5 and $3.5 \cdot 10^{20} \text{ m}^{-3}$ (above this electron density range the peak becomes hollow and below this range the production is negligible). This resulting number was multiplied by the fraction of neutrals that are 'hot' as deduced from the double Voigt fits, see Sect. 4.4.2. This ratio was 2/3 for the 6.5 Pa measurement and 2/5 for the 50 Pa measurement. The values used in the simulation are $n_2^{hot} = 4.8 \cdot 10^{16} \text{ m}^{-3}$, $V = 5.89 \cdot 10^{-5} \text{ m}^{-3}$, $T_{hot} = 2.0 \text{ eV}$, $T_{cold} = 1000 \text{ K}$ for $P = 6.5 \text{ Pa}$ and $n_2^{hot} = 1.044 \cdot 10^{16} \text{ m}^{-3}$, $V = 1.34 \cdot 10^{-4} \text{ m}^3$, $T_{hot} = 2.5 \text{ eV}$, $T_{cold} = 1000 \text{ K}$ for $P = 50 \text{ Pa}$.

4.5.2 Results

We simulated the n=2 lateral density scan measurements (Fig. 4.7) made at 6.5 Pa and 50 Pa. The results are shown in Fig. 4.11. The measured value of the density of n=2 neu-

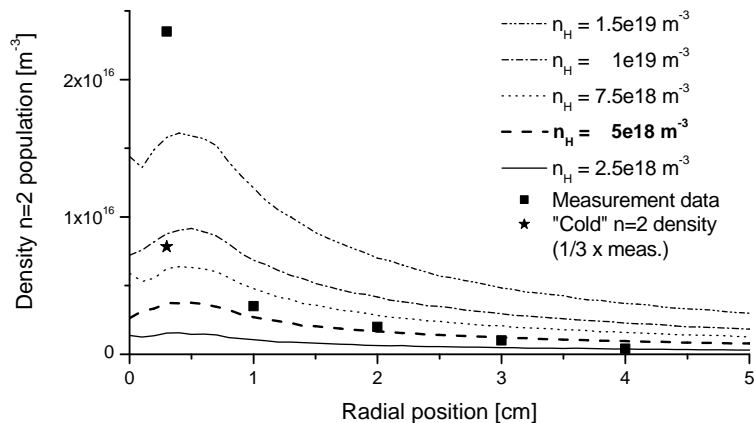
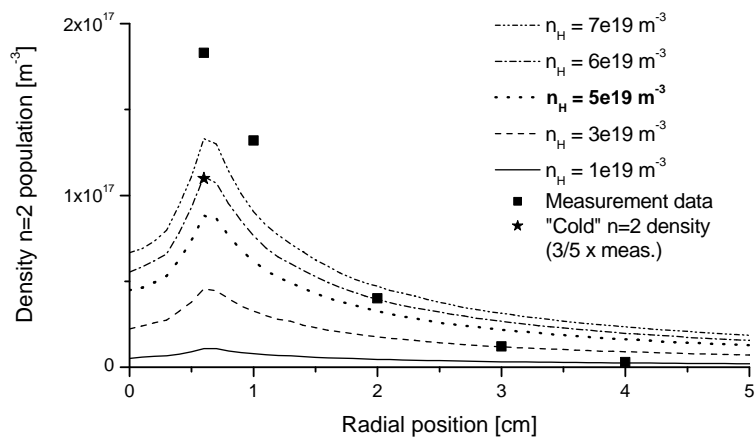
(a) $P = 6.5$ Pa(b) $P = 50$ Pa

Figure 4.11: Simulation of $n=2$ production due to radiation transport with different values of ground state density, n_H . Measurement data points are added for comparison.

trals is plotted at five positions across the radius. This is the total n=2 density, including both the hot and the cold population. The expected density of the cold population inside the beam (based on measurements of the ratio between the hot and cold population) is indicated by a star. Outside the beam, all measured n=2 atoms are expected to be cold. The calculated radial n=2 density distribution is plotted at different assumed values of the ground state density, n_H . As explained above, the radial profile of n_H is assumed to be flat. Evident is that the measurements show a faster drop in density than the simulation. This probably indicates a radial gradient in n_H , but could also be partly due to the inaccuracy of the Abel inverted profile. A radial gradient is however to be expected in n_H , since hydrogen atoms, even in the ground state, are confined by charge exchange reactions with ions when the ion density is higher than about 10^{20} m^{-3} . Outside the beam, the ground state neutral density is expected to decrease radially due to diffusion. The best overall match between measured and simulated ‘cold’ n=2 atoms is found at approximately $n_H = 5 \cdot 10^{18} \text{ m}^{-3}$ for 6.5 Pa and $n_H = 5 \cdot 10^{19} \text{ m}^{-3}$ for 50 Pa.

These solutions give an underestimation of the n=2 density in the centre of the beam and an overestimation at the edge. We conclude that the value of the neutral density in the centre is higher than determined here. This would lead to more build up of the n=2 density in the centre of the beam, and give a steeper radial n=2 density profile than simulated (more reabsorptions and thus more photon loss). This would give a better match of the n=2 density at the edge for the estimations of the ground state density made above. A gradient would be required in the assumed n_H density in the simulation to achieve more accurate results. This was not performed here due to insufficient accuracy of the Abel inversions.

4.6 Interpretation of the results

4.6.1 Estimation of the escape factor from spectral analysis

The escape factor of Lyman- α is important to know for collisional-radiative modelling of the plasma of Pilot-PSI. If this line is optically thick then both the excitation and ionization balance will lean toward higher excitation/ionization than in the optically thin case.

An estimate can be made of the Lyman- α escape factor Λ_{21} by assuming as hypothesized in Sect. 4.4.2 that there is both a ‘hot’ and a ‘cold’ distribution of n=2 atoms in the plasma populated respectively by MAR and reabsorption of Lyman- α photons. We illustrate as follows.

Considering a case in which Lyman- α is optically thin and all n=2 neutrals are produced by MAR and are ‘hot’, the population balance for the n=2 density, n_2^{thin} can be written as:

$$n_2^{thin} = n_2^{hot} = \frac{0.3n_e n_{H_2(v \geq 4)} k_{cx}}{A_{21} + n_e K_2} \quad (4.21)$$

By then considering a plasma in which Lyman- α is optically thick, we obtain:

$$n_2^{total} = \frac{0.3n_e n_{H_2(v \geq 4)} k_{cx}}{A_{21}\Lambda_{21} + n_e K_2} \quad (4.22)$$

$$= n_2^{hot} \cdot \frac{A_{21} + n_e K_2}{A_{21}\Lambda_{21} + n_e K_2} \quad (4.23)$$

$$= \frac{n_2^{hot}}{\alpha} \quad (4.24)$$

where

$$\alpha = \frac{n_2^{hot}}{n_2^{total}} \quad (4.25)$$

$$= \frac{A_{21}\Lambda_{21} + n_e K_2}{A_{21} + n_e K_2} \quad (4.26)$$

If we know α , the ratio of n=2 neutrals that are ‘hot’, we can then calculate the escape factor Λ_{21} from:

$$\Lambda_{21} = \frac{\alpha(n_e K_2 + A_{21}) - n_e K_2}{A_{21}} \quad (4.27)$$

Using an average lateral value for the electron density of $2 \cdot 10^{20} \text{ m}^{-3}$ at 6.5 Pa and $4 \cdot 10^{20} \text{ m}^{-3}$ at 50 Pa, and taking the ‘hot’ to ‘cold’ ratios as 2/3 and 2/5 respectively, we calculate that $\Lambda_{21} = 0.57$ at 6.5 Pa and $\Lambda_{21} = 0.145$ at 50 Pa. Using the escape factor simulation in [17], this gives neutral densities of $2.22 \cdot 10^{19} \text{ m}^{-3}$ and $1.11 \cdot 10^{20} \text{ m}^{-3}$ respectively. Taking the electron density in the centre of the beam, this corresponds to ionization degrees of 95 % and 88 % respectively.

In both cases the Lyman- α radiation field will have a significant effect on the excitation balance in the plasma, more so at high pressure than at low pressure.

4.6.2 Examination of the n=2 density behavior for determination of neutral densities

In Sect. 4.2, we ascertained that electrons, rovibrationally excited molecules and ground state neutrals all play an important role in the excitation balance of n=2 excited neutrals. In order to deduce density information about the neutral populations mentioned above, inside and outside of the plasma beam and at different electron densities, we now analyze the n=2 measurements made as a function of electron density (Fig. 4.8) and as a function of lateral distance (Fig. 4.7). A summary of the different neutral population densities determined is given in Sect. 4.6.3.

Density of ground state atoms and rovibrationally excited molecules in the transition to the high electron density regime

In this section we attempt to understand how n_H and $n_{H_2(v \geq 4)}$ change in Pilot-PSI in the transition to the high electron densities. We look at the n=2 density measurements as a function of electron density at low magnetic field strength (0.015 T) in Fig. 4.8. The rise in n=2 density is much steeper than the linear increase predicted by equation 4.12. An explanation could be that either the $H_2(v \geq 4)$ density or Λ_{21} or (most probably) both exhibits an n_e dependence. We consider other possible contributions to the rise to be unimportant. The electron temperature remains approximately constant, ruling out a change in the production rate of n=2 excited atoms. A change in the width of the beam due to reabsorption would at very most explain a factor of two in the n=2 density rise.

To explain the data, the factor $n_{H_2(v \geq 4)}/\Lambda_{21}$ must rise by a factor of 30 from the lowest to the highest current value. We can estimate the contribution of $n_{H_2(v \geq 4)}$ to this rise by noting the restriction on Λ_{21} . We estimated its value to be 0.145 at conditions conducive to high optical thickness (high magnetic field and high background pressure), so $0.145 < \Lambda_{21} < 1$. This gives $H_2(v \geq 4) < 2 \cdot 10^{19} \text{ m}^{-3}$ at the lowest source current and $n_{H_2(v \geq 4)} > 8 \cdot 10^{19} \text{ m}^{-3}$ at the highest source current. The minimum rise in the percentage of molecules that have an internal energy of 2 eV is from 4.3 % to 19.4 %. This is a large rise, especially if we compare it to 0.14 % from other measurements [25] in a similar machine at 0 T and low electron density ($< 10^{20} \text{ m}^{-3}$). A rise in Λ_{21} from 0.145 to 1 corresponds to a rise in the ground state atomic density from $n_H < 2.2 \cdot 10^{18} \text{ m}^{-3}$ to $n_H = 1.1 \cdot 10^{20} \text{ m}^{-3}$, which is much faster than the rise in electron density.

A faster rise in the ground state atomic density than in the electron density is plausible, since n_H is not simply a direct function of the electron density. Ground state atoms are not only produced locally, but can travel several centimeters along the axis before they exit the beam. Furthermore, the flux of neutrals exiting the beam is expected to increase with source current, since as the electron density inside the source increases with current [16], the atoms will be more and more confined by charge exchange reactions. The density of rovibrationally excited molecules can be expected to increase with atomic density as its rate of production at the wall [25] will increase.

Examination of lateral absorption profiles - determination of the ionization degree and the $H_2(v \geq 4)$ density

It is interesting to note that in Fig. 4.7 the lateral n=2 density profiles both become hollow at an electron density of $4.5 \cdot 10^{20} \text{ m}^{-3}$. This agrees well with the values of electron density at which saturation is observed in the n=2 density in Fig. 4.8, and can be explained by the radial profile of rovibrationally excited molecules which becomes hollow at high electron density. The mean free path of these molecules is equal to the radius of the beam ($\sim 6 \text{ mm}$) for $n_e = 4 \cdot 10^{20} \text{ m}^{-3}$ (molecular temperature: $\sim 0.3 \text{ eV}$, MAR rate coefficient: $3 \cdot 10^{-15} \text{ m}^3 \text{ s}^{-1}$ [12]) and grows shorter as the electron density increases. Taking into account elastic collisions, the mean free path of these molecules will be even shorter.

The hollow n=2 excited neutral profiles yield the useful information that there is very

little $n=2$ production in the centre of the beam. Knowing the electron excitation rate of ground state atoms to the $n=2$ level, we can therefore estimate an upper limit on the density of ground state hydrogen in the centre of the beam. The Abel inversion of the lateral $n=2$ density measurement tells us that there is zero $n=2$ density in the centre of the beam. Allowing for the uncertainty in the Abel inversion (with a wide margin), we can assume that the $n=2$ density in the centre has a *maximum* possible value of half of the peak value. To calculate a maximum ground state density n_H , we assume that there are no other production mechanisms apart from electron excitation from the ground state that contribute to the $n=2$ density in the centre of the beam. We also assume maximum efficiency of the loss mechanisms and therefore that the escape factor, Λ_{21} is equal to one. This gives us the balance:

$$n_H = \frac{n_2(n_e K_2 + A_{21} \Lambda_{21})}{n_e K_{12}} \quad (4.28)$$

For the 6.5 Pa measurement, we assume a maximum $n=2$ density in the centre of the beam of $1.2 \cdot 10^{16} \text{ m}^{-3}$. This gives us a maximum possible ground state neutral density in the very centre of the beam of $n_H = 7 \cdot 10^{19} \text{ m}^{-3}$. Given the central electron density of $4 \cdot 10^{20} \text{ m}^{-3}$, we obtain a minimum ionization degree in the centre of the beam of 85 %. For the 50 Pa measurement we assume a maximum $n=2$ density of $9 \cdot 10^{16} \text{ m}^{-3}$ and obtain a maximum n_H density of $3.7 \cdot 10^{20} \text{ m}^{-3}$ and a minimum ionization degree of 68 %.

Another important feature of the lateral $n=2$ density measurements is the absolute value of the peak $n=2$ density. We can use it to estimate the density of $\text{H}_2(v \geq 4)$ in the vessel by setting up a balance between creation and destruction of $n=2$ neutrals:

$$n_2(n_e K_2 + \Lambda_{21} A_{21}) = 0.3 n_e n_{\text{H}_2(v \geq 4)} k_{cx} \quad (4.29)$$

$$n_{\text{H}_2(v \geq 4)} = \frac{n_2(n_e K_2 + \Lambda_{21} A_{21})}{0.3 n_e k_{cx}} \quad (4.30)$$

For $P = 6.5 \text{ Pa}$, this gives $n_{\text{H}_2(v \geq 4)} = 3.9 \cdot 10^{19} \text{ m}^{-3}$ and for $P = 50 \text{ Pa}$, this gives $n_{\text{H}_2(v \geq 4)} = 1.34 \cdot 10^{20} \text{ m}^{-3}$. That is around 30 % and 13.3 % respectively of the total hydrogen molecular density.

In this simple consideration, we have neglected the possibility that production may also take place via 3-particle recombination or direct excitation. However, these processes would be expected to be more important in the centre of the beam, where the electron density is higher, and total production is very small here. Other possibilities for production are mutual neutralization of H^- atoms and dissociative recombination of H_3^+ ions. The populations of these ions are expected to be negligible.

The third important feature of the lateral $n=2$ density profiles is the part of the profile outside of the plasma beam. We used this halo in Sect. 4.5 to estimate ground state densities outside the plasma beam.

4.6.3 Summary of determined neutral densities

Using electron density and radial dependent measurements of the n=2 excited population in Pilot-PSI we have been able to obtain a rich set of information about neutrals in the plasma. In Sect. 4.6.2 we found with a great deal of certainty that at high electron densities (obtained at 0.4 T, 6.5 Pa), the ground state density in the centre of the beam is $n_H < 7 \cdot 10^{19} \text{ m}^{-3}$ giving an ionization degree of $> 85 \%$. At approximately ten times higher background pressure (50 Pa), the ground state density is $n_H < 3.7 \cdot 10^{20} \text{ m}^{-3}$ and the ionization degree $> 68 \%$. If we assume that the hypothesis put forward for the existence of a ‘hot’ and a ‘cold’ population in Sect. 4.4.2 is correct, we can estimate these values more accurately. The escape factors calculated in Sect. 4.6.1 were used to calculate neutral densities in the beam. The results were $n_H = 2.22 \cdot 10^{19} \text{ m}^{-3}$ at 6.5 Pa and $1.11 \cdot 10^{20} \text{ m}^{-3}$ at 50 Pa, corresponding to ionization degrees of 95 % and 88 % respectively. These are important results as they suggest that in plasma surface interaction experiments most particles impinging on the target are ions and not neutrals.

Estimations for the neutral density *outside* of the beam, give the dissociation degree in the vessel, which is important for modelling of the plasma/background gas system [26]. In Sect. 4.5, the dissociation degree was estimated using a Monte Carlo model for the Lyman- α photons compared to n=2 density profiles. The approximate ground state neutral densities were found to be $5 \cdot 10^{18} \text{ m}^{-3}$ (6.5 Pa) and $5 \cdot 10^{19} \text{ m}^{-3}$ (50 Pa) yielding a dissociation degree of 4 % and 5 % respectively.

The $\text{H}_2(v \geq 4)$ density was estimated in Sect. 4.6.2 from the peak values of the n=2 population density. The densities found were $3.9 \cdot 10^{19} \text{ m}^{-3}$ (6.5 Pa) and $1.34 \cdot 10^{20} \text{ m}^{-3}$ (50 Pa). This corresponds to 30 % and 13.3 % of the total H_2 density in the vessel respectively (compared to 0.14 % in [25]). In Sect. 4.6.2, we saw that these percentages rise dramatically in the transition from a low electron density, low magnetic field regime to the high electron density regime. At 20 Pa and 0.015 T, the minimum rise in this percentage is from $< 4.3 \%$ at low current to at least 19.4 % at high current.

4.7 Discussion of the diagnostic method for determination of ion parameters

The rotation velocity and temperature of ions have been measured in Sect. 4.4.2 via the n=2 excited neutrals. Laser induced fluorescence is in principle an ideal method of measuring these parameters because of its high spatial resolution. It has however proven to be problematic in the high electron density plasma of Pilot-PSI. The main problems are electron de-excitation that competes with the fluorescence signal, the background emission that grows by at least a factor of ten when the magnetic field strength is increased from 0.015 T to 0.4 T, and the hollow n=2 density profile at high electron densities which ensures that zero signal is measured in the centre of the beam.

Absorption has proven to be a good replacement diagnostic, even though Abel inversion is required to obtain radial density profiles and information obtained from spectra are averages over the line of sight of the laser. Absorption ratios of down to $7 \cdot 10^{-4}$ have

been measured and the wavelength resolution is good (spectral linewidth < 300 kHz). Ion velocity and temperature information could be obtained from asymmetric spectra at high electron density and high magnetic field (0.4 T), but could not be obtained from the symmetric spectra measured at low field (0.015 T) because of ambiguity in the coupling of these neutrals with ions. Figs. 4.9 and 4.10 show the ion parameters obtained. Rotation velocities of about 5 to 7 km/s are in agreement with typical rotation velocities at a magnetic field strength of 0.4 T using optical emission spectroscopy on the H_{β} line in Chap. 3. Ion temperatures are found to be approximately equal to the electron temperatures, but since they are line of sight measurements, they are expected to be lower limits on the real ion temperature. Heating of the ions above the electron temperature is attributed to ion viscous heating in Chap. 3.

The signal to noise ratio of the absorption diagnostic could be further improved by more averaging, by the use of a lock-in amplifier and by the use of a real time I_0 laser power measurement. This last idea would involve splitting the laser beam and guiding both beams through the vessel, with only one of the beams penetrating the plasma. A further improvement to the diagnostic could be achieved by ensuring a non-hollow $n=2$ density profile, such that the centre of the plasma beam can be seen. The upgrade to Pilot-PSI, Magnum-PSI [4] is foreseen to have a broader plasma diameter (~ 10 cm) and a lower background pressure (< 1 Pa near the target). The expectation is MAR will become less important for the production of emission, firstly because the density of $H_2(v \geq 4)$ will be lower and secondly because these molecules will only be able to penetrate the edge of the beam. A larger fraction of the excited neutrals can then be expected to originate from direct electron excitation and three particle recombination in the centre.

4.8 Conclusion

This paper explains a methodology using $n=2$ excited atoms, for determining ion parameters and neutral densities in a linear, hydrogen, magnetized plasma with ITER divertor relevant electron parameters. Measurements were made in this regime in the beam of Pilot-PSI using LIF and absorption. Absorption was found to have a much better sensitivity than LIF, mainly due to competition with background emission. At 4 cm from the source (half a meter from the target) the following parameters were measured: ion rotation velocities up to 7 km/s and ion temperatures of 2-3 eV $\sim T_e$. Comparison of measurements with modelling yielded also the following information: a central ionization degree of $> 85\%$, a dissociation degree in the vessel of $\sim 4\%$ and an escape factor for the Lyman- α line of ~ 0.6 . 30% of molecules were found to have a rovibrational excitation of more than 2 eV, a significant increase with respect to low density, less magnetized plasmas. The effect of a ten-fold increase in pressure did not significantly affect the dissociation degree in the vessel. However, it did reduce the proportion of $v > 4$ excited molecules (by $\sim 17\%$) and the escape factor of the Lyman- α line (to ~ 0.15). In a doubling of the electron density in the transition to high electron densities, the proportion of rovibrationally excited molecules (excitation more than 2 eV) was found to increase by more than a factor of four, probably because of a large increase in the production and

confinement of ground state neutrals.

References

- [1] J. Roth *et al.*, “Recent analysis of key plasma wall interaction issues for ITER,” *J. Nucl. Mater.*, vol. 390-391, pp. 1–9, 2009.
- [2] H. J. van der Meiden *et al.*, “High sensitivity imaging Thomson scattering for low temperature plasma,” *Rev. Sci. Instrum.*, vol. 79, p. 013505, 2008.
- [3] G. J. van Rooij *et al.*, “Thomson scattering at Pilot-PSI and Magnum-PSI,” *Plasma Phys. Controlled Fusion*, vol. 51, p. 124037, 2009.
- [4] H. J. N. van Eck *et al.*, “Pre-design of Magnum-PSI: A new plasma-wall interaction experiment,” *Fusion Eng. Des.*, vol. 82, no. 1878, 2007.
- [5] D. M. Goebel, G. Campbell, and R. W. Conn, “Plasma surface interaction experimental facility (PISCES) for materials and edge physics studies,” *J. Nucl. Mater.*, vol. 121, pp. 277–282, 1984.
- [6] N. Ohno *et al.*, “Static and dynamic behaviour of plasma detachment in the divertor simulator experiment NAGDIS-II,” *Nucl. Fusion*, vol. 41, p. 1055, 2001.
- [7] W. Bohmeyer, A. Markin, and C. Biedermann, “Erosion of CFC at medium flux densities in the plasma generator PSI-2,” *Phys. Scripta*, vol. T138, p. 014016, 2009.
- [8] S. Mazouffre, M. G. H. Boogaarts, I. S. J. Bakker, P. Vankan, R. Engeln, and D. C. Schram, “Transport of ground-state hydrogen atoms in a plasma expansion,” *Phys. Rev. E*, vol. 64, p. 016411, 2001.
- [9] M. J. de Graaf, R. Severens, R. P. Dahiya, M. C. M. van de Sanden, and D. C. Schram, “Anomalous fast recombination in hydrogen plasmas involving rovibrational excitation,” *Phys. Rev. E*, vol. 48, p. 2098, 1993.
- [10] U. Fantz, “Hydrogen molecules in the divertor of ASDEX upgrade,” *J. Nucl. Mater.*, vol. 290-293, pp. 367–373, 2001.
- [11] J. K. Janev, W. D. Langer, J. K. Evans, and J. D. E. Post, *Elementary Processes in Hydrogen-Helium Plasmas*. Springer-Verlag, 1987.
- [12] P. S. Krstic, “Inelastic processes from vibrationally excited states in slow $H^+ + H_2$ and $H + H_2^+$ collisions: Excitations and charge transfer,” *Phys. Rev. A*, vol. 66, p. 042717, 2002.
- [13] R. K. Janev, D. Reiter, and U. Samm *Tech. Rep. Jül-4105*, vol. Jül-4105, 2003.
- [14] W. J. Goedheer, *Models for a steady-state plasma in a gas blanket*. PhD thesis, Rijksuniversiteit Utrecht, 1978.
- [15] J. A. M. van der Mullen and D. C. Schram, “On the atomic state distribution function in inductively coupled plasmas-III. Rate coefficients and properties of atomic states,” *Spectrochim. Acta*, vol. 45B, no. 3, pp. 233–247, 1990.

- [16] W. A. J. Vijvers *et al.*, “Optimization of the output and efficiency of a high power cascaded arc hydrogen plasma source,” *Phys. Plasmas*, vol. 15, no. 093507, 2008.
- [17] K. Behringer and U. Fantz, “The influence of opacity on hydrogen excited-state population and applications to low-temperature plasmas,” *New Journal of Physics*, vol. 2, p. 23, 2000.
- [18] R. J. Rosado, *An investigation of non-equilibrium effects in thermal argon plasmas*. PhD thesis, Technische Hogeschool Eindhoven, 1981.
- [19] G. J. van Rooij *et al.*, “Extreme hydrogen plasma densities achieved in a linear plasma generator,” *Appl. Phys. Lett.*, vol. 90, p. 121501, 2007.
- [20] J. Westerhout, N. J. Lopes Cardozo, J. Rapp, and G. J. van Rooij, “CH spectroscopy for carbon chemical erosion analysis in high density low temperature hydrogen plasma,” *Appl. Phys. Lett.*, vol. 95, no. 151501, 2009.
- [21] G. M. W. Kroesen, D. C. Schram, and J. C. M. de Haas, “Fast deposition of amorphous hydrogenated carbon films using a supersonically expanding arc plasma,” *Plasma Chem. Plasma Proc.*, vol. 10, p. 531, 1990.
- [22] W. Demtröder, *Laser Spectroscopy, Basic Principles*, vol. 1. Springer-Verlag, 2008.
- [23] B. H. Armstrong, “Spectrum line profiles: the Voigt function,” *J. Quant. Spectrosc. Radiat. Transfer*, vol. 7, pp. 61–88, 1967.
- [24] M. C. M. van de Sanden, *The Expanding Plasma Jet: Experiments and Model*. PhD thesis, Technische Universiteit Eindhoven, 1991.
- [25] P. Vankan, D. C. Schram, and R. Engeln, “Atomic and molecular hydrogen densities in a plasma expansion,” *Plasma Sources Sci. Technol.*, vol. 14, pp. 744–750, 2005.
- [26] H. J. N. van Eck *et al.*, “Modeling and experiments on differential pumping in linear plasma generators operating at high gas flows,” *J. Appl. Phys.*, vol. 105, p. 063307, 2009.

Chapter 5

Two dimensional electric current effects on a magnetized plasma in contact with a surface

Abstract

Significant electric fields both parallel and perpendicular to a magnetic field have been observed and modelled self-consistently in an ITER divertor relevant plasma-wall experiment. Due to magnetization, electric current is found to penetrate the plasma beam outside of the cascaded arc plasma source with a length scale proportional to $\sqrt{1 + H^2}$, where H is the Hall parameter. Plasma rotation measurements and chemical erosion profiles at a carbon target demonstrate that for a sufficiently well-magnetized plasma, a current through the target causes plasma-wall sheath potentials to significantly increase in a region of net ion collection while for the conditions studied, regions of net electron collection remain unaffected.

5.1 Introduction

A magnetized plasma can support potential differences which, if short-circuited by a conducting surface, give rise to an electric current through the surface. This current influences the sheath potentials at the surface. Determination of the resulting sheath potential profile is important, since it determines the particle and energy flux to the surface. We consider plasma beams with such high ion fluxes ($> 10^{23} \text{ m}^{-2}\text{s}^{-1}$) that the ion saturation current at the surface is significant ($> 10 \text{ kA/m}^2$). Since the resistivity parallel to the magnetic field is also high ($> 10^{-4} \Omega\text{m}$), significant parallel electric fields can arise. This chapter answers the question how the plasma sheath conditions are affected in this very general case where perpendicular and parallel electric fields, magnetization and the ion saturation current can all play a significant role, and self-consistently determines the 2-dimensional current distribution in the plasma beam and the sheath potentials at the surface.

An important application can be found in magnetic fusion. Electric currents are expected in the conducting divertor of the tokamak ITER [1; 2], where the ambient plasma conditions will be in the regime described above. Understanding plasma-wall sheath potentials at this divertor is paramount for understanding the erosion, one of the key issues in magnetic fusion research [3]. Currents are known to flow in a tokamak between the inner and outer divertor. They are caused either by a difference in sheath voltage at the surfaces arising from a temperature difference [4; 5; 6], or by an independently arising loop voltage [7]. Currents may also flow within a single divertor plate [8] due to radial electric fields (parallel to the divertor plates) [9].

The latter case has an analogy in linear magnetized divertor simulators [10; 11; 12]. In this chapter, we develop a generic model for such a linear plasma experiment, that can be adjusted for application to a tokamak divertor. Three different cases are considered: two with a conducting target perpendicular to the magnetic field in which the magnetization of the plasma is varied, and one in which current flow is inhibited by an insulating insert. We analyze the effect of the magnetization of the plasma and current through the target on the plasma current configuration and the plasma-wall sheath profile. The experiment is introduced in Sect. 5.2, the model explained in Sect. 5.3 and the experimental approach outlined in Sect. 5.4. Results and conclusions are given in sections 5.5 and 5.6.

5.2 Experimental

The experiments were performed in the linear plasma generator Pilot-PSI (see Fig. 2.1), with typical ion fluxes of $\sim 10^{24} \text{ m}^{-2}\text{s}^{-1}$, at an electron temperature of $\sim 1 \text{ eV}$. The plasma is produced in a cascaded arc source where gas is ionized by a typical voltage difference of 100 V between cathode tips and the grounded source nozzle. The plasma flows into a low pressure vessel ($\sim 5 \text{ Pa}$) where it is confined by an axial magnetic field of 0.4 T to a beam width of $\sim 1 \text{ cm}$ and impinges on a removable target at a distance of 0.5 m from the source. The plasma parameters n_e and T_e are monitored with Thomson scattering (TS) 4 cm downstream of the source and 2 cm in front of the target.

Electric fields are deduced from the $\vec{E} \times \vec{B}$ drift of plasma ions: $v = \vec{E} \times \vec{B} / B^2$. Ion rotation velocities are determined indirectly by virtue of their strong coupling with excited, radiating atoms. These excited atoms emit Balmer- β spectra that are asymmetric because of a second population coupled to cold, non-rotating neutrals. The spectra are measured as explained in Sect. 3.2.2. Analysis with a double Voigt function is used to determine the Doppler shift of the population coupled to the ions. See Chap. 3 for more details. Spectra measured close to the target are symmetric and are analyzed using a single Voigt fit. Since we are measuring excited neutrals and not ions directly, it should be noted that the results are a lower limit on the true electric field values.

Other diagnostics include a conducting target with probe in its centre. The set up for this ‘target probe experiment’ is shown in Fig. 5.1. A 3 mm diameter copper probe sur-

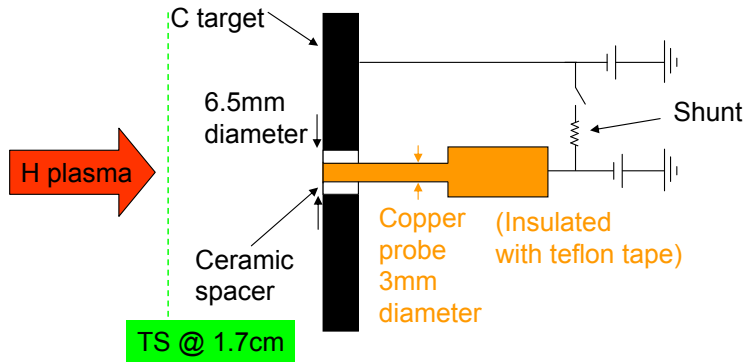


Figure 5.1: Set up for ‘target probe experiment’ with an insulating insert to inhibit current flow through the target. By allowing current to flow through the shunt, we can measure the current that would have flowed through a conducting target without insulating insert.

rounded by a 1.75 mm wide ceramic spacer is inserted in a carbon target. The floating potential of the probe and of the target are measured. The probe and target can be electrically connected outside of the vessel via shunts of varying resistance over which the voltage is measured.

A final diagnostic is the erosion of carbon targets on plasma exposure. This gives an indirect indication of the ion energy at the target. The targets are fine grain carbon discs, 30 mm in diameter and 4 mm thick. They are clamped onto a copper target holder at floating potential, and are cooled directly by pressurized water.

5.3 Modelling

5.3.1 Background

Due to magnetization of the charged plasma species in Pilot-PSI, the cross-field electrical conductivity, σ_{\perp} in the plasma beam is drastically reduced with respect to the conductivity parallel to the field, σ_{\parallel} .

$$\sigma_{\perp} = \frac{0.51\sigma_{\parallel}}{(1 + H^2)} [13] \quad (5.1)$$

The Hall parameter $H = \omega/\nu$, is a measure of the magnetization of the plasma, defined as the ratio between the cyclotron frequency $\omega = eB/m$ and the frequency of radial diffusion causing collisions, ν .

The large reduction in radial conductivity associated with magnetization determines the behavior of the current from the cascaded arc source. As shown schematically in Fig. 5.2(a), the current from the grounded nozzle of the source must radially cross the magnetic field to close the circuit to the cathode tips.

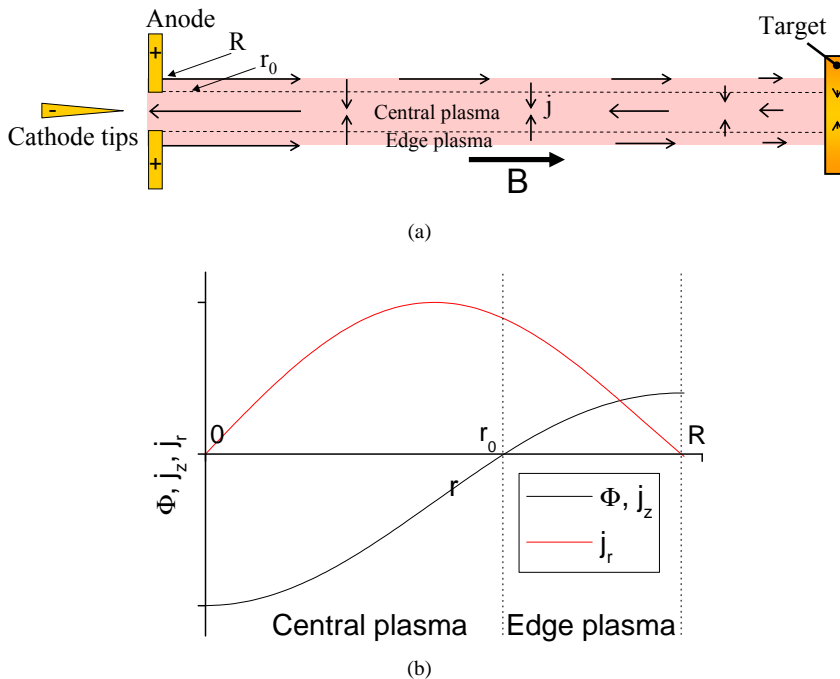


Figure 5.2: (a) Schematic picture of the plasma beam of Pilot-PSI with indication of current flow. (b) Normalized solutions for Φ , j_z and j_r plotted as a function of radius with sign chosen to agree with definitions (see Sect. 5.3.2).

Electrons are more mobile than ions parallel to the magnetic field, and for all conditions studied in this chapter, also in the direction perpendicular to the field. We therefore approximate the parallel conductivity σ_{\parallel} and the Hall parameter H , by the values for the electrons. σ_{\parallel} is given by the Spitzer resistivity [14] and the Hall parameter is taken to be the electron Hall parameter, H_e . The most important diffusion causing collisions for electrons are Coulomb interactions with ions. The frequency of these collisions is $\nu_{ei} = 2.9 \cdot 10^{-12} n_e \hat{T}_e^{-3/2} \ln(\Lambda)$ [13], where \hat{T}_e is the electron temperature in electron Volts and $\ln(\Lambda)$ is the Coulomb logarithm [13]. The electron Hall parameter can then be expressed as:

$$H_e = \frac{e}{2.9 \cdot 10^{-12} m_e \ln(\Lambda)} \frac{B \hat{T}_e^{3/2}}{n_e} \quad (5.2)$$

Note it increases linearly with magnetic field, decreases with electron density and increases strongly with electron temperature. For the plasma conditions presented in this chapter, this Hall parameter has values of between 3 and 55.

5.3.2 Modelling electric fields and currents in plasma beam

A model of the current path in Pilot-PSI is constructed from $\vec{\nabla} \cdot \vec{j} = 0$ for the current density together with the assumption of cylindrical symmetry. Poloidal current and its effects as well as the electric field associated with the density gradient can be ignored. The current density $\vec{j}(r, z)$ is then related to the electric potential $\Phi(r, z)$ as:

$$\vec{j}(r, z) = \left(-\sigma_{\perp} \frac{\partial \Phi}{\partial r}, -\sigma_{\parallel} \frac{\partial \Phi}{\partial z} \right) \quad (5.3)$$

So:

$$\vec{\nabla} \cdot \vec{j} = - \left(\frac{\sigma_{\perp}}{r} \frac{\partial}{\partial r} \left(r \frac{\partial}{\partial r} \right) + \sigma_{\parallel} \frac{\partial^2}{\partial z^2} \right) \Phi = 0 \quad (5.4)$$

Inserting a general solution for Φ of the form:

$$\Phi(r, z) = \phi_{-}(r) e^{-kz} + \phi_{+}(r) e^{kz} \quad (5.5)$$

gives:

$$- \left(\sigma_{\perp} \frac{\partial^2}{\partial r^2} + \frac{\sigma_{\perp}}{r} \frac{\partial}{\partial r} + k^2 \sigma_{\parallel} \right) (\phi_{-}(r) e^{-kz} + \phi_{+}(r) e^{kz}) = 0 \quad (5.6)$$

from which we determine that:

$$\frac{\partial^2 \phi_{\pm}}{\partial r^2} + \frac{1}{r} \frac{\partial \phi_{\pm}}{\partial r} + k^2 \frac{\sigma_{\parallel}}{\sigma_{\perp}} \phi_{\pm} = 0 \quad (5.7)$$

This can be written in the form of the Bessel differential equation:

$$\alpha^2 \frac{\partial^2 \phi_{\pm}}{\partial \alpha^2} + \alpha \frac{\partial \phi_{\pm}}{\partial \alpha} + (\alpha^2 - n^2) \phi_{\pm} = 0 \quad (5.8)$$

with $\alpha = kr\sqrt{\sigma_{\parallel}/\sigma_{\perp}}$, $n = 0$ and solution:

$$\phi_{\pm} = cJ_0(\alpha) = cJ_0\left(rk\sqrt{\frac{\sigma_{\parallel}}{\sigma_{\perp}}}\right) \quad (5.9)$$

$\Phi(r, z)$ is thus given by:

$$\Phi = \Phi_0[c_-e^{-kz} + c_+e^{kz}]J_0\left(rk\sqrt{\frac{\sigma_{\parallel}}{\sigma_{\perp}}}\right) \quad (5.10)$$

Using the identity $\partial J_0(ax)/\partial x = -aJ_1(ax)$ we can describe the axial and radial currents as

$$j_r = -\sigma_{\perp}\frac{\partial\Phi}{\partial r} = (c_-e^{-kz} + c_+e^{kz})\sqrt{\sigma_{\perp}\sigma_{\parallel}}kJ_1\left(rk\sqrt{\frac{\sigma_{\parallel}}{\sigma_{\perp}}}\right) \quad (5.11)$$

and

$$j_z = -\sigma_{\parallel}\frac{\partial\Phi}{\partial z} = -(c_-e^{-kz} + c_+e^{kz})\sigma_{\parallel}kJ_0\left(rk\sqrt{\frac{\sigma_{\parallel}}{\sigma_{\perp}}}\right) \quad (5.12)$$

The solutions correspond to the picture of a current channel spreading out of the source into the vessel as shown schematically with arrows in the picture of the plasma in Fig. 5.2(a). Normalized solutions for Φ , j_z and j_r are plotted in Fig. 5.2(b) as a function of radius. The sign is chosen so that the the potential is highest at the anode of the source, and so that the current flows from anode to cathode, where positive current directions are defined as being from the source towards the target and from the anode radially inwards.

Let us take a closer look at these solutions. As an aid to intuition, it is useful to realize that the same problem solved in cartesian co-ordinates would give solutions proportional to $\sin(x)$ and $\cos(x)$ functions instead of Bessel functions. The plots in Fig. 5.2(b) show that the axial current is positive (flows away from the source) in the range $r_0 < r < R$ (we define this as the ‘edge plasma’) and negative (back towards the source) in the range $0 < r < r_0$ (the ‘central plasma’). The strength of the radial current is proportional to the derivative of the potential. It is weakest in the centre and at the edges of the beam and strongest in between.

The existence of both positive and negative exponential functions for the axial dependence of the above named quantities, reflects the tendency of the plasma to support a radial electric field which decays in both positive and negative axial directions. In the case of Pilot-PSI, the largest externally generated electric field (up to 5000 V/m measured close to the source) arises in the plasma source and will decay axially towards the target. Interruption of this exponential decay by the target ensures an electric field across the target at the sheath edge. This electric field will decay axially from the target back towards the source.

Another example of a radial electric field arising at the target end of the beam, is that caused by radial temperature differences. In the absence of current effects (that we will discuss later), the sheath potential is proportional to the electron temperature, $V_{sheath} \sim 2.5 kT_e/e$ [8], where T_e is the electron temperature in Kelvin. This radially

changing sheath potential causes a radial electric field (in the order of 300 V/m) in front of the target because the sheath forms in front of a highly conductive and thus equipotential target plate.

The characteristic axial decay length of potential and currents, k , can be determined by integrating the axial current density across the radius of the beam. When the target is at floating potential such that all current must return to the source, this integral should be equal to zero.

$$2\pi \int_0^R j_z r dr = -2\pi \sqrt{\sigma_{\parallel} \sigma_{\perp}} \Phi_0 (-c_1 e^{-kz} + c_2 e^{kz}) J_1(Rk \sqrt{\frac{\sigma_{\parallel}}{\sigma_{\perp}}}) = 0 \quad (5.13)$$

Then,

$$J_1(Rk \sqrt{\frac{\sigma_{\parallel}}{\sigma_{\perp}}}) = 0 \quad (5.14)$$

Therefore,

$$Rk \sqrt{\frac{\sigma_{\parallel}}{\sigma_{\perp}}} = \xi \quad (5.15)$$

where $\xi \approx 3.83$ is the first positive root of J_1 . So

$$k = \frac{\xi}{R} \sqrt{\frac{\sigma_{\perp}}{\sigma_{\parallel}}} \quad (5.16)$$

By setting $\ell_{\parallel} = 1/k$ and $\ell_{\perp} = R$, we can compare the parallel and perpendicular length scales of the current that penetrates into the vessel. Using also Equation 5.1 we obtain:

$$\frac{\ell_{\parallel}}{\ell_{\perp}} = \frac{1}{\xi} \sqrt{\frac{\sigma_{\parallel}}{\sigma_{\perp}}} = \frac{1}{\xi} \sqrt{1.95(1 + H^2)} \quad (5.17)$$

where $H \approx H_e \propto B \hat{T}_e / n_e$ for the conditions studied in this paper.

5.3.3 Modelling the effect of current through a surface on the plasma-wall sheath

Having studied the effect of a radial electric field on the magnetized, open ended plasma beam of Pilot-PSI, we now consider the effect of an electric field across a conducting target in contact with a magnetized plasma. We first consider the simplest case for which ℓ_{\parallel} is so much longer than ℓ_{\perp} that we can ignore radial current flow. The electric system can then be modelled with a simple replacement circuit as shown in the inset of 5.3. The central and edge plasma are modelled with two replacement resistors (R_{centre} and R_{edge} respectively) and the plasma-wall sheath for the inner and outer plasma with two diodes (Vsh_{centre} and Vsh_{edge}). The total voltage difference applied (or existing) across the system is labelled V_{tot} . Simple Ohm's law then gives:

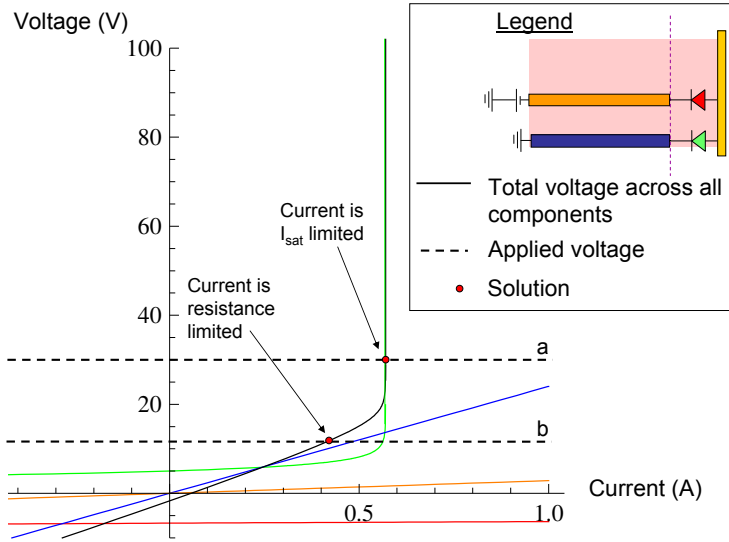


Figure 5.3: Modelling of the plasma at typical high Hall parameter conditions with a simple electric replacement circuit. Radial current flow is ignored. The plasma beam is divided into two regions, edge and centre. The plasma resistance and plasma-wall sheath in each region are modelled with a replacement resistor and a diode. The voltage drop over each circuit component is plotted as a function of current. The black plot indicates the sum over the four circuit components. Two characteristic solutions are indicated for different values of the voltage over the circuit. See text for details.

$$V_{tot} = IR_{edge} + Vsh_{edge} - Vsh_{centre} + IR_{centre} \quad (5.18)$$

The I-V characteristic for a plasma-wall sheath (the diode components) is given by [8]:

$$I = I_{sat} + \frac{1}{4}en_0\sqrt{\frac{8kT_e}{\pi m_e}}\exp\left(\frac{eVsh}{kT_e}\right) \quad (5.19)$$

where I_{sat} is the ion saturation current and is equal to the ion flux, n_0 is the electron density far from the sheath [m^{-3}] and e is the (negative) electron charge. The positive direction for current and voltage is the same as defined earlier, away from the source, towards the target. This expression describes a constant ion (saturation) current through the sheath with an electric current that decays exponentially with sheath potential. The expression holds only for negative values of Vsh and thus ignores the decay in the ion current expected for increasing positive values of Vsh . As we will show in Sect. 5.5, this is justified for the conditions studied in this chapter since the negative current through the central sheath is limited by the current through the edge sheath and is not large enough

to change the polarity of the sheath. For zero current, the value of V_{sh} is $\sim 2.5 kT_e/e$. A small change in this voltage gives a large change in the current, except when the voltage is so large that the ion saturation current I_{sat} has been reached. Then the voltage can become arbitrarily large with no further change in current.

We describe the effect of a current through the target on the sheath potentials with the aid of Fig. 5.3. This figure describes the voltage over each of the replacement circuit components as a function of current, for typical plasma conditions (with a high Hall parameter). The current through the resistors depends linearly on voltage (temperature dependence is ignored). The current through the sheath components behaves as explained above. When the voltage is high enough to repel all electrons, the ion saturation current will be reached, in this case at just over 0.5 A. This limits the current through the entire system. The current through the central sheath is in the other direction, so ion saturation is not obtained (unless the current direction is reversed). The black line indicates the sum of the voltage drop over the four circuit components. Solutions are indicated (by a red dot) for two different values of the voltage applied across the circuit. We distinguish two cases:

1. The current through the target is **I_{sat} limited** - Note the value of the edge sheath voltage (green curve) for the solution given applied voltage a. It is clear from this plot that any further increase in the applied voltage would result not in an increase in the current, but in an increase in the voltage over the edge sheath.

2. The current through the target is **resistance limited** - For the solution, given applied voltage b, this voltage falls mostly over the plasma. A further increase in the applied voltage would lead to an increase in the current through the system and thus in the voltage drop over the plasma.

5.3.4 Combination of modelling in beam and at plasma-wall transition

Combining the modelled electric field behaviour in the free plasma with the sheath behaviour due to a current through the target, we find that the combined system behaves as shown in Fig. 5.4. The potential is sketched as a function of the distance along the current path, from the anode (the nozzle of the source), through the edge of the plasma beam, through the target and back through the central plasma ending just downstream of the source opening. V_{tot} is defined as the potential at the exit of the plasma source between inner and outer plasma regions. The sheath behaviour is displayed by means of a magnified scale on the x-axis in the proximity of the target.

As in the previous section, we identify two cases (with a conducting target), this time defined by a large or small value of the Hall parameter. For the low Hall parameter case, the current flow is such that the potential difference V_{tot} falls entirely over the plasma beam. The current through the target is lower than I_{sat} . The current in the system is therefore determined by the resistance of the plasma. The sheath potentials are then approximately equal to their value for zero current, $\sim 2.5 kT_e/e$, which differs between the central and edge plasma. For the high Hall parameter case, the axial exponential

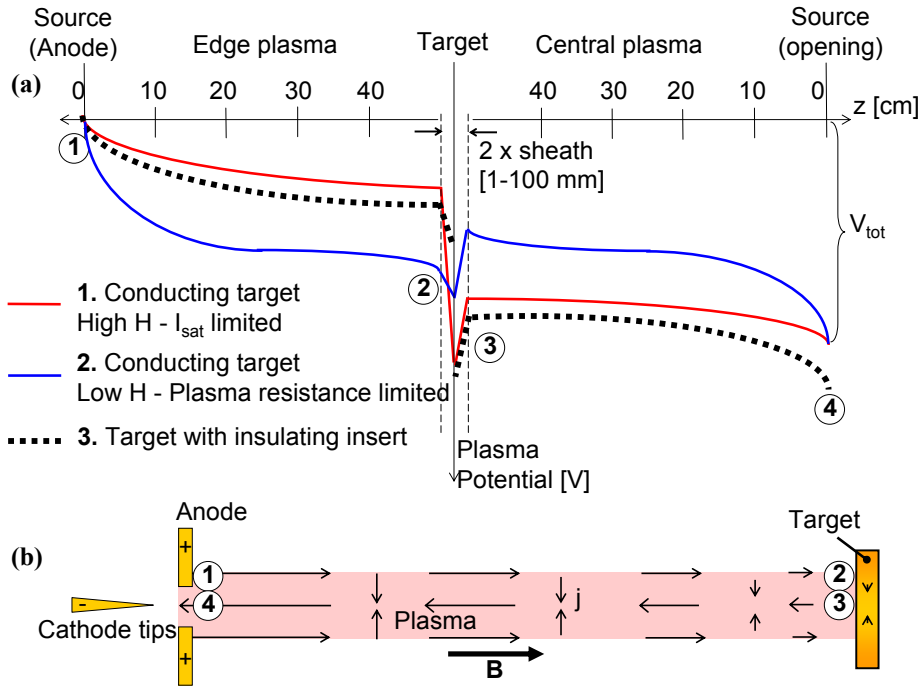


Figure 5.4: (a) The modelled plasma potential is illustrated schematically along the current path from the source anode, through the target and back to the source opening. The sheath behaviour is shown by means of a magnified scale. Three cases are shown, 1. A conducting target near a high Hall parameter plasma where the current at the target is limited by I_{sat} , 2. A conducting target with a low Hall parameter plasma where the current in the system is limited by the plasma resistance and 3. A case in which the inner and outer target are electrically insulated from one another. (b) Schematic view of the Pilot-PSI plasma, depicting the current configuration shape. The circled numbers show the positions in the plasma corresponding to positions on the schematic graph above it.

decay length is longer such that V_{tot} cannot fall entirely over the plasma beam. As we saw in the previous section, the remaining potential then falls over the edge sheath. The current through the system is determined by the boundary condition for the edge plasma, $I = I_{\text{sat}}$.

In order to emphasize the effect of a conducting target interfacing with a magnetized plasma, we also consider a third case in which electric currents are inhibited from flowing through the target. The first consequence is that the resistance of the whole plasma-target system will be larger and for a given current, V_{tot} will be larger. Since it is now possible for inner and outer targets to be at different potentials, there is no increase in edge sheath potential.

5.4 Experimental approach

Measurements have been carried out for two specific plasma conditions with a conducting target and a magnetic field strength of 0.4 T. The source discharge current was 200 A in both cases, the gas flow 1 slm and 2 slm. The radial profiles of the electron temperature and electron density at 4 cm from the source and 2 cm from the target are shown in Fig. 5.5. The main difference between the two conditions is the electron temperature, especially the temperature measured near the target. The profiles are peaked with maximum values of 0.3 eV and 1.1 eV near the target and 3 eV and 3.7 eV near the source. The corresponding n_e profiles are also peaked and do not differ greatly from one another. The Hall parameters calculated for the peak electron parameters near the target are 3 and 12 respectively. These conditions will henceforth be called the ‘H = 3 case’ and the ‘H = 12 case’. Near the source the Hall parameters corresponding to the peak electron parameters are 47 and 55. We perform a rough test of the simple model, by measuring the decay of the radial electric field as a function of axial distance. We compare the strength of this observed axial decay to the characteristic distance ℓ_{\parallel} predicted using the Hall parameter calculated from measured electron parameters.

Using our model, electric field measurements in front of the target are then used to estimate the sheath potential profile at the target. Current flow and potentials at the target are then studied in more detail using the ‘target probe experiment’ (Fig. 5.1). Plasma conditions at the target for these measurements are $T_e = 1$ eV and $n_e = 10^{20} \text{ m}^{-3}$, corresponding to a Hall parameter of 30. The floating potential of the probe and of the target are measured as well as the electric current between them when the two are connected via shunts of varying resistance.

We then turn to study of the sheath behaviour in the centre of the target. An I-V-characteristic of the probe is measured. Also, an indirect indication of the ion energy at the target is obtained by observing the erosion profiles of carbon targets exposed to the ‘H = 3’ and ‘H = 12’ plasma conditions, each for 100 seconds. Surface depth profiles are made ex-situ with a surface profilometer.

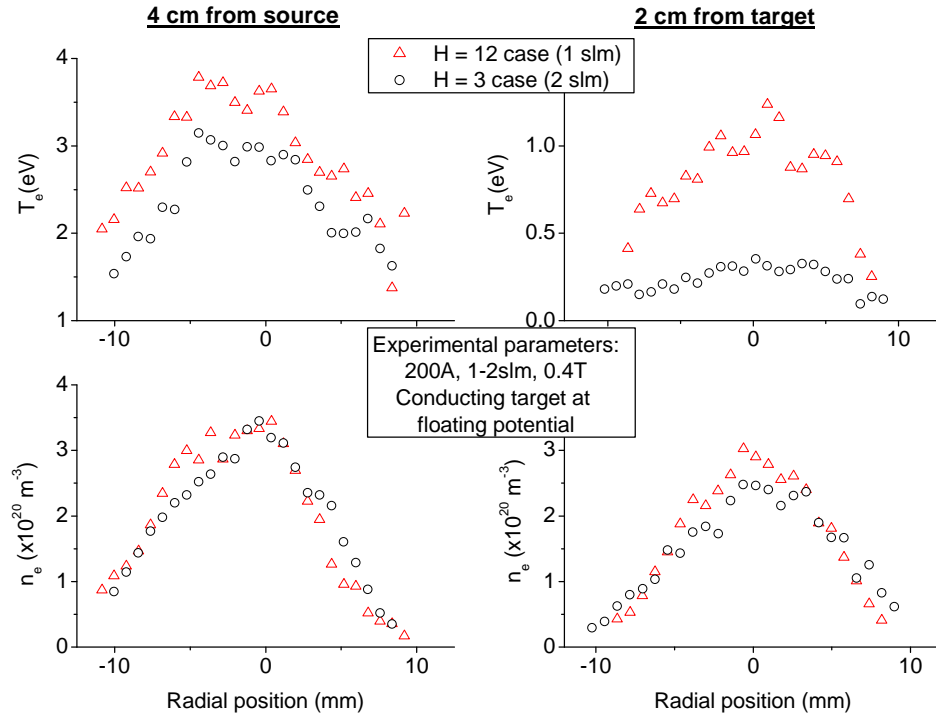


Figure 5.5: Electron density and electron temperature profiles for the two plasma conditions studied, measured at positions 4 cm from the source and 2 cm from the target. We name them the ‘H = 3 case’ and the ‘H = 12 case’ according to the Hall parameter calculated from electron parameters measured at 2 cm from the target.

5.5 Results

The ion rotation velocities measured and radial electric fields determined are plotted in Fig. 5.6 for different axial positions. Although the electron parameters and therefore the Hall parameter are not constant along the axis or radius of the beam, in our rough comparison of model with experiment, we assume that these parameters are in fact constant between the source and $z = 33$ cm and between $z = 33$ cm and the target.

The decrease in (the peak value of) the electric field between $z = 9$ cm and 33 cm is then consistent with an exponential decay with characteristic decay length, $\ell_{\parallel} = 50$ cm, for both experimental conditions. The decay lengths predicted by the Hall parameter from Thomson scattering (TS) measurements at 4 cm from the source are longer, 84 and 90 cm. The agreement is reasonable, especially considering that the electron temperature (and therefore Hall parameter and ℓ_{\parallel}) are expected to decline along the axis.

Over the second section of the beam, the rotation velocity measurements indicate

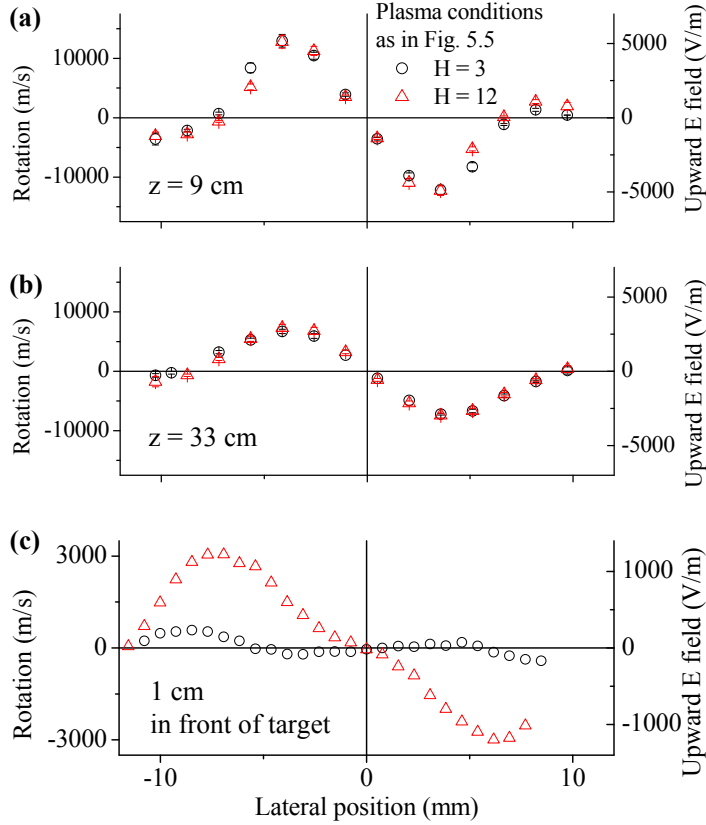


Figure 5.6: Rotation velocities for ‘H = 3’ and ‘H = 12’. Measurements made at (a) 9 cm downstream of the plasma source ($z = 9$ cm), (b) $z = 33$ cm and (c) 1 cm in front of the target. Positive rotation is defined as clockwise when looking from the source. Electric fields calculated from $v = \vec{E} \times \vec{B}/B^2$ can be read from the right hand axes of the graphs.

$\ell_{\parallel} = 10$ and 30 cm for the ‘H = 3’ and the ‘H = 12’ case respectively. Here predictions using the Hall parameter from TS measurements at 2 cm from the target give lower decay lengths, 6 and 20 cm respectively. That is reasonable given that the average electron temperature (and therefore also Hall parameter and ℓ_{\parallel}) along this section of the beam is expected to be higher than at the target. Overall, given the gradients in electron parameters, the agreements are reasonable.

Having determined that in both experimental conditions, a significant radial electric field is still present at the target, we deduce that electric current must flow through the target. The current through the target has been determined experimentally for a plasma

condition with Hall parameter 30 at 2 cm from the target. We measured the current over the shunt in the set up shown in Fig. 5.1. The current measured was 2 A. This measurement gives a lower limit on the real current through the target, since the current measured depends strongly on the radial position of the ceramic spacer and the exact radius at which the direction of the current changes. The current measured was independent of the resistance of the shunt, showing that it must be limited, not by the resistance of the target, but by the ion saturation current I_{sat} . Although the resistance of the target is orders of magnitude lower than the radial resistance of the plasma, total short-circuiting of the source current through the target is prevented by I_{sat} .

To estimate the sheath potentials, the voltage difference in front of the target is estimated from the rotation velocity measurements at 1 cm from the target. Using this measurement, the model predicts a sheath in the edge region of $\sim 2.5 \text{ kT}_e/e$ for the ‘H = 3’ case and 5-10 V for the ‘H = 12’ case. The sheath *profile* can also be estimated by integrating (fits of) the electric field profiles close to the target. The integral of the measurement at 1 cm from the target is shown in Fig. 5.7.

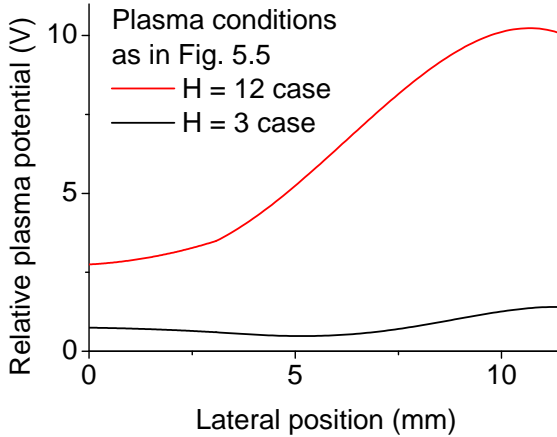


Figure 5.7: Sheath potential profiles made by integrating fits of the E field profiles at 1 cm from the target. Constants of integration are chosen such that the voltage at the central position is equal to $V_{\text{sheath}} = 2.5 \text{ kT}_e/e$.

Constants of integration are chosen such that $V = 2.5 \text{ kT}_e/e$ at $r = 0$. The sheath voltage at the edge of the plasma is about $\sim 10 \text{ V}$. Since we are measuring excited neutrals and not ions directly, dV/dr and therefore also the edge sheath voltage are probably underestimated. Interesting to note is that for the ‘H = 3’ case, the T_e dependence of the sheath potential can be observed in the centre (the potential decreases with radius). At the edge, the sheath potential increases with radius. It is higher at positions where the ion flux is lower and I_{sat} is reached more quickly. The T_e dependence of the central sheath potential can also be seen in the reversal of the electric field direction in the centre of the plasma in Fig. 5.6. We have also illustrated its effect schematically in the plasma

resistance limited case in Fig. 5.4.

To serve as a contrast with the results for a conducting target interfacing with the plasma, we also did experiments to confirm the expected effect when current is inhibited from flowing through the target between the inner and outer regions of the plasma. We used the ‘target probe experiment’ set up illustrated in Fig. 5.1. The floating potential of the inner target was measured to be -14 V and that of the outer target, -5 V. This potential difference is about the same as that predicted for the edge sheath voltage in the case of a conducting target, corresponding to the expectation illustrated in Fig. 5.4.

Finally, we studied the influence of radial electric fields on the ion flux in the centre of the target, to answer the question whether the large negative potentials here could impede the ion impingement. If the current through the target reaches the electron saturation current (the opposite of the ion saturation current, where all ions are repelled) in the centre, then the interpretation of plasma-wall interaction experiments could be influenced.

We consider two pieces of evidence. Firstly, in Fig. 5.8, we plot the I-V characteristic of the probe in the ‘target probe experiment’. This measurement indicates an ion satura-

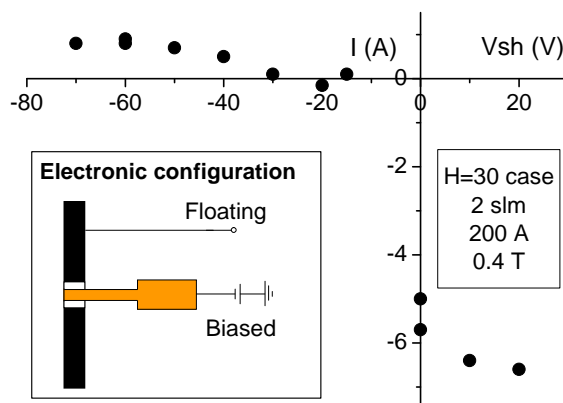


Figure 5.8: I-V characteristic for target probe experiment described in Fig. 5.1

tion current of approximately 1 A and an electron saturation current of about -7 A. We have seen earlier that when the inner and outer target regions are connected at the same plasma conditions, a current of 2 A flows (-2 A through the central sheath). It is clear from Fig. 5.8 that for this case, the current limitation ensures that the sheath voltage in the centre is negative (and that ions will not be repelled).

Secondly, we consider the carbon erosion profiles in Fig. 5.9. Surface profiles are displayed for carbon targets that have been exposed to two plasma conditions, the ‘ $H = 3$ ’ and ‘ $H = 12$ ’ cases. Electron temperature profiles near the target are shown for comparison. Spatial resolution of the measurement is $0.5 \mu\text{m}$ using a stylus of radius $12.5 \mu\text{m}$. The spikes observed in the figure do not represent noise, but real craters.

The maximum erosion depth roughly follows the electron temperature profiles and therefore in the central region also the sheath profile ($V_{sh} \sim 2.5 kT_e/e$). We believe this

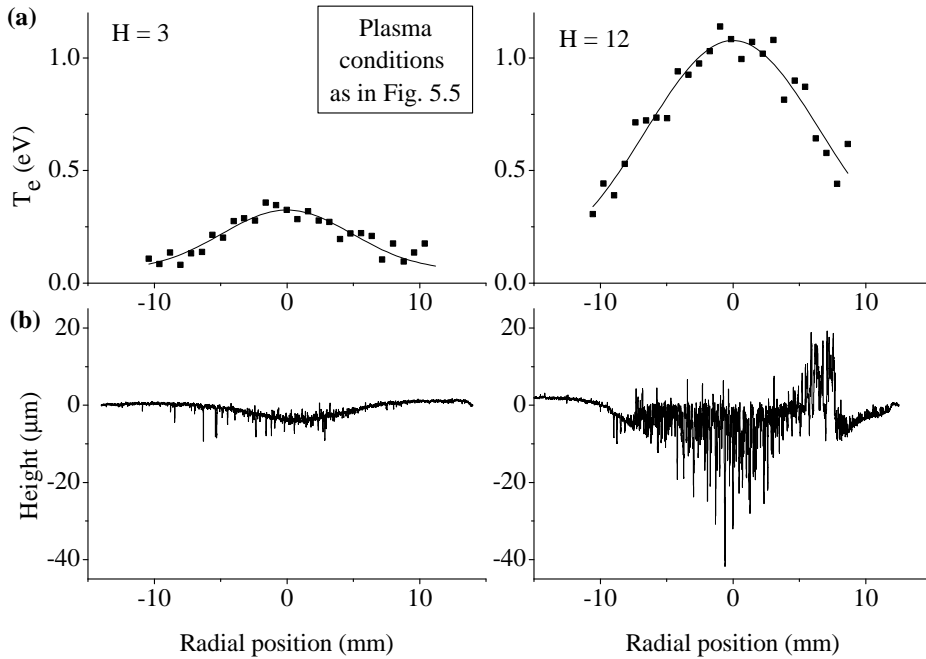


Figure 5.9: (a) Electron temperature profiles from Thomson scattering at 2 cm from the target, for the two main plasma conditions studied in this chapter. (b) Erosion profiles of carbon target samples exposed to the plasma conditions as shown. Profiles were measured ex-situ by means of a surface profilometer.

T_e dependence to be an energy threshold effect, observed in [15] and also predicted by molecular dynamics simulations [16] for an ion impact energy of < 5 V. Local hot spots may be the reason for local positions of net deposition. As seen in for example [17; 18], erosion is strongly dependent on surface temperature. The increased sheath voltage at the edge of the beam does not appear to lead to enhanced erosion. This could be due to the lower target temperature and lower ion flux density expected here. Larger effects on plasma surface interaction are expected in tokamaks where impurity sputtering is important.

Most importantly for the question at hand, the erosion profiles show that even though the central plasma potential is more negative for the ‘H = 12’ case, a larger local erosion is seen. This indicates that ions are not impeded from reaching the surface, concurring with the conclusion from the probe experiment. More experimental data is required to confirm that ions are not impeded from reaching the target for all relevant plasma conditions.

5.6 Conclusions

The current distribution and the plasma-wall sheath potential profile in a cylindrically symmetric, linear, magnetized divertor simulator have been modelled and studied experimentally. The ion saturation current at the target and the electric fields, both parallel and perpendicular to the magnetic field, all play an important role. It was found that a significant increase in the sheath potential can occur at the positive end of the target current if the plasma is sufficiently well magnetized. The sheath voltage increase can approach the total radial voltage difference available (i.e. much larger than $2.5 kT_e/e$) and may have a significant impact on plasma-wall interaction in tokamaks where impurity sputtering is important. For the conditions studied, the current through the target was confirmed to have negligible influence on the sheath voltage and the ion impingement at the target in the central plasma region.

5.7 Acknowledgements

We thank the MirrorLab Team from Forschungszentrum Jülich for use of and assistance with the surface profilometer.

References

- [1] K. Ikeda, “Progress in the ITER physics basis,” *Nucl. Fusion*, vol. 47, no. 6, 2007.
- [2] G. Janeschitz, K. Borrass, G. Federici, Y. Igitkhanov, A. Kukushkin, H. D. Pacher, G. W. Pacher, and M. Sugihara, “The ITER divertor concept,” *J. Nucl. Mater.*, vol. 220-222, pp. 73–88, 1995.
- [3] A. Kreter *et al.*, “Nonlinear impact of edge localized modes on carbon erosion in the divertor of the JET tokamak,” *Phys. Rev. Lett.*, vol. 102, no. 045007, 2009.
- [4] P. J. Harbour, “Current flow parallel to the field in a scrape-off layer,” *Contrib. Plasm. Phys.*, vol. 28, pp. 417–419, 1988.
- [5] G. M. Staebler and F. L. Hinton, “Currents in the scrape-off layer of diverted tokamaks,” *Nucl. Fusion*, vol. 29, no. 10, 1989.
- [6] R. Pitts, S. Alberti, P. Blanchard, J. Horacek, H. Reimerdesa, and P. C. Stangeby, “ELM driven divertor target currents on TCV,” *Nucl. Fusion*, vol. 43, no. 1145-1166, 2003.
- [7] A. Kallenbach *et al.*, “Divertor power and particle fluxes between and during type-I ELMs in the ASDEX upgrade,” *Nucl. Fusion*, vol. 48, no. 085008, 2008.
- [8] P. C. Stangeby, *The Plasma Boundary of Magnetic Fusion Devices*. Taylor & Francis Group, 2000.
- [9] K. Ida, S. Hidekuma, Y. Miura, T. Fujita, M. Mori, K. Hoshino, N. Suzuki, T. Yamauchi, and JFT-2M Group, “Edge electric-field profiles of H-mode plasmas in the JFT-2M tokamak,” *Phys. Rev. Lett.*, vol. 65, no. 11, 1990.
- [10] T. Lunt, G. Fussmann, and O. Waldmann, “Experimental investigation of the plasma-wall transition,” *Phys. Rev. Lett.*, vol. 100, no. 175004, 2008.
- [11] D. Nishijima, R. P. Doerner, M. J. Baldwin, A. Pospieszczyk, and A. Kreter, “Experimental determination of S/XB values of W I visible lines,” *Phys. Plasmas*, vol. 16, no. 122503, 2009.
- [12] M. Miyamoto *et al.*, “Observations of suppressed retention and blistering for tungsten exposed to deuterium-helium mixture plasmas,” *Nucl. Fusion*, vol. 49, no. 065035, 2009.
- [13] J. D. Huba, *NRL Plasma Formulary*. No. NRL/PU/6790–04-477, Naval Research Laboratory Washington DC, 2004.
- [14] L. Spitzer, “US atomic energy commission report,” tech. rep., 1951. NYO-993 (PM-S-1).

- [15] J. Westerhout *et al.*, “Chemical erosion of different carbon composites under ITER-relevant plasma conditions,” *Phys. Scripta*, vol. T138, no. 014017, 2009.
- [16] E. Salonen, K. Nordlund, and J. Keinonen, “Swift chemical sputtering of amorphous hydrogenated carbon,” *Phys. Rev. B*, vol. 63, no. 195415, 2001.
- [17] M. Balden and J. Roth, “New weight-loss measurements of the chemical erosion yields of carbon materials under hydrogen ion bombardment,” *J. Nucl. Mater.*, vol. 280, no. 39-44, 2000.
- [18] E. Vietzke and V. Phillips, “Hydrocarbon formation on carbon surfaces facing a hydrogen plasma,” *Fusion Technol.*, vol. 15, no. 1, pp. 108–117, 1989.

Chapter 6

Plasma acceleration on negative biasing: ion heating by reflected energetic neutrals

Abstract

This chapter reports on surface biasing experiments that affect upstream plasma parameters for high electron density conditions ($n_e \sim 10^{20} \text{ m}^{-3}$) in hydrogen and argon plasmas in contact with a copper target. Electron parameters were measured at three discrete positions in the pre-sheath region of the plasma-wall transition. As the target potential becomes more negative, measured electron temperatures rise by up to a factor of two and a half and integrated radial electron density profiles decrease by up to a factor of five. Given that the ion current to the target does not change with bias, we infer that the increase in the radial average of the axial velocity is also up to a factor of five. Observed changes are consistent with ion heating by energetic neutrals reflected from the target. Energy exchange between electrons and ions explain the electron temperature increase. The large change in axial velocity is partly explained by acceleration across the pre-sheath due to the rise in the sound velocity at the sheath edge, and partly by an increase in the pre-sheath length scale.

6.1 Introduction

Divertor biasing experiments are common in tokamaks and useful for the study of a variety of subjects [1; 2], from plasma mode control [3] to recycling and impurity control [4]. In linear tokamak divertor simulators, negative biasing of the target plate is used to control the incident ion energy or to determine the plasma flux (from the ion saturation current). Generally it is assumed that negative target biasing does not affect upstream plasma conditions. Potential applied to the target is shielded from the plasma on a length scale approximately equal to the Debye length. Applied voltage is thus incorporated into the so-called Debye sheath, which determines the ion energy at the target. Only a small part of this voltage leaks out of the sheath; enough to accelerate the ions to meet the Bohm criterion at the sheath edge.

Although voltage applied on a target cannot directly influence upstream plasma conditions, it may in fact do so via the reflection of energetic neutrals at the target following ion impingement. The energy of these neutrals increases with the ion impact energy. The electron density in most linear divertor simulators is so low that these reflected neutrals escape the beam without interacting with the plasma. For example, a paper on the linear plasma generator PISCES [5] reports constant plasma conditions as a function of negative target potential (20-90V) based on probe measurements and D_γ emission. A study on the linear plasma device NAGDIS-I [6] with a normalized sheath potential (eV_{sh}/kT_e) of up to 65 V reports that no plasma heating due to energetic neutral particles was observed.

Variations in plasma parameters *have* been observed in the pre-sheath region of the linear tokamak divertor simulator, Pilot-PSI. This plasma generator produces uniquely high plasma fluxes ($\sim 10^{24} \text{ m}^{-2}\text{s}^{-1}$) [7] and can produce ion densities that are high enough to ensure ion-neutral coupling. In this strongly coupled regime [8], neutrals reflected from the target share their energy with the plasma. This paper presents an experimental study of this effect and its consequences for the plasma velocity in the pre-sheath. We approach the study by measuring electron density and temperature with Thomson scattering in close proximity to the target as a function of target bias. We vary the fraction of neutrals that are reflected from the target by choosing different combinations of plasma discharge gas and target material such that the fraction of energy reflected from the target (the energy reflection coefficient) is varied.

The chapter is structured as follows. Sect. 6.2 defines two important phenomena that are instrumental to the effects studied in this chapter: the plasma-wall sheath and the pre-sheath. We outline the specific characteristics of these phenomena for the plasma-target interface in Pilot-PSI. Sect. 6.3 continues with a description of the experimental set-up. In Sect. 6.4, we outline the effect of target biasing on the ion energy at the target of Pilot-PSI. This is achieved via a study of the electric current configuration in the plasma. We come to the main results in Sect. 6.5 where measurements of several parameters are presented as a function of target bias: current to the target, electron temperature, electron density and axial neutral velocity and temperature. Our interpretation of the results is explained in Sect. 6.6 and simple ion energy balances are set up in Sect. 6.7 to assess this interpretation quantitatively. Finally, we discuss the results and conclude in sections 6.8 and 6.9.

6.2 The plasma-wall interface in Pilot-PSI

Changes in the energy of target reflected neutrals are caused by changes in the plasma-wall sheath on target biasing. Observed changes in plasma parameters are observed in the pre-sheath region further upstream. We begin this chapter by defining both of these elements of the plasma-wall interface - the sheath and pre-sheath - and by pointing out some of their properties in the unique plasma conditions of Pilot-PSI.

6.2.1 Debye sheath

When a surface interfaces with a plasma, a so-called Debye sheath will form at the surface. This is a region of net positive space charge that results when the surface becomes negatively charged by the very mobile electrons. This positive charge shields the potential of the target (even an applied potential) over a distance of the order of the Debye length, $\lambda_{\text{Debye}} = (\epsilon_0 k T_e / n_e e^2)^{1/2}$. For typical Pilot-PSI plasma conditions this distance is extremely short; only about 10 micrometers for an electrically floating target. For a negatively biased target, the sheath thickness can increase to several hundred micrometers. The sheath voltage for a hydrogen plasma at an electrically floating surface with $T_e = T_i$ is $V_{\text{sheath}} = 2.5 kT_e/e$ [9].

6.2.2 Pre-sheath

Shielding by the plasma-wall sheath is however not perfect. A small electric field penetrates into the plasma over the so-called pre-sheath. This is the approximately quasineutral region upstream of the sheath over which the plasma is accelerated to reach the sound velocity at the sheath edge (according to the Bohm criterion [9]). In some machines the pre-sheath length is determined by the re-ionization length, but the electron temperatures in Pilot-PSI are so low (< 3 eV) that re-ionization is negligible. In Pilot-PSI, the pre-sheath length is of the order of the mean free path for ion-neutral momentum exchange, λ_{in} [9; 10; 11]. This is of the order of 1 cm for both hydrogen and argon for the conditions studied in this chapter.

The electron density drop over the pre-sheath in Pilot-PSI is not the classic value of one half as holds for a static plasma. Since Pilot-PSI constitutes a high flux, streaming plasma, the most important consideration is flux conservation. Ignoring any recombination or ionization, the density drop across the pre-sheath can be calculated from:

$$\Gamma = n_0 v_0 = n_t c_s \quad (6.1)$$

giving:

$$\frac{n_t}{n_0} = \frac{v_0}{c_s} \quad (6.2)$$

where n_0 and v_0 are the electron density and velocity upstream of the pre-sheath, n_t is the density at the sheath edge and c_s is the sound velocity at the sheath edge. Typical upstream velocities are $0.2-0.5 \cdot c_s$, where c_s is the local sound velocity. Therefore, density

drops of up to a factor of five can be expected, or even more if the sound velocity increases towards the target. The voltage drop over the pre-sheath $V_{\text{pre-sheath}}$ is obtained from the Boltzmann equation [9] and given by:

$$V_{\text{pre-sheath}} = \frac{kT_e}{e} \ln \left(\frac{n_t}{n_0} \right) \quad (6.3)$$

Assuming a factor of five density drop over the pre-sheath, $V_{\text{pre-sheath}} = 1.6 kT_e/e$.

6.3 Experimental

Pilot-PSI is a magnetized linear plasma generator that simulates the plasma parameters expected in the divertor of ITER [12]. A schematic of the machine is shown in Fig. 6.1. The beam is typically ~ 1 cm in diameter and 0.5 m in length. The parameter range

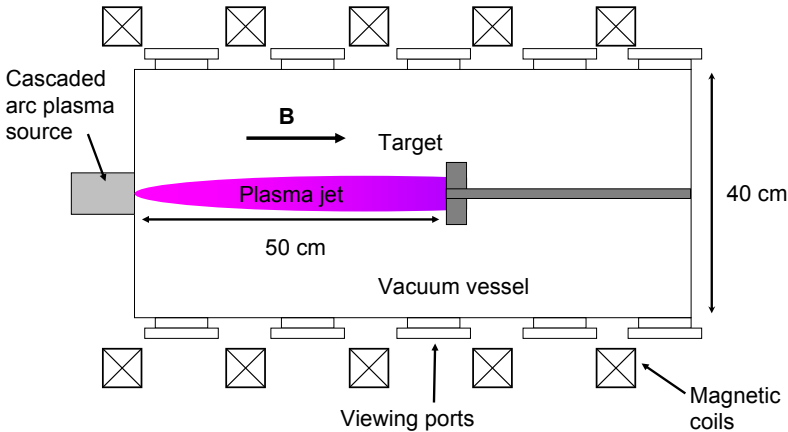


Figure 6.1: Schematic of plasma generator, Pilot-PSI

is defined by electron temperature $T_e = 0.3 - 3$ eV, electron density $n_e \approx 5 \cdot 10^{19} - 5 \cdot 10^{21} \text{ m}^{-3}$, neutral pressure of typically $P \approx 5$ Pa and magnetic field strength $B = 0.4 - 1.6$ T. These conditions yield an ion flux density of $\Gamma = 10^{23} - 10^{25} \text{ m}^{-2}\text{s}^{-1}$. Measurements presented in this chapter are performed in both argon and hydrogen plasma discharges.

In the experiments presented in this chapter, polished copper inserts of various thicknesses (30 mm in diameter) were mounted in a stainless steel, water-cooled target, thus varying the distance (6, 10 and 14 mm) between the target and the fixed position Thomson scattering diagnostic [13; 14; 15] (for T_e and n_e measurement). The magnetic field strength was in all cases 0.4 T.

The average ion energy impinging on the target was scanned by varying the target potential from floating potential (for Ar: 0 V, for H: -3 V) down to the most negative

bias obtainable before arcing is observed in the background gas surrounding the plasma beam. Electric current to the target was recorded across a shunt of $\sim 50 \mu\Omega$. We define the target bias in volts as the absolute value of the difference between the applied target potential and the target's floating potential.

Axial neutral velocity is determined by vector subtraction of Doppler shift measurements on the Balmer- α line taken from two different angles; one with a line of sight at 13 degrees to the normal of the target (almost axial) and one taken when viewing perpendicularly to the axis (i.e. parallel to the target). Spectra were analyzed with Voigt functions [16] (with the fine structure simulated by two Voigt functions shifted with respect to one another as explained in Chap. 3) and wavelength calibrated with spectra from a hydrogen lamp.

Analysis of spectra measured parallel to the target at a 6 mm distance yield the rotation velocity and temperature of excited neutrals near the target. Assuming ideal coupling between excited neutrals and ions, the rotation velocity is equal to the ion $\vec{E} \times \vec{B}$ drift, from which the radial electric field profile is calculated. Its dependency on the target bias is studied in Sect. 6.4 and used to evaluate the radial sheath voltage profile.

The experimental parameters for the hydrogen discharge were a gas flow of 1.5 slm and discharge current of 200 A. Two argon discharges were performed with different particles fluxes. Experimental parameters were 0.7 slm, 120 A for the low flux case and 2 slm and 150 A for the high flux case.

6.4 Study of electric current configuration as a function of bias

A key parameter in the study presented in this chapter is the sheath voltage at the target, since it determines the ion energy. The sheath voltage at the target in Pilot-PSI is not a simple function of the target bias. The relationship is complicated by the flow of electric current through the target and by radial plasma parameter gradients. In this chapter we present a consideration of the sheath voltage profile as a function of target bias. The consideration is supported by radial electric fields inferred from experimentally determined rotation velocities for the hydrogen plasma conditions studied in this work.

We saw in Chap. 5 that for a well magnetized plasma beam impinging on an electrically floating target in Pilot-PSI, an electric field exists at the target directed perpendicularly to the magnetic field. This electric field causes a current to flow through the target and the sheath potential at the edge of the beam (the ion end of the current path) to increase. Note that although the target is electrically floating in the sense that the net current to the target is zero, locally the target pulls current and is therefore not at floating potential. The sheath voltage at the edge of the target is approximately equal to the voltage difference across the beam from edge to centre. Intuitively, this can be understood because the path through the plasma and through the target form a parallel electric circuit and the voltage drop over both branches must be equal.

Furthermore in Chap. 5 we saw that the radial plasma-wall sheath voltage profile can

be approximated by integrating an electric field profile that is measured very close to the target. Constants of integration are chosen such that the sheath voltage in the centre is equal to the natural sheath voltage $2.5 \text{ kT}_e/e$ (since at the electron end of the current path the sheath potential is approximately equal to that for a floating surface).

A picture of the sheath voltage behaviour as a function of bias has been obtained for the hydrogen discharge conditions studied in this chapter. The radial electric field profiles used are estimated by measuring the rotation velocity of excited neutral atoms that are strongly coupled to the ions that have an $\vec{E} \times \vec{B}$ rotation drift. The electric field profiles obtained are underestimations of the real values, since the coupling between ions and neutral atoms is not perfect and the ion velocity may be somewhat limited by viscosity. However, the measurements show a strong change in the electric field configuration with bias, which allows us to obtain a qualitative description of the changes that occur. The rotation velocities and inferred radial electric field profiles at 6 mm from the target are plotted in Fig. 6.2a.

The radial potential profile is obtained from $V = -\int E \, dr$, with the constant of integration set by the sheath voltage in the centre of the target, $2.5 \text{ kT}_e/e$. The result is shown in Fig. 6.2b, where the integral is estimated by means of a Riemann sum. Note that after the (total) ion saturation current is reached, we change the constant of integration. This is because ion saturation has now also been reached in the centre of the beam and the sheath voltage can no longer be approximated by the case of a floating target. Since the current through the plasma beam to the target is now limited, further changes in voltage applied at the target cannot be supported in the beam and will be taken up in the plasma-wall sheath. We therefore assume a linear increase of the sheath potential with target bias after the ion saturation current has been reached. It is interesting to note that the position of maximum gradient in the sheath potential moves inwards as the target potential becomes more negative, up until the (total) ion saturation current is reached. This effect is even more evident in the maxima of the electric field profiles in Fig. 6.2a. We can deduce from this observed behaviour that as the target is biased, ion saturation is first reached at the edge of the target and this condition moves progressively inwards towards the centre of the beam. This is to be expected for two reasons. Firstly, the bias difference between upstream plasma and target is largest at the edge of the beam. Secondly, the ion flux is lower towards the edges of the beam. This effect is expected to be less pronounced in argon, since the radial potential gradients will be smaller (this is due to the lower Hall parameter as explained in Chap. 5).

We conclude that just like the electron density and electron temperature, the ion energy at the target is a radially varying parameter. In the hydrogen discharges it is typically 10 V larger at the edge of the beam than in the centre.

6.5 Study of plasma parameters as a function of bias

Here we present the main results of this chapter; an experimental study of the plasma parameters measured in the pre-sheath as a function of target bias. An overview of the measurement series performed is given in Fig. 6.3 in the form of I-V characteristics of the

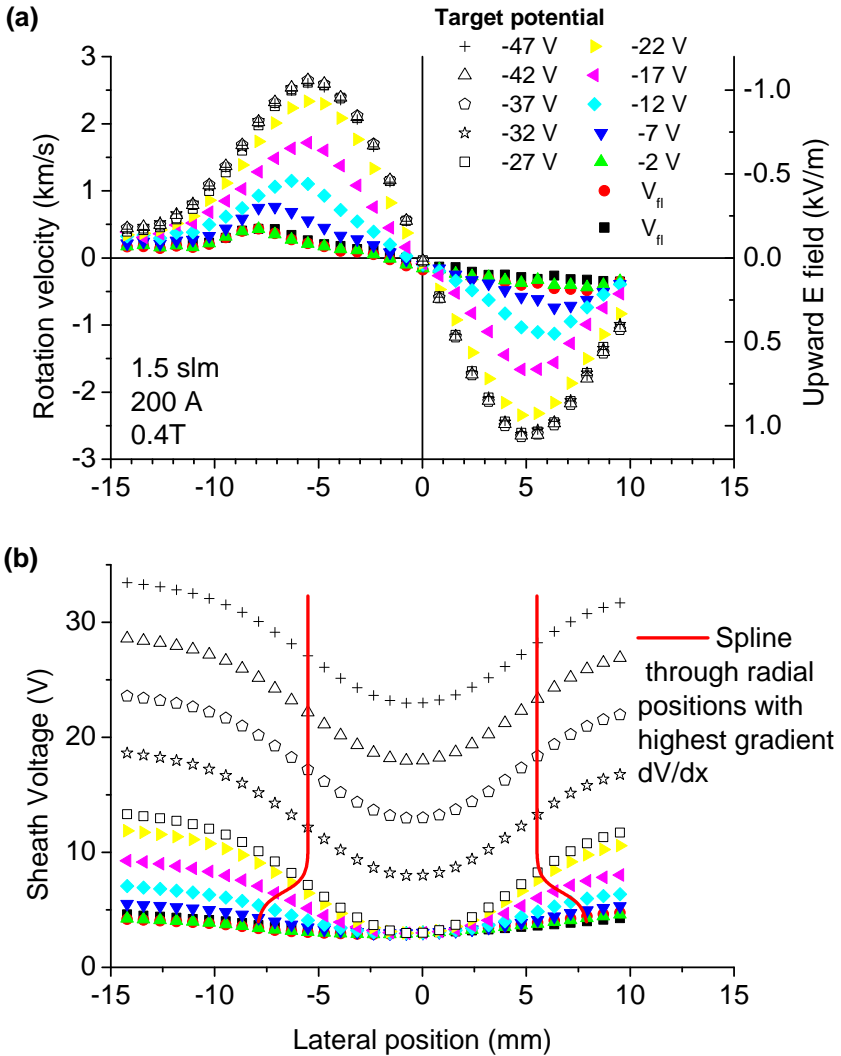


Figure 6.2: (a) Rotation velocity of excited neutral atoms at 6 mm from the target as a function of target bias. The rotation velocities are used to calculate radial electric field values under the assumption of perfect ion-neutral coupling and zero viscosity. (b) Radial sheath potential profiles calculated via Riemann sums of the estimated radial electric field profiles. The offset at $r = 0$ is assumed to be $2.5 kT_e/e$ until I_{sat} is reached and thereafter to increase linearly with target bias. A spline is drawn through the positions of maximum gradient, emphasizing the inward movement of ion saturation. Note that edge sheath voltages are underestimated. Assuming that the increase in edge sheath voltage is equal to the increase in target bias, the edge sheath voltage for bias 47 V should in fact be equal to 51 V.

target for each set of plasma source parameters. The target bias - defined as the absolute

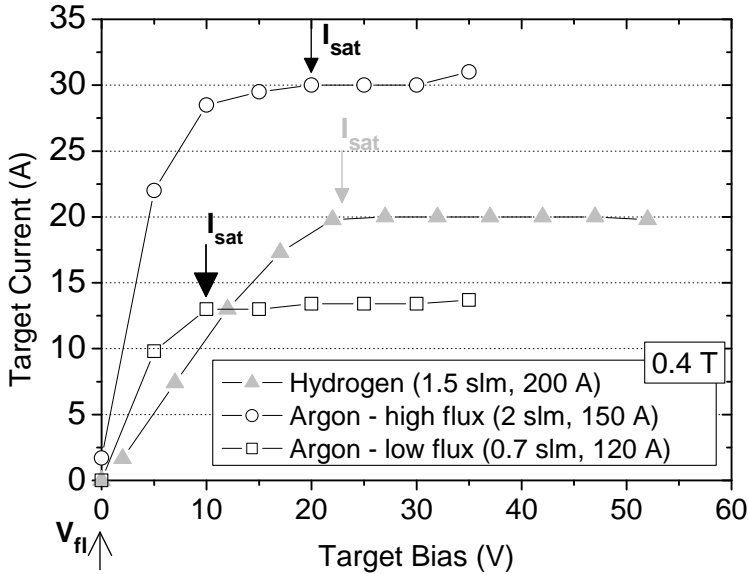


Figure 6.3: Overview of target bias scans. Current to the target is plotted. Target bias is defined as the absolute difference between the target potential and floating potential.

difference between the target potential and the floating potential - is increased up until the ion saturation current (I_{sat}) is reached. Beyond this point the current to the target is constant, with small variations due to instability of the plasma. We are particularly interested in the measurements at I_{sat} , since for this condition, Ohmic dissipation can be ruled out as a cause of variation in plasma parameters. The target bias at which I_{sat} is reached is indicated in the graphs in this section. Two different working gases are used. In this way, we vary the energy reflection coefficient; the fraction of target deposited energy that is converted into kinetic energy of target reflected neutral particles. For the relevant ion energies, the energy reflection coefficient is 0.6-0.8 [17] for hydrogen on a copper target, and 0.05 [18] for argon on copper. The saturation current is equal to the total ion flux and is of course larger for the high flux case than for the low flux case.

The electron density was monitored during these scans with Thomson scattering at three distances, z , from the target. The peak values are plotted in Fig. 6.4. The electron density drops towards the target by up to a factor of five (for the argon, low flux case) and the decrease is stronger for positions closer to the target. Notable is that the decrease continues after I_{sat} has been reached. Since the ion flux to the target was shown to be constant in Fig. 6.3, the decrease in density must be due to acceleration. We can therefore calculate the average axial velocity \bar{v}_{ax} , at each axial position using the equation:

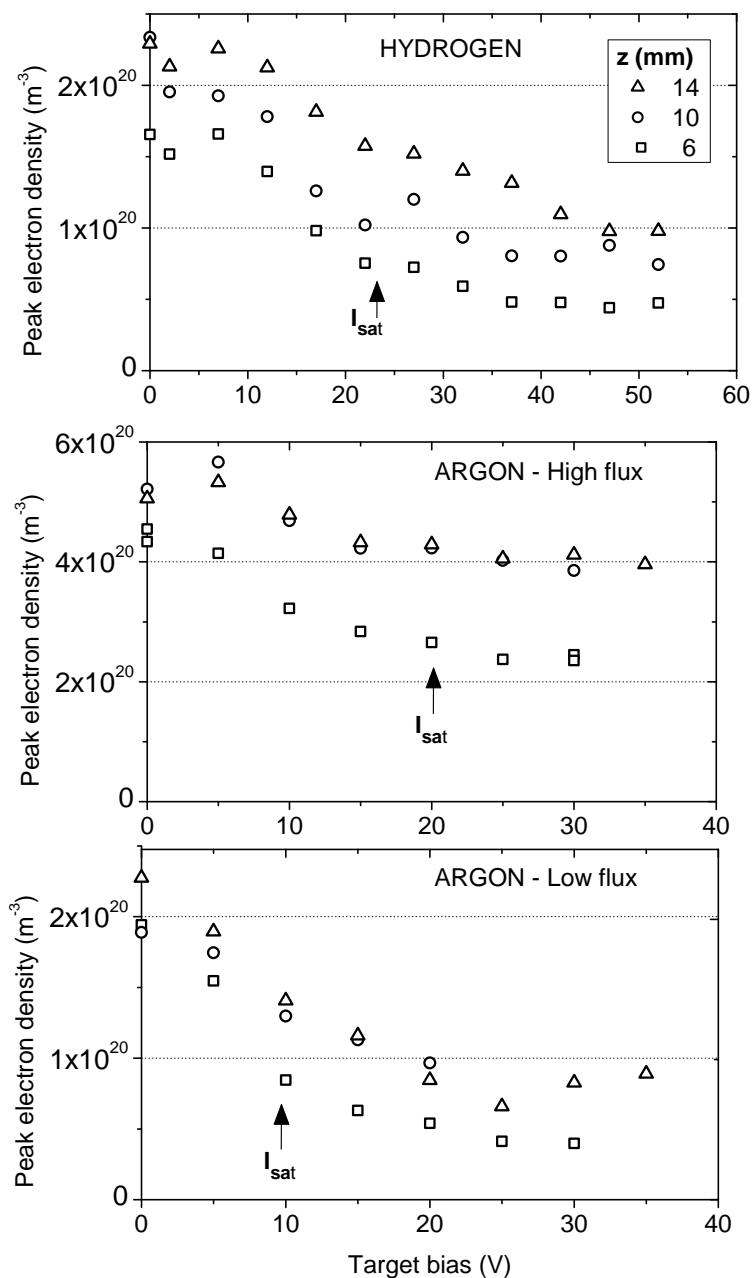


Figure 6.4: Peak electron density vs target bias at distances $z = 6, 10$ and 14 mm from the target. Decrease in electron density continues after the saturation current (I_{sat}) has been reached. Source parameters as in Fig. 6.3.

$$I_{\text{sat}} = e\Gamma = e \int n_e(r)v_{\text{ax}}(r)2\pi r dr \quad (6.4)$$

which gives

$$\bar{v}_{\text{ax}} = \frac{I_{\text{sat}}}{e \int n_e(r)2\pi r dr} \quad (6.5)$$

This equation assumes flux conservation between the position of the Thomson scattering diagnostic and the target, supported by the observation that the ion saturation current is constant. Measured electron density profiles $n_e(r)$ were fitted with a Gaussian function before integration. The results for \bar{v}_{ax} are plotted in Fig. 6.5 together with an indication of the value of the sound speed at the maximum electron temperature condition measured. The following expression was used to calculate the sound speed,

$$c_s = \sqrt{\frac{k(T_e + \gamma T_i)}{m}} \quad (6.6)$$

with the following assumptions: The maximum possible value is chosen for the specific heat ratio - $\gamma = 3$ as holds in the sheath - to ensure an upper limit on the indicated sound velocity. The electron and ion temperatures T_e and T_i are assumed equal to one another and m is equal to the atomic mass of the species considered.

In all cases, the velocity increases as a function of target bias. The velocities are larger closer to the target and the acceleration from $z = 14$ mm to 6 mm increases with target bias. For argon, the plasma velocity is around 0.5-1 km/s at floating potential. For the high flux case it accelerates up to 2.3 km/s at 6 mm from the target (an increase by a factor of 2.6). For the low flux case this acceleration is considerably more, up to 5.8 km/s (a factor of 4.7). For the hydrogen case the plasma at 6 mm accelerates from 8 km/s up to 24 km/s (a factor of 3). In all cases, acceleration is observed beyond the achievement of ion saturation. Eventually the value of the velocity becomes constant or even starts to decrease. Notable is the large relative increase in velocity, by a factor of as much as 5 for the argon low flux case at 6 mm from the target. Also notable is that in some cases, the velocity is larger than the calculated sound velocity (given the assumption of $T_e = T_i$).

In Fig. 6.6, the axial ion velocity for the hydrogen discharge was also measured indirectly via excited neutrals which are coupled to the plasma ions via charge exchange. These measurements confirm that the axial velocity increases as a function of target bias, and that the increase continues beyond ion saturation. The values of the velocity are of course lower due to the long line of sight of the measurements (several tens of centimeters). Also, the emission decreases strongly towards the target and is therefore most sensitive for the lower upstream velocity. These measurements therefore give us a good estimation of the axial velocity upstream of the pre-sheath, $v_0 \approx 3$ km/s. The asymmetry in the profiles is due to slight inaccuracies in the determination of the centre of the beam and the magnification of the optical set-up before vector subtraction of axial and radial Doppler shift measurements.

Analysis of optical emission spectra measured parallel to the target (at 6 mm distance) in the hydrogen discharge are analyzed with a Voigt function yielding not only a

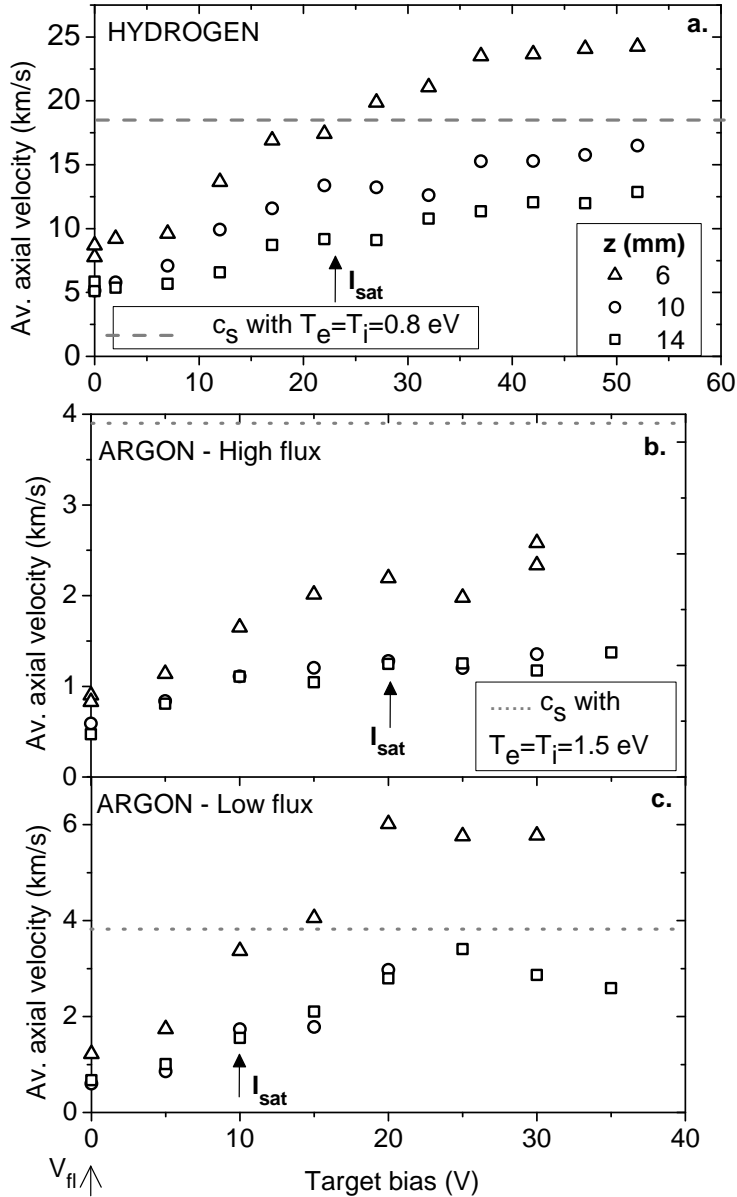


Figure 6.5: Average axial velocities calculated using electron density measurements in combination with I_{sat} measurements. The magnitude of the sound velocity at the maximum electron temperature measured is indicated for comparison. The bias at which I_{sat} is reached is indicated. Source parameters as in Fig. 6.3.

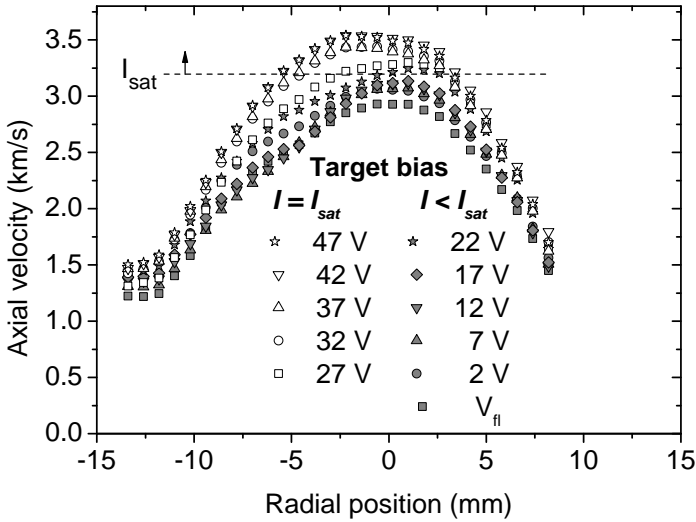


Figure 6.6: Radial profiles of axial velocity determined from optical emission spectroscopy on the H- α line. Acceleration is clearly observed even after the ion saturation current has been reached. Source parameters as in Fig. 6.3.

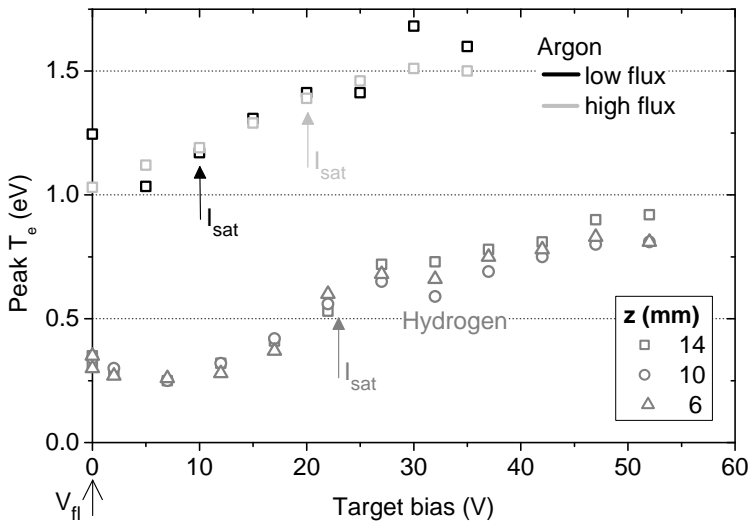


Figure 6.7: Peak electron temperature as a function of target bias. In all cases, T_e clearly continues to rise after I_{sat} has been reached. Measurements for argon at $z = 6$ mm and 10 mm have been removed for clarity. Source parameters as in Fig. 6.3.

Doppler shift but also a temperature from the Doppler broadening and an electron density from the Stark broadening. Unfortunately, for this measurement set, the two broadening mechanisms could not be unambiguously separated from one another to give reliable temperature measurements. The analyses have however given us an indication that the background neutral temperature is less than or equal to 1 eV. They appear to show a general trend increasing from about 0.3 eV to 0.7 eV over the target bias scan.

The electron temperature for hydrogen shows similar behaviour to that of the background neutrals. Peak electron temperatures for all plasma conditions are plotted in Fig. 6.7. The axial temperature gradient is approximately zero in all cases, so for clarity, only one axial position is shown for the argon cases. For all three target bias scans, the electron temperature is clearly seen to rise even after ion saturation has been reached. Interestingly, its behaviour is almost identical for both argon discharges. It rises by up to a factor of 1.5 for the argon measurements and 3.7 for hydrogen. There is no significant axial temperature change over the three measurement positions. The dip in the electron temperature at low bias is explained by changes in the current configuration. When the target is at floating potential, the current to the target in the centre of the beam is negative (carried by the electrons). As the target is biased, the strength of the current decreases and goes through zero before becoming positive and eventually reaching the ion saturation current. When the current is zero, the power input due to Ohmic dissipation is also zero, corresponding to the temperature dip at ≈ 5 V. Examples of electron temperature and density profiles are shown in Fig. 6.8. At ion saturation, the full width half maximum (FWHM) of all density profiles is approximately constant.

6.6 Interpretation: plasma heating by energetic target reflected neutrals

The experiments reported demonstrate a significant change in plasma parameters in the pre-sheath on target biasing. The most obvious change is a decrease in the electron density. Given the constant ion flux to the target, this indicates plasma acceleration. Also, a temperature rise is observed in the electron population, and also in the background neutral population. Significant is that these changes continue even after the ion saturation current has been reached (and there is no additional heat input due to Ohmic dissipation).

The second significant observation is that the inferred axial velocities rise to above the value of the sound velocity that is calculated assuming $T_e = T_i$ and $\gamma = 3$. Supersonic velocities are unexpected since we know of no mechanism that could accelerate the plasma to above $M = 1$ at the sheath edge. There is no temperature gradient towards the target [9] and no constriction in the magnetic field, which could produce supersonic velocities in a manner analogous to a Laval nozzle [19].

One possible explanation for the apparent supersonic velocities is residual ionization in the background gas. It is possible that velocities are overestimations if the Gaussian fits of the electron density do not accurately describe the residual electron density outside of the beam. For example, if the electron density in the region $r = 1.5 - 5$ cm outside the

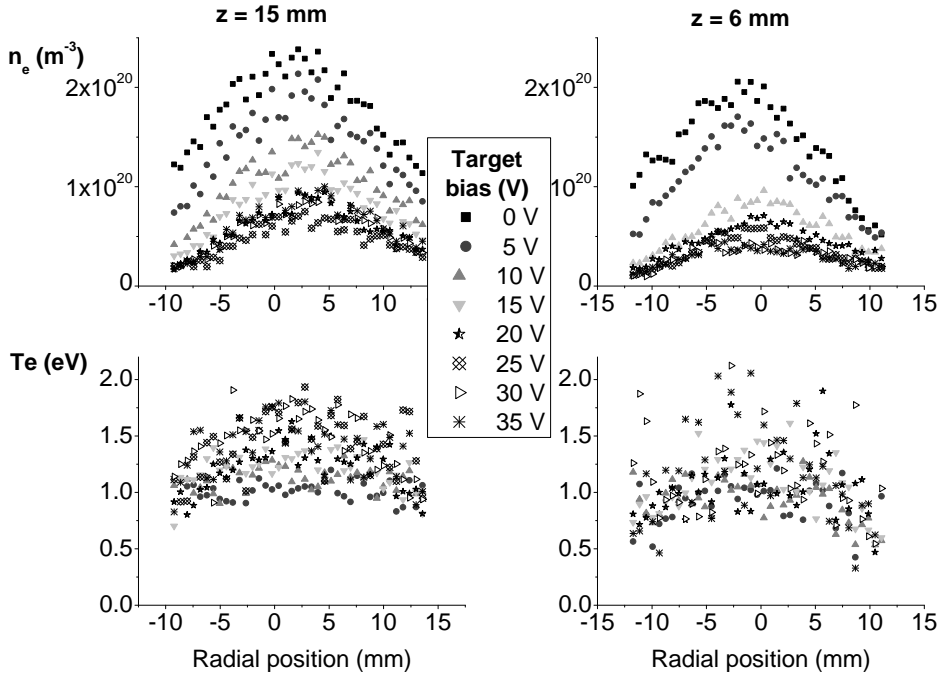


Figure 6.8: Examples of electron density and temperature profiles as a function of bias. The profiles shown are for the low flux argon case at 6 mm and 15 mm from the target.

beam, was on average $1.5 \cdot 10^{18} \text{ m}^{-3}$ higher than estimated, then the axial velocities in Fig. 6.5c (argon - low flux) would in fact be lower than the indicated sound speed.

However, this cannot explain the large *rise* in the velocity (up to a factor of five for the low flux argon case). Since the beam width is constant after ion saturation has been reached, it is very unlikely that the density of any extra residual charge outside the beam is a strong function of target bias (otherwise we would see the effect at the edges of the plasma profiles).

A plausible explanation of the velocity rise can be found in consideration of the Bohm criterion [20]. This criterion states that the plasma must accelerate over the pre-sheath to reach at least the sound velocity at the sheath edge. Therefore, if the sound velocity at the sheath edge were to increase significantly, this would cause an increase in the acceleration across the pre-sheath. A rise in this sound velocity can be caused by a rise in the electron temperature and/or in the ion temperature at the sheath edge. In addition, if the length-scale of this pre-sheath acceleration were to increase, an additional velocity increase would be observed on measurement at a fixed axial position, as depicted schematically in Fig. 6.9.

Since the observed velocity increase continues at ion saturation, temperature increase

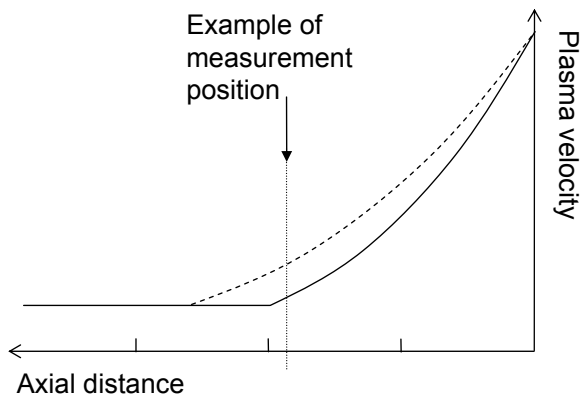


Figure 6.9: Schematic showing how change in pre-sheath length can cause an increase in the measured velocity, independent of the increase in the sound velocity.

due to Ohmic heating is not sufficient to explain the observations. We do however expect another significant heating mechanism near the target of Pilot-PSI: ion heating by target reflected neutrals. Ions are accelerated across the plasma-wall sheath and neutralized before hitting the target and being reflected back into the plasma with energy, $R_E \cdot V_{sheath}$. R_E is the energy reflection coefficient [9] and V_{sheath} is the sheath voltage, the value of which is significantly larger when the target is biased than when it is floating. After reflection, these neutrals interact with other particles. The interaction with the largest cross-section is charge exchange with ions. The mean free path for this process ranges from a few millimeters to a few centimeters for the conditions considered. These distances are in the same order as the dimension of the beam, so energy coupling is expected. Thermal energy is also expected to be at least partially transferred to electrons via Coulomb collisions.

As mentioned earlier, electron heating has indeed been observed. At 6 mm from the target, a factor of 1.5 increase in electron temperature was observed with target biasing in argon and an increase of up to a factor of 3.7 was seen in hydrogen. We expect the temperature increase to be larger for the ions, since this is the species that receives primary heating. We also expect the ion temperature to be even higher closer to the target, since heating by target reflected neutrals must decrease exponentially from the target into the plasma.

The pre-sheath length scale can also be affected by interaction of ions with target reflected neutrals. This length scale is approximately equal to the mean free path for ion-neutral charge-exchange, λ_{in} . As the target bias is increased, the reflected neutrals become more and more energetic, the cross-section for charge exchange decreases and λ_{in} increases. For argon, we calculate an increase in this length of about a factor of 1.3 over the target bias scan. For hydrogen the increase is by about a factor of 1.9. As explained above, this will give an additional increase in the inferred axial velocity.

6.7 Quantitative evaluation of the effect of target reflected neutrals

In this section, we give a rough quantitative evaluation of the above interpretation based on calculations of the plasma, ion and electron energy balances. These calculations assume that radial gradients are zero for the quantities; electron temperature, electron density, axial velocity and sheath voltage. In Sect. 6.4 we saw that in hydrogen, the sheath voltage is typically 10 V larger at the edges of the beam than in the centre, and Fig. 6.8 shows that the electron densities and temperatures are in fact larger in the centre of the beam. Comparison between experiment and calculations can therefore not be expected to give exact agreement. We can however use such a comparison to give a rough quantitative evaluation of our hypothesis. For the calculations, we have used peak values of radial profiles of electron temperature and density and maximum values of the radial sheath voltage profile.

6.7.1 Power balance as a function of axial distance

Our approach is to first set up a very simple power balance as a function of distance, z , from the target. The aim is to evaluate whether the energy transferred from target reflected neutrals to ions is enough to cause the observed acceleration. We assume a single temperature $\hat{T} = \hat{T}_i = \hat{T}_e$ (in eV), power input from energetic target reflected neutrals and power loss due to convection. By assuming a relationship between the axial velocity $v(z)$ and the temperature $\hat{T}(z)$, we then obtain estimates for axial plasma temperature and velocity profiles.

Power input

We first require an expression for the deposited power in the plasma from target reflected neutrals. We expect this quantity, $P(z)$ [eV/m/s], to be an exponential function decaying from the target into the plasma.

$$P(z) = F(0)e^{-z/\lambda_{ni}} \quad (6.7)$$

λ_{ni} is the mean free path for charge exchange between target reflected neutrals and plasma ions. We calculate it with $\lambda_{ni}=1/n_e\sigma_{ni}$, where n_e is the average axial electron density for a given bias from Fig. 6.4 and σ_{ni} is the cross-section for charge exchange. $F(0)$ can be calculated since we know that the integral of $P(z)$ from the target ($z=0$) to infinity is the total energy input into the plasma:

$$\int_0^\infty P(z)dz = \int_0^\infty F(0)e^{-z/\lambda_{ni}}dz = \alpha R_E V_{sh} \phi \quad (6.8)$$

where α is the fraction of target reflected neutrals that couple with the plasma, R_E is the energy reflection coefficient, V_{sh} is the sheath voltage and ϕ is the ion flux to the target, in particles per second. Solving this integral gives:

$$F(0) = \frac{\alpha R_E V_{sh} \phi}{\lambda_{ni}} \quad (6.9)$$

Therefore:

$$P(z) = \frac{\alpha R_E V_{sh} \phi}{\lambda_{ni}} e^{-z/\lambda_{ni}} \quad (6.10)$$

Power balance

The power balance is as follows:

$$\begin{aligned} \left(\frac{5}{2} \hat{T}(z) + \frac{mv(z)^2}{2e} \right) \phi &= \left(\frac{5}{2} \hat{T}_{far} + \frac{mv_{far}^2}{2e} \right) \phi \\ &+ \int_z^\infty \frac{\alpha R_E V_{sh} \phi}{\lambda_{ni}} e^{-z/\lambda_{ni}} dz \end{aligned} \quad (6.11)$$

The units of each term are eV/s. The subscript ‘far’ indicates a parameter far from the target (in principle at infinity). Note that ϕ cancels out, giving:

$$\frac{5}{2} \hat{T}(z) + \frac{mv(z)^2}{2e} = \frac{5}{2} \hat{T}_{far} + \frac{mv_{far}^2}{2e} + \alpha R_E V_{sh} e^{-z/\lambda_{ni}} \quad (6.12)$$

We then assume an (arbitrary) relationship between $\hat{T}(z)$ and $v(z)$, that satisfies $v(0) = c_s(0)$ and $v(\infty) = v_{far}$ and that changes with approximately the same characteristic length as the heat input, λ_{ni} . To simplify the substitution into equation 6.12, we define $v(z)^2$ instead of $v(z)$. The exponential decay is therefore set equal to $\exp(-2z/\lambda_{ni})$ instead of $\exp(-z/\lambda_{ni})$. The following expression satisfies the above requirements:

$$v(z)^2 = (c_s(z)^2 - v_{far}^2) e^{-2z/\lambda_{ni}} + v_{far}^2 \quad (6.13)$$

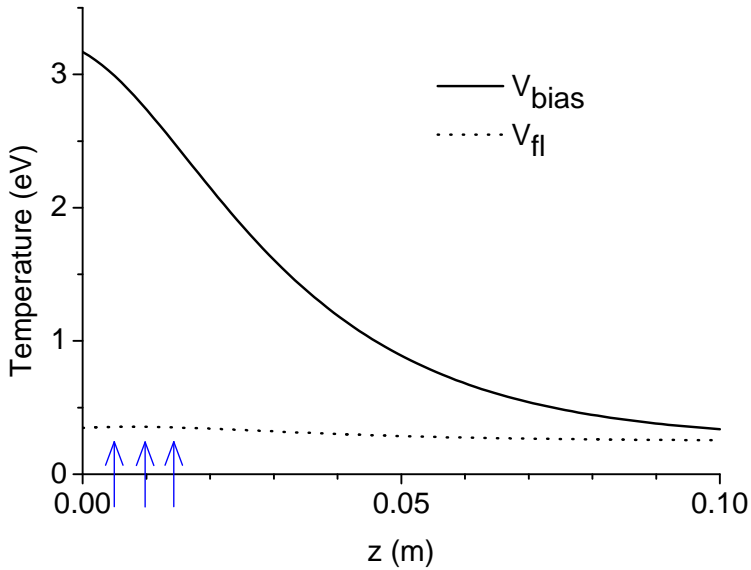
with

$$c_s(z) = \sqrt{\frac{e(\hat{T}_e + \gamma \hat{T}_i)}{m_i}} = \sqrt{\frac{4e\hat{T}}{m_i}} \quad (6.14)$$

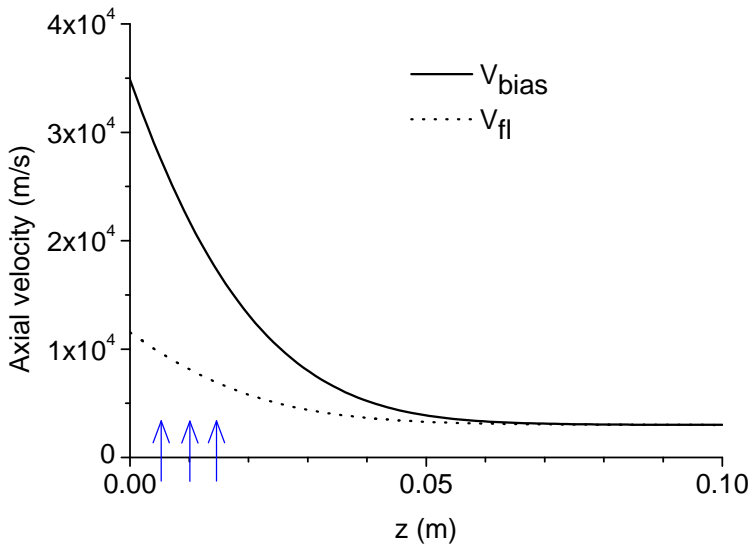
We then obtain:

$$\hat{T}(z) = \frac{\frac{5}{2} \hat{T}_{far} + \frac{mv_{far}^2}{2e} e^{-2z/\lambda_{ni}} + \alpha R_E V_{sh} e^{-z/\lambda_{ni}}}{\frac{5}{2} + \frac{3}{2} e^{-2z/\lambda_{ni}}} \quad (6.15)$$

In Figs. 6.10 and 6.11, the temperature from equation 6.15 and the axial velocity from equation 6.13 are plotted as a function of axial distance for the values in Table 6.1. Calculations are shown for both a floating and a biased target. The calculations are performed using reflection coefficients from the literature. At 30 V, $R_E = 0.05$ [18] for argon reflecting from a copper surface and at 50 V, $R_E = 0.8$ [17] for hydrogen on reflecting from copper.

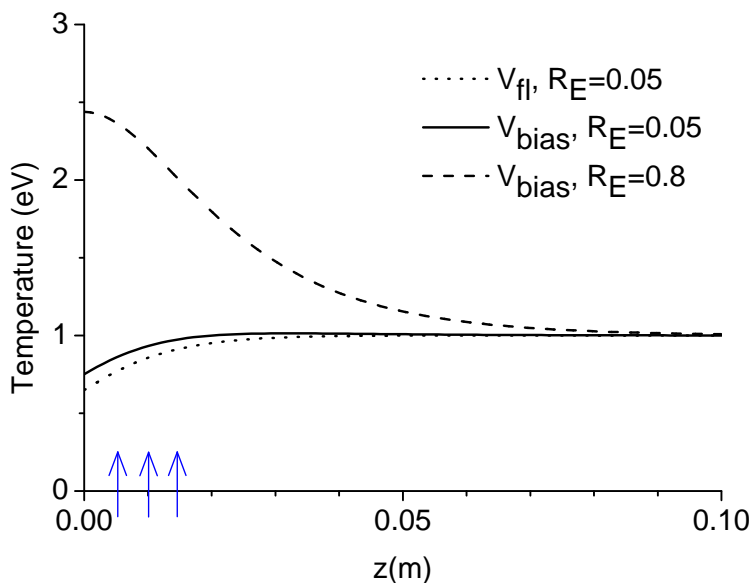


(a) Temperature

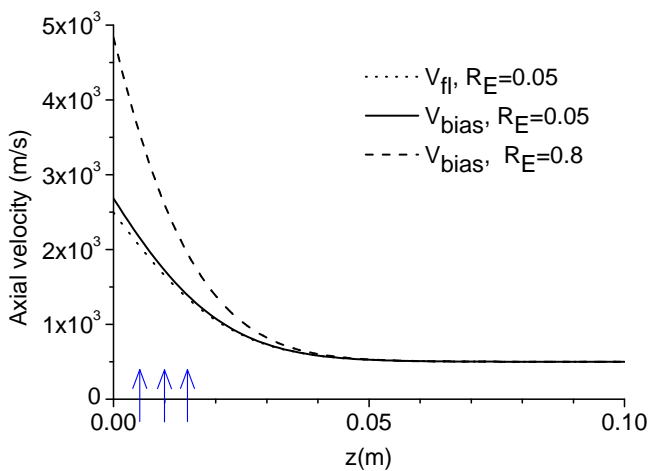


(b) Axial velocity

Figure 6.10: Calculated temperature and axial velocity as a function of axial distance for hydrogen plasma on a copper target. Positions at which measurements were made are indicated with arrows. The reflection coefficient is $R_E = 0.8$.



(a) Temperature



(b) Axial velocity

Figure 6.11: Calculated temperature and axial velocity as a function of axial distance for argon plasma on a copper target. Positions at which measurements were made are indicated with arrows. Calculations are for the literature value of $R_E = 0.05$ and for a much higher value, $R_E = 0.8$.

	Hydrogen	Argon (low flux)	Argon (high flux)
\hat{T}_{far}	0.25 eV	1.0 eV	1.0 eV
v_{far}	3000 m/s	500 m/s	500 m/s
$V_{sh,bias}$	50 V	30 V	30 V
$V_{sh,fl}$	3 V	3 V	3 V
α	0.3	0.3	0.3
R_E	0.8	0.05	0.05
$\lambda_{ni,bias}$	2.5 cm	1.72 cm	0.33 cm
$\lambda_{ni,fl}$	0.58 cm	0.47 cm	0.2 cm

Table 6.1: Data taken from measurements and literature for a hydrogen/argon plasma impinging on a copper target. The appropriate collision times are calculated from data measured at the highest possible target bias at 6 mm from the target.

Inspection of Fig. 6.11 clearly shows that the literature value for the energy reflection coefficient, $R_E = 0.05$, for argon on copper is insufficient to explain the increase in axial velocity by a factor of 2.6 and 4.7 for the two different plasma conditions. However, there may be factors that enhance the reflection coefficient, such as the high incident particle and heat fluxes, the target temperature, or the presence of impurities in the plasma and/or target. We therefore also calculate the effect of target reflected neutrals assuming a much higher energy reflection coefficient. We choose here arbitrarily the same reflection coefficient as for hydrogen impinging on copper, $R_E = 0.8$.

Under this assumption, the calculated axial velocity increases by a factor of two on target biasing. Another factor of two could be gained in the increase in axial velocity at a single axial position, due to an increase in the pre-sheath length. We therefore propose the hypothesis that the energy reflection coefficient for argon on copper is greatly enhanced with respect to the literature value. More research is required to determine a viable mechanism.

For hydrogen, the axial velocity calculations agree surprisingly well with experimentally determined velocities, considering the simplicity of the model. Energy from target reflected neutrals is clearly sufficient to explain the increase in experimental axial velocities by a factor of three.

Notable in these calculations is that the calculated temperature \hat{T} required to obtain agreement between calculated and experimental velocities is higher than the measured electron temperatures. This can be understood if there is a separation between the ion and electron temperatures. We evaluate this possibility in the next section, with a power balance that includes more terms than in this section, but does not consider spatial dependence.

6.7.2 Evaluation of separation of ion and electron temperatures

In this section, we set up a balance for the *change* in stored energy, w due to target reflected neutrals for both the electrons and the ions. Units are eV/m³/s. The goal is to evaluate whether, as suggested in the previous section, the ion temperature can be larger than the electron temperature. The balance includes heating by target reflected neutrals (Q), energy loss via convection with confinement time $1/\nu_C$, ion-electron energy transfer with time constant $1/\nu_{ie}$, and energy loss by heat conduction for electrons (the latter is negligible for ions). This gives:

$$\frac{d}{dt}(w_i) = Q - \frac{5}{2}n\Delta\hat{T}_i\nu_C - n(\Delta\hat{T}_i - \Delta\hat{T}_e)\nu_{ie} = 0 \quad (6.16)$$

$$\frac{d}{dt}(w_e) = -\frac{5}{2}n\Delta\hat{T}_e\nu_C + n(\Delta\hat{T}_i - \Delta\hat{T}_e)\nu_{ie} - K_e \frac{2\Delta\hat{T}_e}{e\lambda_{ni}^2} = 0 \quad (6.17)$$

The changes in stored energy are calculated using average changes in $\Delta\hat{T}_i$ and $\Delta\hat{T}_e$ in the volume $A \cdot \lambda_{ni}$, where A is the cross-section of the beam. We assume that without heating, the electrons and ions are at the same starting temperature so that $\hat{T}_i = \hat{T}_{far} + \Delta\hat{T}_i$ and $\hat{T}_e = \hat{T}_{far} + \Delta\hat{T}_e$. ν_C is estimated as $\nu_C = v_{ax}/\lambda_{ni}$ where v_{ax} is the average axial velocity at given bias in Fig. 6.5. The last term in equation 6.17 is an approximation based on the expression for electron conduction [9]:

$$q_{e,cond} = -K_e \frac{d\hat{T}_e}{dz} W/m^2 \quad (6.18)$$

with

$$K_e = \frac{30692 \hat{T}_e^{5/2}}{\ln\Lambda} \quad (6.19)$$

We approximate this loss as:

$$q_{e,cond} = -K_e \frac{2\Delta\hat{T}_e}{e\lambda_{ni}^2} eV/m^3/s \quad (6.20)$$

We thus assume that without the extra heating source (from target reflected neutrals), the axial electron temperature gradient is zero. We assume that when heating is added, the temperature gradient over the distance, λ_{ni} within which this heating is distributed is constant. The change in temperature is assumed to be $2\Delta\hat{T}_e$ at the target, and zero at distance λ_{ni} . We ignore the increase in the parameter K_e with electron temperature. By defining:

$$q = \frac{Q}{n} eV/s \quad (6.21)$$

and

$$C = \frac{2K_e}{ne\lambda_{ni}^2} s^{-1} \quad (6.22)$$

we obtain the simpler expressions:

$$q - \frac{5}{2}\Delta\hat{T}_i\nu_C - \Delta\hat{T}_i\nu_{ie} + \Delta\hat{T}_e\nu_{ie} = 0 \quad (6.23)$$

and

$$-\frac{5}{2}\Delta\hat{T}_e\nu_C + \Delta\hat{T}_i\nu_{ie} - \Delta\hat{T}_e\nu_{ie} - C\Delta\hat{T}_e = 0 \quad (6.24)$$

From equation 6.24, we then find that:

$$\frac{\Delta\hat{T}_e}{\Delta\hat{T}_i} = \frac{\nu_{ie}}{\frac{5}{2}\nu_C + \nu_{ie} + C} \quad (6.25)$$

from which we obtain expressions for $\Delta\hat{T}_i$ and $\Delta\hat{T}_e$:

$$\Delta\hat{T}_i = \frac{q(\frac{5}{2}\nu_C + \nu_{ie} + C)}{(\frac{5}{2}\nu_C + \nu_{ie})(\frac{5}{2}\nu_C + \nu_{ie} + C) - \nu_{ie}^2} \quad (6.26)$$

$$\Delta\hat{T}_e = \frac{q\nu_{ie}}{(\frac{5}{2}\nu_C + \nu_{ie})(\frac{5}{2}\nu_C + \nu_{ie} + C) - \nu_{ie}^2} \quad (6.27)$$

With $Q = \alpha R_E V_{sh} \Gamma / \lambda_{ni}$ (all energy is assumed to be deposited within distance, λ_{ni} from the target) and n , \hat{T}_e , ν and Γ taken from measurements at the highest bias and at 6 mm from the target, we can calculate $\Delta\hat{T}_e$ and $\Delta\hat{T}_i$. The values of ν_C , ν_{ie} , C and q are calculated using the axial average of parameters measured at the highest bias and are tabulated in Table 6.2. Since there are many assumptions in the calculation of the

	Hydrogen	Argon (low flux)	Argon (high flux)
ν_{ie}	$4.5 \cdot 10^6 \text{ s}^{-1}$	$4.22 \cdot 10^4 \text{ s}^{-1}$	$2.17 \cdot 10^5 \text{ s}^{-1}$
ν_C	$9.92 \cdot 10^5 \text{ s}^{-1}$	$3.198 \cdot 10^5 \text{ s}^{-1}$	$5.62 \cdot 10^5 \text{ s}^{-1}$
C	$6.87 \cdot 10^5 \text{ s}^{-1}$	$7.245 \cdot 10^6 \text{ s}^{-1}$	$3.825 \cdot 10^7 \text{ s}^{-1}$
q	$7.128 \cdot 10^7 \cdot \alpha R_E \text{ eV s}^{-1}$	$1.695 \cdot 10^7 \cdot \alpha R_E \text{ eV s}^{-1}$	$2.58 \cdot 10^7 \cdot \alpha R_E \text{ eV s}^{-1}$

Table 6.2: The values of the ν_C , ν_{ie} , C and q calculated using the axial average of parameters measured at the highest bias for each of the three experimental conditions.

value of C , we test the sensitivity of the calculations to C by plotting $\Delta\hat{T}_e$ and $\Delta\hat{T}_i$ as a function of C in Fig. 6.12. The calculated values of C are indicated with arrows. The fact that Fig. 6.12 predicts a higher average change in the ion temperature than Figs. 6.11 and 6.10 is due to the fact that conversion of thermal energy into axial velocity is ignored.

These calculations verify that, despite the high electron density and thus fast electron-ion thermalization, the ions close to the target will be hotter than the electrons. For hydrogen, the energy balance predicts a 1.7 times larger rise in the ion temperature than in the electron temperature. For argon the rise predicted is 100 times larger for ions than for electrons. However, based on the observation that on target biasing, the electron temperature rises by 0.5 eV for all measurement conditions, it is likely that we have overestimated the losses due to heat conduction for argon and underestimated these losses for hydrogen.

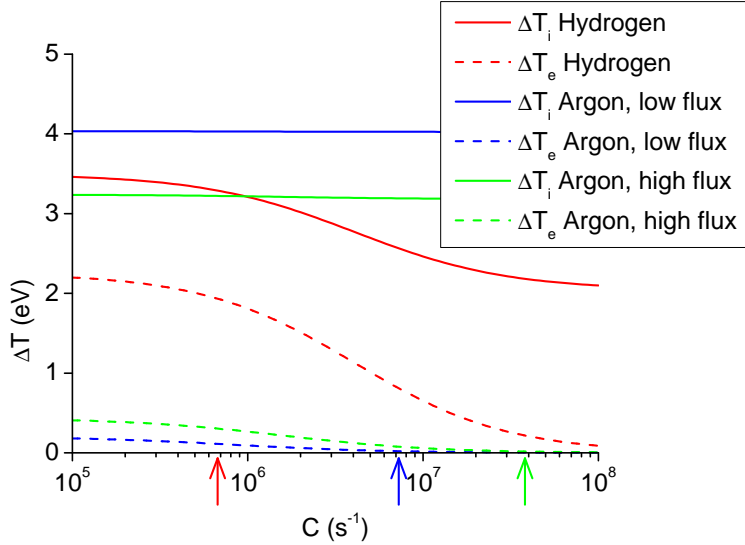


Figure 6.12: The average change in ion temperature $\Delta\hat{T}_i$ and electron temperature $\Delta\hat{T}_e$ caused by target reflected neutrals in the region close to the target under the assumption $R_E = 0.8$. Variables are plotted as a function of C , the inverse time constant for heat loss by electron heat conduction. Arrows indicate the calculated value of C for each experimental condition.

6.8 Discussion: comparison of measurements with calculations

Given the strong radial gradients in experimental parameters, the one dimensional model in the previous section cannot be expected to predict the experiments perfectly. The accuracy is however good enough to show us whether the energy coupled from target reflected neutrals to the plasma is in the right ball park to explain the observed acceleration.

For hydrogen plasma impinging on copper, the agreement in axial velocity between experiment and calculations is good. We conclude that energy from reflected neutrals is large enough to explain the factor of three observed increase in the axial velocity. This acceleration does require a larger plasma temperature increase than the observed electron temperature increase, however this makes sense when we calculate the separation of the ion and electron temperatures. Calculations predict that on target biasing, the ion temperature rise is 1.7 times larger than that of the electron temperature. This difference may be even larger if we have underestimated the electron energy losses.

Calculations of the argon on copper experiments using the literature value for the energy reflection coefficient predict less than a 10% rise in axial velocity. This is clearly insufficient to explain the velocities inferred from measurements of up to a factor of 4.7. Instead of immediately rejecting our hypothesis based on this observation, we consid-

ered the possibility that the energy reflection coefficient is significantly enhanced for the plasma-wall system in these experiments with respect to the literature value. We therefore repeated the calculations assuming a significantly higher (arbitrary) value of the energy reflection coefficient, $R_E = 0.8$. This predicts a velocity increase of a factor of 2. A further factor of 2.35 increase in the velocity at a single axial position could reasonably be attributed to a change in the length scale of the acceleration in combination with additional heat input terms that have been ignored.

To evaluate the hypothesis of a higher energy reflection coefficient, extra experiments and calculations are required. Extra terms in the energy balance such as viscous heating and Ohmic heating should be calculated. We suggest extra experiments to explore the behaviour of the energy reflection coefficient of argon on copper. In these experiments, special care should be taken to ensure the purity of the plasma and of the target material. Scans in the plasma flux and target temperature during measurements may shed some light on a mechanism that could increase the reflection coefficient with respect to literature values.

6.9 Conclusion

Despite the well-known Debye shielding of a target potential from an upstream plasma, we have measured changes in plasma parameters in the pre-sheath region as a function of negative target bias. In hydrogen and argon plasmas impinging on a copper target, measurements indicate an increase in the electron temperature and in the axial plasma velocity as a function of bias. For the hydrogen case, calculations show that the observations are consistent with our hypothesis of changes due to heating by target reflected neutrals. For argon impinging on copper, the literature value for the energy reflection coefficient, 0.05, is not high enough to explain the observed changes with this mechanism. A significantly enhanced energy reflection coefficient of 0.8 could however explain the observations. Further experiments are required to understand and evaluate a possible mechanism for an increase in this energy reflection coefficient.

The observations described in this chapter have not been reported in other linear divertor simulators. This is most likely due to the uniquely high (ITER relevant) ion densities that are produced in Pilot-PSI which result in a large charge exchange rate and therefore good coupling of the ions with neutrals reflected from the target. It is an important result which is also expected to be found in the divertor of ITER in regions where sheath voltages are large. Such plasma rarefaction is difficult to measure so close to the divertor plates in a tokamak. The effect does however deserve consideration since it is important for the calculation of reaction rates close to the surface of the divertor.

References

- [1] R. R. Weynants and G. Van Oost, "Edge biasing in tokamaks," *Plasma Phys. Controlled Fusion*, vol. 35, pp. B177–B189, 1993.
- [2] A. Boileau, "Tokamak plasma biasing," *Nucl. Fusion*, vol. 33, no. 1, 1993.
- [3] T. E. Stringer, "Explanation of the L-H mode transition induced by applied voltage," *Nucl. Fusion*, vol. 33, no. 9, 1993.
- [4] B. Terreault *et al.*, "Improvements in recycling and impurity control obtained by divertor biasing," *Nucl. Fusion*, vol. 34, no. 6, p. 777, 1994.
- [5] D. G. Whyte, G. R. Tynan, R. P. Doerner, and J. N. Brooks, "Investigation of carbon chemical erosion with increasing plasma flux and density," *Nucl. Fusion*, vol. 41, no. 1, pp. 47–62, 2001.
- [6] S. Masuzaki, N. Ohno, and S. Takamura, "Experimental study on plasma heat flow to plasma-facing materials," *J. Nucl. Mater.*, vol. 223, pp. 286–293, 1995.
- [7] G. J. van Rooij *et al.*, "Extreme hydrogen plasma densities achieved in a linear plasma generator," *Appl. Phys. Lett.*, vol. 90, p. 121501, 2007.
- [8] A. W. Kleyn, N. J. Lopes Cardozo, and U. Samm, "Plasma-surface interaction in the context of ITER," *Phys. Chem. Chem. Phys.*, vol. 8, pp. 1761–1774, 2006.
- [9] P. C. Stangeby, *The Plasma Boundary of Magnetic Fusion Devices*. Taylor & Francis Group, 2000.
- [10] K.-U. Riemann, "The Bohm criterion and sheath formation," *J. Phys. D*, vol. 24, pp. 493–518, 1991.
- [11] L. Oksuz, M. A. Khedr, and N. Hershkowitz, "Laser induced fluorescence of argon ions in a plasma presheath," *Phys. Plasmas*, vol. 8, no. 5, pp. 1729–1733, 2001.
- [12] G. Federici *et al.*, "Key ITER plasma edge and plasma-material interaction issues," *J. Nucl. Mater.*, vol. 313-316, pp. 11–22, 2003.
- [13] H. J. van der Meiden *et al.*, "High sensitivity imaging Thomson scattering for low temperature plasma," *Rev. Sci. Instrum.*, vol. 79, p. 013505, 2008.
- [14] G. J. van Rooij *et al.*, "Thomson scattering at Pilot-PSI and Magnum-PSI," *Plasma Phys. Controlled Fusion*, vol. 51, p. 124037, 2009.
- [15] M. H. J. 't Hoen, "Supersonic flow near a negatively biased target in a linear plasma generator," Masters Thesis, Universiteit Utrecht, 2009.
- [16] B. H. Armstrong, "Spectrum line profiles: the Voigt function," *J. Quant. Spectrosc. Radiat. Transfer*, vol. 7, pp. 61–88, 1967.

- [17] D. Reiter, "Surface interaction database." http://www.eirene.de/html/surface_data.html.
- [18] H. L. Bay, H. F. Winters, H. J. Coufal, and W. Eckstein, "Energy transfer to a copper surface by low energy noble gas ion bombardment," *Appl. Phys. A*, vol. A55, pp. 274–278, 1992.
- [19] D. D. Ryutov, "Kinetic theory analysis of sheaths and shocks," *Contrib. Plasm. Phys.*, vol. 36, no. 2/3, pp. 207–219, 1996.
- [20] D. Bohm, *The Characteristics of Electric Discharges in Magnetic Fields*. New York: McGraw-Hill, 1949. Chap. 3.

Chapter 7

Discussion

7.1 Conclusions

The main research questions of this thesis are:

1. When electric fields are applied or come into existence in a magnetized plasma near a conducting target, how will the electric current be distributed, and how will the plasma-wall sheaths be affected?
2. How will the plasma parameters in a high electron density plasma in front of a conducting target be affected by target reflected neutrals when the target plate is biased?

In order to address these research question, we first tackled two sub-questions

- a. How can we non-intrusively measure the electric fields and neutral particle densities in Pilot-PSI?
- b. What is the origin of the radial electric fields in Pilot-PSI and how can we manipulate them?

We first developed a non-intrusive diagnostic based on optical emission spectroscopy to probe the radial electric fields in Pilot-PSI via the $\vec{E} \times \vec{B}$ drift. A second diagnostic based on absorption spectroscopy returned comparable values for the radial electric field. We found that the rotation at 4 cm from the source was approximately that which could be expected from an electric field corresponding to the voltage drop between the last two plates in the cascaded arc source divided by the radius of the beam. This voltage drop increases with magnetic field strength and with nozzle diameter, parameters that increase the effective radial resistance. Simple modelling showed that the radial electric field penetrated into the vessel, decaying exponentially into the vessel with parallel length scale ℓ_{\parallel} , related to the characteristic width of the beam ℓ_{\perp} as $\ell_{\parallel}/\ell_{\perp} = (1/\xi)\sqrt{\sigma_{\parallel}/\sigma_{\perp}} = 0.36\sqrt{1 + H^2}$ where σ_{\parallel} and σ_{\perp} are the conductivities of the plasma parallel and perpendicular to the magnetic field. H is the Hall parameter, a measure of the magnetization of the plasma, defined as the ratio between the gyration frequency and collisional frequency of a plasma species. The current penetration thus increases with magnetization, H . For the conditions studied in Pilot-PSI, the relevant Hall parameter was that of the electrons, H_e , since elec-

trons are more mobile than ions perpendicular to the magnetic field. H_e increases linearly with magnetic field, is inversely proportional to the electron density and increases with electron temperature to the power $3/2$.

We also developed a method to measure neutral densities using absorption spectroscopy. An important result is the high ionization degree in the beam centre close to the plasma source ($> 85\%$). Another is the strong increase in neutral atomic density as a function of electron density. This is attributed to an increase in residence time of neutral atoms in the plasma, especially inside the channel of the plasma source, due to the increased strength of ion-neutral coupling.

Armed with knowledge about electric field behaviour in Pilot-PSI and two non-intrusive diagnostic techniques, we could then commence study of the first research question. We started by generalizing understanding obtained about electric field behaviour in Pilot-PSI. An electric field and corresponding electric current perpendicular to a magnetic field will decay exponentially along the magnetic field lines with a length scale dependent on the Hall parameter. Secondly, we confirmed that when this electric field decay is interrupted by a conducting surface, an electric current will flow through the surface. Also, in areas where the current to the surface is positive, the impact energy of ions will be affected. The plasma-wall sheath voltage (see Chap. 6.2) in this region will increase to approximately the value of the voltage difference across the surface. This can be avoided by prohibiting current flow in the surface with an insulating insert.

We approached the second research question, the effect of target reflected neutrals on plasma parameters with detailed measurements in both hydrogen and argon plasma impinging on a copper target. Radial electron density and temperature profiles were measured at three axial positions in the last 2 cm in front of the target while the energy of reflected neutrals was scanned. This was performed by scanning the impact ion energy via target biasing. An increase in the electron temperature with target bias was observed. Also the electron density was observed to decrease, while the plasma flux to the target was constant. This implies extra axial plasma acceleration over the pre-sheath (see Sect. 6.2). The results are consistent with heating of the ions by target reflected neutral particles and secondary heating of electrons by ion-electron heat exchange. Such an increase in ion and electron temperature must also raise the sound velocity at the sheath edge. The plasma must thus undergo extra acceleration to meet the boundary condition set by the Bohm criterion, which states that the plasma velocity must be equal to or larger than the sound velocity at the entrance to the sheath.

We could therefore conclude that electric fields and neutral particles affect the plasma-wall transition in tokamak divertors. Ion energies at divertor surfaces may be increased by electric fields and reflected neutral particles may affect plasma boundary conditions and thereby also plasma parameters close to divertor plates. Plasma surface interaction processes, and thereby surface material lifetimes will be affected. We will return to these issues in sections 7.3 and 7.4, but first we discuss the impact of this research for further studies on Pilot-PSI.

7.2 Implications for further research on Pilot-PSI

The research program of Pilot-PSI constitutes a component of plasma-wall interaction or tokamak divertor relevant studies, and a component of understanding the plasma itself. The latter category of experiments is important and forms a prerequisite for understanding the former.

In this thesis, the tools have been developed with which the ion energy profile at the target can be approximated for plasma-wall interaction experiments in Pilot-PSI. The ion energy is a critical parameter for the study of plasma-wall interaction mechanisms relevant for fusion. It has also confirmed that the large negative potentials in the centre of the Pilot-PSI beam do not necessarily impede ions from reaching the surface. For the conditions observed in this thesis, ions are not repelled by the central plasma-wall sheath.

Another important conclusion of this thesis with implications for Pilot-PSI is the result that the plasma beam is not transparent for neutral atoms. This has been shown in Chap. 4, where we saw a dramatic increase in the neutral atomic density with electron density, in a scan from low electron density up to ITER divertor relevant parameters. The interaction of neutral atoms with the plasma is also dramatically demonstrated in Chap. 6 where this interaction is the most likely cause of the observed acceleration. We have thereby demonstrated that Pilot-PSI is the first linear divertor simulator with such a high electron densities that consideration of interactions with neutral particles becomes crucial.

Other important results for Pilot-PSI were obtained from the extra quantities that could be measured with the diagnostics developed to measure electric fields and atomic neutral densities. The quantities include: ion temperature, the optical thickness of the Lyman- α line, dissociation degree in the vessel and penetration of rovibrational molecules into the plasma beam. All of these quantities are important ingredients for plasma modeling [1; 2; 3], required for improved understanding of the Pilot-PSI plasma.

Particularly interesting results include the higher ion temperature than electron temperature that is observed near the plasma source at high magnetic fields in a hydrogen discharge. It would be interesting to confirm this result using Collective Thomson Scattering [4]. The optical thickness of the Lyman- α line (~ 0.6 at typical conditions near the source) is a significant result for collisional radiative modelling [5; 6; 7]. The observed penetration of rovibrationally excited molecules into only the outer few millimeters of the beam is significant since it is similar to the case expected in ITER where rovibrationally excited molecules will be dissociated a few millimeters from the divertor plates.

One particularly important parameter that has been estimated is the ionization degree in the beam. At 4 cm from the plasma source exit and standard plasma conditions this was found to be $> 85\%$. From preliminary measurements close to the target even higher ionization degrees are expected at this position [8]. Further measurements as a function of radius should be performed to confirm this. The ionization degree is important to know for the interpretation of plasma-wall interaction experiments [9; 10; 11; 12]. If the neutral fraction of the flux is low enough its effect can be ignored.

7.3 Implications for tokamaks

The observed plasma-wall sheath voltage increase in Pilot-PSI due to an electric field across the target has parallels in existing literature in theory and experiment. For example, a similar effect is well-known from the double Langmuir probe diagnostic [13]. In tokamaks, a voltage difference between the inner and outer divertor legs had been shown [14; 15] to cause a current to flow through the divertor structure and increase the plasma-wall voltage at the ion end of the current path. Theory on this effect in tokamaks [16; 17] focuses largely on the case in which the voltage difference is due to a temperature difference (thermoelectric currents).

The important contribution of the experiments in Pilot-PSI to the literature is their focus on the existence of a voltage difference across a single conducting surface in contact with a magnetized plasma. The experiments imitate the radial electric field in the scrape of layer of a tokamak (the outer layer of plasma in a tokamak that hits the divertor plates) which gives a voltage difference across a single divertor plate in the divertor. The effect of this voltage difference on the plasma-wall sheath is difficult to measure directly in a tokamak divertor because of the multitude of variables at work, the complicated geometry that limits diagnostic access and the difficulty of interpretation of electric probe measurements in a magnetic field.

The effect does however deserve consideration in tokamak divertors. Radial electric fields can be large. For example, in the JFT-2M tokamak [18], radial electric fields of up to 15 kV/m are observed close to the divertor plates, three times larger than the largest fields observed in this thesis. Other references give measured and simulated electric fields of 5-10 kV/m ([19] Asdex Upgrade and [20] DIII-D and Mast).

The induced sheath voltages are of consequence since they determine the impingement energy of ions at the divertor plates. Especially heavy impurity ions that are present in tokamak divertors can cause significant damage to and lifetime reduction of divertor plates via sputtering [21; 22]. Experiments in this thesis have shown that an increase in sheath energy can be avoided by insulation of sections of a conducting target from one another.

We have also shown in this thesis that at the high plasma fluxes expected in ITER, an increase in sheath voltage can have more far reaching consequences than only an increase in the ion impact energy. Via target biasing experiments, we have shown that such changes in the sheath voltage can cause extra plasma acceleration across the pre-sheath. The rarefaction involved means an accompanying decrease in the electron density. These are significant results because knowledge of ion velocity and density in the vicinity of tokamak divertor plates is required for the calculation of reaction rates of particles that are reflected or desorbed from the target. These rates determine important features of plasma-wall transition. One example is the length that molecules can penetrate into the plasma before dissociating. Another concerns the mean free paths of various species compared to the characteristic size of the plasma. This determines whether the particles are trapped in the beam and can for example determine whether eroded divertor material is redeposited on the divertor plates.

The acceleration observed in Pilot-PSI is not expected to be observed in present day

tokamak divertors. These divertor plasmas are transparent for the energetic target reflected neutrals which we believe to be responsible. The width of the scrape-off layer is typically a few centimeters wide and the mean free paths for neutrals are much longer. The effects are however expected in ITER.

7.4 Implications for ITER and beyond

Due to the higher electron densities expected in the ITER divertor (and in other reactor-grade fusion devices), energetic neutrals reflected from the divertor plates will share their energy with the plasma. This thesis predicts that extra pre-sheath acceleration will therefore occur in areas of these divertors where the sheath voltage is enhanced. Modelling of plasma-wall interaction for ITER relevant conditions should take the associated change in plasma parameters into account.

Extrapolation of the results of sheath enhancement in Pilot-PSI to the ITER divertor is not straight forward. Differences in the conditions include the geometry, the angle of interception of the magnetic field lines with the divertor plates and temperature and density gradients. However, several lessons learned from this research can be applied directly to the future ITER divertor. We have demonstrated that at the high fluxes expected in the ITER divertor, significant electric currents can be expected to flow through conducting divertor plates. The high resistivity of the plasma will also ensure that significant voltage differences can be supported both parallel and perpendicular to the magnetic field lines. A simple consideration of electric currents in the divertor therefore requires inclusion of both.

References

- [1] M. Baeva, W. J. Goedheer, N. J. Lopes Cardozo, and D. Reiter, “B2-EIRENE simulation of plasma and neutrals in MAGNUM-PSI,” *J. Nucl. Mater.*, vol. 363-365, pp. 330–334, 2007.
- [2] Z. Ahmad and W. J. Goedheer, “Optimization and characterization of a Pilot-PSI cascaded arc with non-LTE numerical simulation of Ar, H₂ gases,” *Plasma Sources Sci. Technol.*, vol. 18, no. 015008, 2009.
- [3] K. S. C. Peerenboom, W. J. Goedheer, J. van Dijk, and J. J. A. M. van der Mullen, “Integral simulation of the creation and expansion of a transonic argon plasma,” *Plasma Sources Sci. Technol.*, vol. 2, no. 19, 2010.
- [4] H. J. van der Meiden, “Collective Thomson scattering for ion temperature and velocity measurements on Magnum-PSI: a feasibility study,” *Plasma Phys. Controlled Fusion*, vol. 52, no. 045009, 2010.
- [5] D. Wunderlich, S. Dietrich, and U. Fantz, “Application of a collisional radiative model to atomic hydrogen for diagnostic purposes,” *J. Quant. Spectrosc. Radiat. Transfer*, vol. 110, pp. 62–71, 2009.
- [6] O. Rottier, “Continuum and line emission measurements on Pilot-PSI,” Bachelor Thesis, Universiteit Utrecht, 2010.
- [7] S. Wolbers, “A collisional-radiative model for atomic and molecular hydrogen in Pilot-PSI,” Bachelor Thesis, Universiteit Utrecht, 2011.
- [8] G. van der Star, Masters Thesis, Universiteit Utrecht, 2011.
- [9] J. Westerhout *et al.*, “Chemical erosion of different carbon composites under ITER-relevant plasma conditions,” *Phys. Scripta*, vol. T138, no. 014017, 2009.
- [10] K. Bystrov, J. Westerhout, M. Matveeva, A. Litnovsky, L. Marot, E. Zoethout, and G. D. Temmerman, “Erosion yields of carbon under various plasma conditions in Pilot-PSI,” *J. Nucl. Mater.*, 2011.
- [11] G. M. Wright *et al.*, “Materials research under ITER-like divertor conditions at FOM Rijnhuizen,” *J. Nucl. Mater.*, 2010.
- [12] G. D. Temmerman *et al.*, “Interactions of diamond surfaces with fusion relevant plasmas,” *Phys. Scripta*, vol. T138, no. 014013, 2009.
- [13] J. D. Swift and M. J. Schwar, *Electrical Probes for Plasma Diagnostics*. London: Iliffe Books Ltd., 1970.
- [14] A. Kallenbach *et al.*, “Divertor power and particle fluxes between and during type-I ELMs in the ASDEX upgrade,” *Nucl. Fusion*, vol. 48, no. 085008, 2008.

-
- [15] G. M. Staebler, "Divertor bias experiments," *J. Nucl. Mater.*, vol. 220-222, pp. 158–170, 1995.
- [16] P. J. Harbour, "Current flow parallel to the field in a scrape-off layer," *Contrib. Plasm. Phys.*, vol. 28, pp. 417–419, 1988.
- [17] P. C. Stangeby, *The Plasma Boundary of Magnetic Fusion Devices*. Taylor & Francis Group, 2000.
- [18] K. Ida, S. Hidekuma, Y. Miura, T. Fujita, M. Mori, K. Hoshino, N. Suzuki, T. Yamauchi, and JFT-2M Group, "Edge electric-field profiles of H-mode plasmas in the JFT-2M tokamak," *Phys. Rev. Lett.*, vol. 65, no. 11, 1990.
- [19] L. D. Horton *et al.*, "Characterization of the H-mode edge barrier at ASDEX Upgrade," *Nucl. Fusion*, vol. 45, pp. 856–862, 2005.
- [20] V. Rozhansky, "Modelling of the edge plasma with account of self-consistent electric fields," *Contrib. Plasm. Phys.*, vol. 46, no. 7-9, pp. 575–585, 2006.
- [21] J. Roth *et al.*, "Recent analysis of key plasma wall interaction issues for ITER," *J. Nucl. Mater.*, vol. 390-391, pp. 1–9, 2009.
- [22] W. Eckstein, "Sputtering yields," *Top. Appl. Phys.*, vol. 110, pp. 33–187, 2007.

Acknowledgements

The work in this thesis came about with the help and support of many people. First and foremost of course from my daily supervisor, Gerard van Rooij. Thank you for your guidance, for straightening out my texts and for helping me to find and distill the importance of my results. Thanks for encouraging me when things were difficult. Most of all, thank you for sharing your insight in physics problems. I am always amazed by the clarity with which you can see ‘straight through’ a problem.

Thank you to my promotores, Prof. Niek Lopes Cardozo and Prof. Daan Schram. Daan, you have been the driving force behind so much of this work. Even though it is not always what I wanted at the time, thank you for hanging on until the very end - and even further - in every discussion, for never giving up. Thanks for your sharing your amazing depth of knowledge about plasma physics and also for your genuine interest in my research. Niek, thank you for all your input, for sharpening my arguments and my texts. I learned a lot and was greatly motivated by the discussions we had. Your skill in expressing arguments both very specifically and very generally never ceases to impress me. Thank you also to the members of Niek’s group in Eindhoven who always made me feel welcome when I visited. Thank you to Prof. Ursel Fantz, Prof. Jaap Schouten and Prof. Wim van der Zande for reading and evaluating this thesis. Prof. Tony Donné, thank you for keeping an eye on the whole process. I really appreciated the support.

A thousand thanks to Hugo de Blank and to Prof. Wim Goedheer. I have called upon your knowledge countless times since I met you in your plasma physics lectures some six years ago. Both of you always took the time to explain the wonders of plasma physics to me clearly and patiently. Another thousand thanks to the students that I supervised: Jan Leijssen, Bram van den Langenberg, Jurriaan Biesheuvel, Rianne ’t Hoen and Otto Rottier. I learned at least as much from you as you did from me and you contributed to a lot of the work in this thesis. Thanks to my room-mates over the years for your wisdom and ‘gezelligheid’, Jan-Willem Blokland (roomie), Dagmar de Rooij and Martijn Graswinkel.

Thanks to all the people outside of Rijnhuizen with whom I have had the pleasure of working with over the years. Thanks for sharing your knowledge: Graham Wright, Prof. Dennis Whyte, Mr. V. Anita, Claudiu Costin, Marius Solomon, Prof. Ursel Fantz, Dirk Wunderlich, Thornton Greenland, Oleksandr Marchuk and Prof. Nader Sadeghi.

For work in the lab I owe thanks to many people. Firstly of course, Richard Al. Where would I have been without your help (always accompanied with a good story) in all of the experimental work in this thesis? And the rock-climbing was good too! Thanks to Marc van de Pol, for all the assistance, discussions and for the many evenings you offered up to guarantee our safety. Thanks to Hennie van der Meiden for all the assistance with the Thomson scattering diagnostic and for your wisdom in general. For

general technical assistance, thank you to Andries Lof, Bart de Groot, Ogé Kruijt, Paul Smeets and Rob Prins. Thanks also to Ton van der Grift and Wim Melissen for getting the magnetic field back on-line whenever something went wrong, even on your free days. Thanks to Peter Wortman and everyone else from the workshop and drawing office for designing and constructing vital experimental parts. Thanks also for all the last minute odd-jobs and for helping out with the MacGyver constructions. Thank you to Giel Berden for lending us laser equipment and expertise and to the Felix group for ordering dinner when experiments and writing crept into the evening hours. Thanks to all my fellow OIOs and students who helped out with measurements, especially members of ‘Low temperature plasma physics and heating’ group, Wouter Vijvers, Jeroen Westerhout, Niek den Harder and Gido van der Star.

I would also like to thank the many people who helped to form the ideas presented in this thesis. Many I have already named, others are: Greg de Temmerman (thanks for sharing your knowledge so generously), Prof. Aart Kleyn, Prof. Juergen Rapp, Kyrill Bystrov, Jakub Zielinski, Manfred von Hellerman, Miranda van den Berg, Oliver Lischtschenko, Rob Wieggers and Gijs van Swaaij. Thanks to Jan-Willem Blokland for the template of this thesis and to Dagmar de Rooij and Jeroen Westerhout for sharing your experience on that front. Thank you Gieljan de Vries for all your writing advice and for editing the Dutch version of my summary. Thanks to Victor Veremiyenko, Martijn Nuijten and Hennie van der Meiden for the work you did on spectral analysis before I arrived that I could build on. Thank you to Hajnal Vörös, for making sure I always had enough to read, to the ICT department for keeping the computers healthy, to everyone who kept my work place clean and kept me well fed and of course to Frits Hekkenberg for keeping the whole institute running all the time.

And of course thanks to everyone for the good times in this little piece of paradise in Nieuwegein. To name a few more who I have not yet mentioned, thank you to the Rijnhuizen footballers, to Hans Goedbloed (for the philosophy), Albert Wildeman, Alex Poelman (for the photos), Alireza Torghabeh, Anouk Rijs, Arian Visser, Aron Tamminga, Bircan Ayten, Bob Krijger, Dennis Rondén, Dick Hogeweij, Egbert Westerhof, Emiel van der Plas and Erik Min (for the stories), Eric Louis, Hirokazu Ueta, Jan-Cornelis Wolff, John Scholten, Jonathon Citrin, Kees van der Geer, Lenze van der Vegt, Lianne van Swieten, Marjo Lubbers, Mark Westra, Michael Gleeson, Miranda Breugem, Noud Oomens, Pedro Zeijlmans van Emmichoven, Saskia Bruijn, Stefan Wolbers, Thijs van der Wielen, Tim Tsafarti, Theo Oyevaar, Thijs Versloot, Victor Land, Vivike Lapoutre, Waldo Bongers, Wim Koppers and Wolf Weymiens.

The realization of this thesis has been a journey, not only in the world of physics, but also in the emotional sphere. I want to especially thank the people who helped me make it through the emotions of a PhD. Dagmar, Hans, Linda and Reinder, thanks for being such wonderful friends. Christine, thank you from the bottom of my heart for your guidance. Thank you Mum and Dad for standing by me and for always encouraging me to follow my heart. And thanks to all my friends and family for being there.

Last but most importantly, to my wife Eef, thank you for your help designing the cover of this thesis and much more importantly for walking beside me throughout this adventure. I could never have done it without you!

Curriculum vitae

I was born on the 1st of December 1979 in Calgary Canada to Australian parents and lived in Australia from 1982 until 2001. In December 1997 I finished secondary school at "Merewether High School" in Newcastle, Australia. Having obtained the "High School Certificate", I spent 1998 exploring my home country, Australia with a backpack. Settling back into studies, I started a combined degree in Physics and Information technology at the University of NSW, Sydney Australia in 1999. After two years of study, I moved to Holland at the beginning of 2001 to be with my Dutch partner, who is now my wife. In the same year I passed the NT2 exam for the Dutch language required for undergraduate study at a Dutch university. I continued my studies in experimental physics at the University of Leiden in the Netherlands and graduated in November 2005, with a Masters project in experimental plasma physics at the FOM Institute Rijnhuizen. In 2006 I took a job as public information officer at the same institute and one year later decided to apply for a PhD position, which I started at the same FOM institute in January 2007. This thesis describes the results of my PhD research.